

AN ABSTRACT OF THE DISSERTATION OF

Kirk D. Rowe for the degree of Doctor of Philosophy in Physics presented on  
December 9, 2004.

Title: Unusual Quantum Effects in Scattering Wave functions of Two-Dimensional  
Cage Potentials.

Abstract approved: *Redacted for Privacy*

---

Philip J. Siemens

We exhibit long-lived resonances in scattering from two-dimensional soft cage potentials comprised of three and four Gaussian peaks. Specific low-energy resonances with very narrow width are shown to correspond to classical multiple-reflection events. These states have much larger probability densities inside the cage than outside and mimic bound states in the sense that the symmetry-breaking effect of the incident wave is relatively small. As a result we have found that isolated states display the simple symmetry characteristics of bound states. Overlapping resonances exhibit a mixing of symmetry classes leading to wave functions of lower symmetry, like those of wider resonances at higher energy. We demonstrate that at energies below the lowest resonances of two-dimensional cages, where the distance across the entrance of the cage corresponds to less than half a wavelength, the wave function may still gain access to the interior region by squeezing its

wavelength in the necessary direction at the expense of the kinetic energy in the direction normal to the opening. The resulting curvature of the wave function in the donor dimension corresponds to an imaginary wavenumber, curving away from the plane defined by zero amplitude. This mechanism for passing between obstacles may be relevant for electronic and optical devices having spatial structures with dimensions comparable to the wavelengths of the energy carriers.

©Copyright by Kirk D. Rowe

December 9, 2004

All Rights Reserved.

Unusual Quantum Effects in Scattering Wave functions of Two-Dimensional Cage  
Potentials

by  
Kirk D. Rowe

A DISSERTATION  
submitted to  
Oregon State University

in partial fulfillment of  
the requirements for the  
degree of

Doctor of Philosophy

Presented December 9, 2004  
Commencement June 2005

Doctor of Philosophy dissertation of Kirk D. Rowe presented on December 9, 2004.

APPROVED:

*Redacted for Privacy*

---

Major Professor, representing Physics

*Redacted for Privacy*

---

Chair of the Department of Physics

*Redacted for Privacy*

---

Dean of the Graduate School

I understand that my dissertation will become part of the permanent collection of Oregon State University libraries. My signature below authorizes release of my dissertation to any reader upon request.

*Redacted for Privacy*

---

Kirk D. Rowe, Author

## ACKNOWLEDGEMENTS

As is sometimes the case, an undertaking such as this can be intractable if not for support and guidance of others. The author wishes to single out, with great appreciation, Dr. Philip Siemens for special recognition as one such individual who made available both his time and wisdom on which the author relied greatly during the steps leading up to and including the preparation of this document. The author is also grateful to the remainder of his committee: Roger Nielsen, William Warren, Victor Madsen and Viktor Podolskiy, for the time spared to play their roles in the completion his degree. The author is additionally grateful to Dr. Henri Jansen who contributed much of his time providing special assistance and helpful suggestions. Acknowledgement is extended to Dr. Rubin Landau, who provided reference to published literature on the subtraction method as well as the paper by Gaspard and Rice [26] which led to the idea of investigating cage potentials.

The deepest heartfelt gratitude extends, of course, to my parents whose love, support and encouragement, when times were toughest, kept me on track. Thanks mom and dad.

My dog Shadow deserves mention for providing warm fuzzy feelings as well as engaging mathematical exchanges.

# TABLE OF CONTENTS

	<u>Page</u>
1 Introduction . . . . .	1
2 Literature Review . . . . .	3
2.1 A Formal Theory . . . . .	4
2.1.1 Time-Dependent Scattering . . . . .	4
2.1.2 Time-Independent Scattering . . . . .	7
2.2 Additional Developments . . . . .	9
2.2.1 Hard Potentials . . . . .	11
2.2.2 Computations on Parallel Processors . . . . .	14
2.3 Discrete Momentum Representation . . . . .	16
2.3.1 Literature Search . . . . .	17
3 Exact Quantum Theory . . . . .	18
3.1 Basic Equations . . . . .	18
3.2 Representations of Equations . . . . .	20
3.2.1 Migrating Poles . . . . .	22
4 Numerical Methods . . . . .	24
5 3-center scattering potential . . . . .	30
6 4-center scattering potential . . . . .	50
7 Conclusions . . . . .	88

## TABLE OF APPENDICIES

	<u>Page</u>
Appendicies Heading Page . . . . .	90
A Solution by Green's Function . . . . .	91
B Scattering Amplitude Particulars . . . . .	93
C Scattering Amplitude Dependence of 2-D Differential Cross Sections . . . . .	96
D Two-Dimensional Partial Wave Basis . . . . .	98
E Momentum Space Representation of the $D_3$ Potential . . . . .	104

## LIST OF FIGURES

<u>Figure</u>	<u>Page</u>
3.1 Complex momenta, $k$ , of the fourth (top left) and eighth (bottom left) octants map to energies, $E$ , in the fourth quadrant of the first (top right) and second (bottom right) Riemann sheets. . . . .	21
3.2 Radial integration contour specified with a $+i\epsilon$ prescription. . . . .	23
4.1 Verification of differential cross section output (open circles) by comparison against a partial wave analysis (filled dots) for the central test potential (4.3) where $V_a = 0$ , $E_o/V_{\max} = e^2/(4\pi)$ , and $V_b = -16$ (top) $V_b = -256$ (bottom). . . . .	26
4.2 First Born approximations ( $VG^+V$ ) to the corrected radial integrands with the subtraction given by (4.1) after they have been analytically continued to complex energies of (from top to bottom row) $E = \{(4.0, .001), (4.0, .01), (4.0, .1), (4.0, 1.0)\}$ , as a function of $k'$ . Here $k_x = .75$ , $k_y = .75$ and $\theta = \pi/4$ . Real (left) and imaginary (right) parts plotted. Note how the undulation widens as the energy moves away from the real axis. . . . .	27
5.1 Three center scatterer. . . . .	30
5.2 $D_3$ irreducible abstract representations. . . . .	32
5.3 Difference of first (top) and seventh (bottom) phase shifts for soft and hard potentials with $\delta_o$ matched. From fits of the last eight data points, $\Delta\delta(\text{hard-soft}) \propto V^n$ where $n = -2.97 \times 10^{-6}$ (top) and $n = -3.74 \times 10^{-2}$ (bottom). . . . .	36
5.4 Partial wave phase shifts for a central hard disc of unitary radius (open circles) and one centralized exponential peak from (5.1) with $V_o = 1200$ and $a = 1.6$ (dots). . . . .	37
5.5 Total differential cross section on-axis (upper) and $30^\circ$ off-axis (lower) for (5.1) with $V_o = 1200$ , $a = 1.6$ and $R = 2.5$ . . . . .	38
5.6 Probability density for the first resonance of table 5.2 for which $V_o = 1200$ , $a = 1.6$ and $E = 46.1718$ with normal incidence. . . . .	39
5.7 Probability density for the second resonance of table 5.2 for which $V_o = 1200$ , $a = 1.6$ and $E = 69.9163$ with normal incidence. . . . .	40
5.8 Probability density for the third resonance of table 5.2 for which $V_o = 1200$ , $a = 1.6$ and $E = 133.5$ . Here the incident angle is $\theta_o = \pi/12$ . . . . .	41
5.9 Clipped probability density for the first resonance of table 5.2 for which $V_o = 1200$ , $a = 1.6$ and $E = 46.1718$ with normal incidence. Note how the particle flux is able to move through the potential. . . . .	42

## LIST OF FIGURES (Continued)

<u>Figure</u>	<u>Page</u>
5.10 Clipped probability density just above, $E=46.3500$ , the fundamental resonance, $E=46.1718$ , for $V_o = 1200$ with a normal angle of incidence. Note that the particle flux exiting the potential's interior region is greatly reduced as compared to that at resonance given by figure 5.9. . . . .	43
5.11 Real part of the third resonance's clipped wave function. Black $< -.001 < Gray < .001 < White$ (top). Black $< -.0002 < Gray < .0002 < White$ (bottom). The incident plane wave is seen to approach from the left at a $15^\circ$ downward angle. . . . .	44
5.12 Probability density below, $E=45.0$ , the fundamental resonance, $E=46.1718$ , for $V_o=1200$ with a normal angle of incidence. Note that the particle flux is unable to penetrate into the potential's interior region. . . . .	45
5.13 Probability density below, $E=46.0725$ , the fundamental resonance, $E=46.1718$ , for $V_o = 1200$ with a normal angle of incidence. At this energy the particle flux is first able to squeeze into the potential's interior region. . . . .	46
5.14 Real part of wave function below, $E=46.0725$ , the fundamental resonance of $E=46.1718$ for $V_o = 1200$ with a normal angle of incidence showing quantum pinching (viewed from underneath). . . . .	47
5.15 Imaginary part of wave function below, $E=46.0725$ , the fundamental resonance of $E=46.1718$ for $V_o=1200$ with a normal angle of incidence showing quantum pinching. . . . .	48
5.16 Imaginary part of wave function below, $E=9.56$ , the fundamental resonance of $E=9.8326$ for $V_o=100$ with a normal angle of incidence showing quantum pinching. . . . .	49
6.1 Four center scatterer. . . . .	51
6.2 $D_4$ irreducible abstract representations. . . . .	51
6.3 Total differential cross section on-axis (top) and $15^\circ$ off-axis (bottom) for (6.1) with $V_o=1200$ , $a=1.6$ and $R=2.5$ . . . . .	54
6.4 Differential cross sectional surface (top) with the corresponding integrated total cross section (bottom) for (6.1) with $V_o=100$ , $a=1.6$ , $R=2.5$ and an incident angle of $0^\circ$ . . . . .	55

## LIST OF FIGURES (Continued)

<u>Figure</u>	<u>Page</u>
6.5 Probability density for the first resonance of table 6.2 for which $V_o = 100$ , $a = 1.6$ and $E = 5.51305$ with normal incidence. . . . .	56
6.6 Probability density for the second resonance of table 6.2 for which $V_o = 100$ , $a = 1.6$ and $E = 11.3781$ with normal incidence. . . . .	57
6.7 Probability density for the third resonance of table 6.2 for which $V_o = 1200$ , $a = 1.6$ and $E = 45.7994$ with normal incidence. . . . .	58
6.8 Probability density for the fourth resonance of table 6.2 for which $V_o = 1200$ , $a = 1.6$ and $E = 50.9141$ with normal incidence. . . . .	59
6.9 Probability density for the fifth resonance of table 6.2 for which $V_o = 1200$ , $a = 1.6$ and $E = 61.8927$ with normal incidence. . . . .	60
6.10 Probability density for the sixth resonance of table 6.2 for which $V_o = 1200$ , $a = 1.6$ and $E = 74.0325$ with normal incidence. . . . .	61
6.11 Probability density for the seventh resonance of table 6.2 for which $V_o = 1200$ , $a = 1.6$ and $E = 78.8937$ with normal incidence. . . . .	62
6.12 Probability density for the eighth resonance of table 6.2 for which $V_o = 1200$ , $a = 1.6$ and $E = 105.017$ . Here the incident angle is $\theta_o = \pi/12$ . . . . .	63
6.13 Probability density for the ninth resonance of table 6.2 for which $V_o = 1200$ , $a = 1.6$ and $E = 109.108$ with normal incidence. . . . .	64
6.14 Probability density for the tenth resonance of table 6.2 for which $V_o = 1200$ , $a = 1.6$ and $E = 114.780$ with normal incidence. . . . .	65
6.15 Probability density for the eleventh resonance of table 6.2 for which $V_o = 1200$ , $a = 1.6$ and $E = 131.429$ . Here the incident angle is $\theta_o = \pi/12$ . . . . .	66
6.16 Probability density for the twelfth resonance of table 6.2 for which $V_o = 1200$ , $a = 1.6$ and $E = 134.587$ with normal incidence. . . . .	67
6.17 Probability density for the thirteenth resonance of table 6.2 for which $V_o = 1200$ , $a = 1.6$ and $E = 147.285$ with normal incidence. . . . .	68

## LIST OF FIGURES (Continued)

<u>Figure</u>	<u>Page</u>
6.18 Real (top) and imaginary (bottom) parts of the wave function belonging to the first resonance of table 6.2 which carries the fundamental $A_1$ symmetry. . . . .	70
6.19 Real (top) and imaginary (bottom) parts of the fourth resonance's clipped wave function showing the second $A_1$ symmetry (note the single nodal ring at fixed radius). Black < $-.002$ < Gray < $.002$ < White (top). The incident plane wave is seen to approach from the left. . . . .	71
6.20 Real (top) and imaginary (bottom) parts of the fifth resonance's clipped wave function showing $E$ symmetry. Black < $-.001$ < Gray < $.001$ < White (top). The incident plane wave is seen to approach from the left. . . . .	72
6.21 Real (top) and imaginary (bottom) parts of the wave function belonging to the third resonance of table 6.2 which carries $B_1$ symmetry. . . . .	73
6.22 Real (top) and imaginary (bottom) parts of the third resonance's clipped wave function showing $B_1$ symmetry. Black < $-.005$ < Gray < $.005$ < White (top). The incident plane wave is seen to approach from the left. . . . .	74
6.23 Real (top) and imaginary (bottom) parts of the wave function belonging to the eighth resonance of table 6.2 which carries $B_2$ symmetry. The incident plane wave is seen to approach from the left at a $15^\circ$ downward angle. . . . .	75
6.24 Real (top) and imaginary (bottom) parts of the eighth resonance's clipped wave function showing $B_2$ symmetry. Black < $-.01$ < Gray < $.01$ < White (top). The incident plane wave is seen to approach from the left at a $15^\circ$ downward angle. . . . .	76
6.25 Real (top) and imaginary (bottom) parts of the eleventh resonance's clipped wave function showing $A_2$ symmetry. Black < $-.005$ < Gray < $.005$ < White (top). The incident plane wave is seen to approach from the left at a $15^\circ$ downward angle. . . . .	77
6.26 Schematic for the rotation of the real parts of mixed state vectors, neglecting normalization, belonging to the sixth and seventh resonance. . . . .	79
6.27 Real (top) and rotated (bottom) part of the sixth resonance's clipped wave function showing $A_1$ symmetry. Black < $-.005$ < Gray < $.005$ < White (top). The incident plane wave is seen to approach from the left. . . . .	81

LIST OF FIGURES (Continued)

<u>Figure</u>	<u>Page</u>
6.28 Real (top) and rotated (bottom) part of the seventh resonance's clipped wave function showing $E$ symmetry. Black $< -.005 < Gray < .005 < White$ (top). The incident plane wave is seen to approach from the left. . . . .	82
6.29 Vector fields representing current density (top) and velocity (bottom) of the fundamental resonance calculated from (3.9). Vector lengths are relative, the longest being scaled to the radius of a circle determined by the bases of the nearest neighbors. Any magnitudes below a cutoff threshold of 0.061% (curr.) and 0.257% (vel.) of maximum are indicated by dots. . . . .	83
6.30 Probability density at $E=5.43750$ , just below the fundamental resonance of table 6.2. . . . .	84
6.31 Real part of wave function at $E = 5.43750$ , just below the fundamental resonance of table 6.2, which shows quantum pinching. . . . .	85
6.32 Imaginary part of wave function at $E = 5.43750$ , just below the fundamental resonance of table 6.2, which shows quantum pinching. . . . .	86
6.33 Panoramic probability density for the fourth resonance of table 6.2 for which $V_0 = 1200$ , $\alpha = 1.6$ and $E = 50.9141$ showing complicated interference pattern and the shadow behind the scatterer opposite the incident wave. Truncation of the probability peak here shows the dip in particle densities forming a circular pattern. . . . .	87

LIST OF TABLES

<u>Table</u>	<u>Page</u>
5.1 $D_3$ dihedral character table. . . . .	31
5.2 First three 'long-lived' resonances with $a=1.6$ and $R=2.5$ . . . . .	33
6.1 $D_4$ dihedral character table. . . . .	50
6.2 First thirteen 'long-lived' resonances with $a=1.6$ and $R=2.5$ . . . . .	53

LIST OF APPENDIX FIGURES

<u>Figure</u>	<u>Page</u>
B.1 Relationship between the vectors used. . . . .	94
C.1 Relationship between incident and scattered current densities. . . . .	96

## LIST OF APPENDIX TABLES

<u>Figure</u>	<u>Page</u>
D.1 Phase shifts obtained and used in the generation of the top plot of figure 5.4. . . . .	103
D.2 Phase shifts obtained and used in the generation of the bottom plot of figure 5.4. . .	104

Dedicated to the memory of  
Dr. Rudolf Carl Christian Bauer.

# Chapter 1

## Introduction

The importance of scattering and resonant features in contemporary physics cannot be overlooked. The realization of Moore's law over the last four decades, for example, has stimulated a growing interest in the area of mesoscopic physics, specifically in the field of nano and molecular electronics. Aggressive miniaturization of electronic components requires a detailed understanding of the quantum effects that govern them. These devices are based on the quantum properties of electrons, moving in up to three dimensions, confined to an island or a region separated from both the source and drain by a potential barrier [1]. Such systems include quantum dots, resonant tunneling devices, and single-electron transistors. Current flow through them is intimately tied to their resonance structure and their quantum transport properties. As computers, in turn, gain power it becomes possible to investigate complicated models with nonseparable potentials that require the extension of one-dimensional techniques to multiple dimensions.

One new area where this multidimensional analysis is being applied is to photonic crystal fibers (PCFs) [2], which have been manufactured for less than a decade. These are optical fibers that have a regular array of air channels along their length surrounding some central defect. This central defect may be a larger hollow central channel or, as in the case of a solid-core PCF, the absence of such a channel. For the hollow-core case the mechanism for light propagation along the fiber is not due to total internal reflection, which requires a cladding of a relatively lower refraction index, but instead is realized through photonic band gaps or optical suppression in the direction transverse to the fiber's length. For the solid-core fibers, on the other hand, the average index of the channeled medium surrounding the solid central core is reduced, making total internal reflection possible for certain frequencies. With white light introduced at one end of the fiber, only certain colors are

visible on the other end. The complex structure of PCFs dictate that Maxwell's equations must be solved numerically. This task, in the case of a two-dimensional microstructured fiber, decouples into two problems: propagation along the length of the fiber, and scattering in the transverse plane. For transverse in-plane scattering, the full vector problem may be decomposed into a scalar Helmholtz problem for each of the two principal polarizations  $E_{\parallel}$  and  $H_{\parallel}$  [3, 4]. Solid-core PCFs are now marketed commercially as endlessly single mode [5], not possible for conventional optic fibers. The air holes in the PCF's cross section act as a modal sieve. The fundamental mode has a transverse wavelength too long to escape through the gaps, while higher modes can leak away between the air holes. This caging effect may be tuned by adjusting the diameter of the holes, making it possible to trap additional modes. Adjusting the exact geometry may resonate the fundamental mode which in turn can affect dispersion properties. For pulsed digital communication it is obviously advantageous to minimize packet spreading.

Exploring the foundations of this new frontier, we have made some interesting observations and uncovered an as-yet undocumented physical behavior. In this paper the Lippmann-Schwinger technique is applied to noncentral potentials in two dimensions. We use the theory to compute transition matrices for open quantum systems governed by repulsive soft hyperbolically-defocusing scatterers that may trap quantum particles either through multiple internal reflection or by a quantum caging effect. This allows us to describe the given system in terms of its wave functions, resonances, and cross sections. Low-lying long-lived resonances are investigated for both tri-peaked and quad-peaked repellers to determine wave function symmetries and other universal characteristics. One novel feature is a phenomenon similar to quantum tunneling which allows a wave function to penetrate a narrow aperture less than a half wavelength wide. This is accomplished by borrowing kinetic energy from the propagation direction, which can change the sign of the curvature in that dimension, to localize the wave transversely. This squeezing in the crucial dimension is the mechanism by which the wave function gains passage. This phenomenon does not present itself for one-dimensional systems due to the lack of a secondary or donor dimension.

An exact two-dimensional quantum theory is presented in chapter 3 while the particulars of its specific implementation are covered in chapter 4. Results for the three and four-center scatterers are given separately in chapters 5 and 6. Conclusions are summarized in the final chapter.

## Chapter 2

# Literature Review

In 1900 the modern theory of integral equations was founded with a publication by Swedish mathematician Erik Ivar Fredholm [6]. Being the first earnest work in the field since Volterra, this initial paper developed the essential part of a theory of what has become to be known as Fredholm's integral equation. Building on this work, he published a fuller version of his theory in 1903 which goes on to define and solve the Fredholm integral equation of the second kind [7],

$$\Psi(\mathbf{r}) = \varphi(\mathbf{r}) + \lambda \int K(\mathbf{r}, \mathbf{r}') \Psi(\mathbf{r}') d\mathbf{r}'. \quad (2.1)$$

Much of Fredholm's theory was founded on work done by George Hill, an American astronomer who used linear equations involving determinants having an infinite number of rows and columns. These findings also provided a basis for much of the subsequent research carried out by well known German mathematician David Hilbert who extended Fredholm's work to include a complete eigenvalue theory for the Fredholm integral equation. These findings would be key for a formal scattering theory yet to be revealed.

It is by scattering that the structure of things too small to measure directly may be probed. Early scattering experiments by Ernest Rutherford on thin metal foils, for example, invalidated the Thomson model of the atom. Intermittent large deflections of alpha particles led Rutherford to surmise that the positive charge within an atom is packed into a small dense central nucleus [8]. This model was then upgraded in 1915 by Niels Bohr to include electron orbitals of quantized energy [9]. The fundamental aspects of collision theory were put forward in 1933 in the book by Mott and Massey [10] and continued to evolve with the introduction of a scattering matrix concept by Wheeler [11] and Heisenberg [12]. The general formulation of the mathematical problem of finding the S-

matrix followed quickly and in the early 1950's a formal theory of scattering was presented by both Lippmann and Schwinger [13] and Gell-Mann and Goldberger [14].

## 2.1 A Formal Theory

Through the application of variational principles, B. A. Lippmann and Julian Seymour Schwinger were the first to express the scattering process in terms of a formal integral equation,

$$|\Psi_{\mathbf{k}_o}^\pm\rangle = |\varphi_{\mathbf{k}_o}\rangle + \frac{1}{E_{k_o} - H_o \pm i\varepsilon} V |\Psi_{\mathbf{k}_o}^\pm\rangle, \quad (2.2)$$

appearing in their famous 1950 paper [13] as equation number ([13]-1.61) which we recognize to be a Fredholm integral equation of the second kind. They also provide an expression for the transition matrix,

$$T_{\mathbf{k}\mathbf{k}_o} = \langle \varphi_{\mathbf{k}} | T | \varphi_{\mathbf{k}_o} \rangle = \langle \varphi_{\mathbf{k}_o} | V | \Psi_{\mathbf{k}_o}^+ \rangle, \quad (2.3)$$

given as ([13]-1.63). A parallel presentation of formal scattering theory developed from first principles was also published by Gell-Mann and Goldberger [14] in which the two equations above appear as ([14]-{2.30, 2.31}). Multiplication of (2.2) from the left by  $\langle \varphi_{\mathbf{k}} | V$  produces what has been universally accepted as the Lippmann-Schwinger equation for the transition matrix,

$$T_{\mathbf{k}\mathbf{k}_o} = V_{\mathbf{k}\mathbf{k}_o} + \int V_{\mathbf{k}\mathbf{k}'} \frac{1}{E_{k_o} - H_o \pm i\varepsilon} T_{\mathbf{k}'\mathbf{k}_o} d\mathbf{k}'. \quad (2.4)$$

These equations are central to the research to follow and are presented here in the following mathematical context.

### 2.1.1 Time-Dependent Scattering

Beginning with the time-dependent form of Schrödinger's equation,

$$i\hbar \frac{\partial}{\partial t} \Psi(\mathbf{r}, t) = H \Psi(\mathbf{r}, t); \quad H = H_o + V, \quad (2.5)$$

and relations:

$$\begin{aligned} \left( i\hbar \frac{\partial}{\partial t} - H_o \right) \tilde{G}_o^\pm(t) &= \delta(t) \\ \left( i\hbar \frac{\partial}{\partial t} - H \right) \tilde{G}^\pm(t) &= \delta(t), \end{aligned} \quad (2.6)$$

four propagators may be defined. The first set is made up of the *free* propagators:

$$\begin{aligned}\tilde{G}_o^+(t) &= -\frac{i}{\hbar}\Theta(+t)e^{-iH_o t/\hbar} = \begin{cases} 0 & : t < 0 \\ -\frac{i}{\hbar}e^{-iH_o t/\hbar} & : 0 < t \end{cases} \\ \tilde{G}_o^-(t) &= +\frac{i}{\hbar}\Theta(-t)e^{-iH_o t/\hbar} = \begin{cases} +\frac{i}{\hbar}e^{-iH_o t/\hbar} & : t < 0 \\ 0 & : 0 < t, \end{cases}\end{aligned}\quad (2.7)$$

which describe the evolution of states subject to only the kinetic energy term,  $H_o = -\hbar^2\nabla^2/(2\mu)$ , of the Hamiltonian with the interaction,  $V$ , turned off. The following set of propagators include the contribution from the potential and are referred to as the *exact* Green's functions:

$$\begin{aligned}\tilde{G}^+(t) &= -\frac{i}{\hbar}\Theta(+t)e^{-iHt/\hbar} = \begin{cases} 0 & : t < 0 \\ -\frac{i}{\hbar}e^{-iHt/\hbar} & : 0 < t \end{cases} \\ \tilde{G}^-(t) &= +\frac{i}{\hbar}\Theta(-t)e^{-iHt/\hbar} = \begin{cases} +\frac{i}{\hbar}e^{-iHt/\hbar} & : t < 0 \\ 0 & : 0 < t. \end{cases}\end{aligned}\quad (2.8)$$

The top and bottom propagators of each set may also be paired in terms of their time dependence. The operators  $\tilde{G}_o^+$  and  $\tilde{G}^+$  describe forward propagation of states and are referred to as *retarded* Green's functions. The alternate operators,  $\tilde{G}_o^-$  and  $\tilde{G}^-$ , describe a state's earlier history in time and are referred to as the *advanced* Green's functions.

In formalizing the time-dependent theory,  $\Psi^{\text{in}}(t)$  and  $\Psi^{\text{out}}(t)$  states are introduced in the literature. The potential is assumed to be local and short ranged, but for the moment it is assumed to be switched off so that all time evolution is governed momentarily by the free propagators. The *in-state*, given by

$$\Psi^{\text{in}}(t) \equiv \lim_{t' \rightarrow -\infty} i\hbar\tilde{G}_o^+(t-t')\Psi(t'), \quad (2.9)$$

is equal to the exact state function of the complete interacting system in the infinite past where a mixture of eigenstates forms a wave packet distant enough from the interaction region so that its effects are not felt. This state is then evolved in the forward temporal direction by the appropriate free Green's function until it is spatially incident upon the region where the potential's influence would normally be effective. From the infinite future, a free scattered wave may be evolved backwards through time in the same manner yielding an *out-state*,

$$\Psi^{\text{out}}(t) \equiv \lim_{t' \rightarrow \infty} -i\hbar\tilde{G}_o^-(t-t')\Psi(t'). \quad (2.10)$$

With the potential switched back on, further time development in the forward direction is now

governed by the exact Green's function and a full solution to 2.5 is represented by the equations:

$$\Psi^+(t) = \Psi^{\text{in}}(t) + \int_{-\infty}^{\infty} \tilde{G}^+(t-t')V\Psi^{\text{in}}(t') dt' \quad (2.11)$$

$$\Psi^-(t) = \Psi^{\text{out}}(t) + \int_{-\infty}^{\infty} \tilde{G}^-(t-t')V\Psi^{\text{out}}(t') dt'. \quad (2.12)$$

If a general case of (2.9) is taken where a free state is allowed to evolve forward in time by a finite amount, independent from the influence of the interaction,

$$\Psi_o(t') = -i\hbar\tilde{G}_o^-(t'-t)\Psi_o(t); \quad t' < t, \quad (2.13)$$

$\Psi^{\text{in}}(t')$  within the integrand of (2.11) may then be expressed in terms of the present time  $t$ . In doing so, the two in-states of common time may now be factored out,

$$\Psi^+(t) = \left[ \mathbf{I} - \frac{i}{\hbar} \int_{-\infty}^{\infty} \tilde{G}^+(t-t')V\tilde{G}_o^-(t'-t) dt' \right] \Psi^{\text{in}}(t). \quad (2.14)$$

The term in square brackets is known as a Møller wave operator [15] which after a change of variables,  $(t'-t) \rightarrow t''$ , is written

$$\Omega^+ \equiv \mathbf{I} - \frac{i}{\hbar} \int_{-\infty}^{\infty} \tilde{G}^+(-t'')V\tilde{G}_o^-(t'') dt''. \quad (2.15)$$

It gives the inbound exact state in terms of the free in-state and may be expressed explicitly, after another change of variables  $t'' \rightarrow t$ , as

$$\Omega^+ = \mathbf{I} - \frac{i}{\hbar} \int_{-\infty}^0 e^{iHt/\hbar} V e^{-iH_o t/\hbar} dt. \quad (2.16)$$

The integrand of (2.16) may be written in terms of an exact differential,

$$\Omega^+ = \mathbf{I} - \int_{-\infty}^0 \frac{d}{dt} \left( e^{iHt/\hbar} e^{-iH_o t/\hbar} \right) dt, \quad (2.17)$$

so that after evaluating the upper limit the Møller wave operator may be given in its most recognizable form,

$$\Omega^+ = \lim_{t \rightarrow -\infty} e^{iHt/\hbar} e^{-iH_o t/\hbar}. \quad (2.18)$$

Again, similar arguments may be carried through yielding the other Møller wave operator,

$$\Omega^- = \lim_{t \rightarrow \infty} e^{iHt/\hbar} e^{-iH_o t/\hbar}, \quad (2.19)$$

which acts on the out-state and gives the exact outbound wave function,

$$\Psi^-(t) = \Omega^- \Psi^{\text{out}}(t). \quad (2.20)$$

Notice that through the use of the Møller wave operators, the solutions, (2.11) and (2.12), to 2.5 may be represented as:

$$\Psi^+(t) = \Psi^{\text{in}}(t) + \int_{-\infty}^{\infty} \tilde{G}_o^+(t-t')V\Psi^+(t') dt' \quad (2.21)$$

$$\Psi^-(t) = \Psi^{\text{out}}(t) + \int_{-\infty}^{\infty} \tilde{G}_o^-(t-t')V\Psi^-(t') dt'. \quad (2.22)$$

In a scattering experiment one is interested in attaching probabilities to the occurrence of observables. Starting with a state vector  $\Psi^+(t)$  that is known to have been in the controlled input state  $\Psi^{\text{in}}(t)$  at some remote time of the past, one would like to find the probability of finding the system in the state described by  $\Psi^-$ , which is known to lead to  $\Psi^{\text{out}}(t)$ , in the distant future. The probability amplitude may be written as

$$\langle \Psi^-(t) | \Psi^+(t) \rangle. \quad (2.23)$$

Using (2.14) and (2.20) to incorporate the Møller operators,

$$\langle \Psi^-(t) | \Psi^+(t) \rangle = \langle \Omega^- \Psi^{\text{out}}(t) | \Omega^+ \Psi^{\text{in}}(t) \rangle. \quad (2.24)$$

This allows for the representation of (2.23) in terms of a single operator  $\Omega^+$  and its adjoint,  $\Omega^{-\dagger}$ ,

$$\langle \Psi^-(t) | \Psi^+(t) \rangle = \langle \Psi^{\text{out}}(t) | \Omega^{-\dagger} \Omega^+ | \Psi^{\text{in}}(t) \rangle. \quad (2.25)$$

This operator product is then given as the defining relationship for the scattering matrix,

$$S \equiv \Omega^{-\dagger} \Omega^+. \quad (2.26)$$

The fact that the  $S$  operator is independent of time can be seen from (2.16) and (2.19). Also, because the  $S$  operator specifies the probability amplitude for the transition between free in and out-states, its matrix elements are only non-zero for states having equal energy,

$$S(\mathbf{k}, \mathbf{k}_o) = \langle \Psi_{\mathbf{k}}^{\text{out}}(t) | S | \Psi_{\mathbf{k}_o}^{\text{in}}(t) \rangle; \quad \|\mathbf{k}\| = \|\mathbf{k}_o\|. \quad (2.27)$$

### 2.1.2 Time-Independent Scattering

The time dependence is eliminated from the formal theory by Fourier transforming back to the time-independent energy representation. The state vectors will thus take the form

$$\Psi(E) = \int_{-\infty}^{\infty} \Psi(t) e^{iEt/\hbar} dt, \quad (2.28)$$

and the propagators, (2.7) and (2.8), are transformed back to the *resolvents* of the operators  $H_o$  and  $H$ ,

$$\begin{aligned}\frac{1}{E - H_o \pm i\varepsilon} &= \int_{-\infty}^{\infty} \tilde{G}_o^{\pm}(t) e^{iEt/\hbar} dt \\ \frac{1}{E - H \pm i\varepsilon} &= \int_{-\infty}^{\infty} \tilde{G}^{\pm}(t) e^{iEt/\hbar} dt.\end{aligned}\quad (2.29)$$

To deduce the nature of a new matrix, the scattering matrix

$$S_{ks} = \langle \Psi_k^- | \Psi_s^+ \rangle \quad (2.30)$$

given by (2.23) is expanded. After the Fourier transformation of the kets (2.21),

$$|\Psi_s^+\rangle = |\Psi_s^{\text{in}}\rangle + \frac{1}{E - H_o + i\varepsilon} V |\Psi_s^+\rangle, \quad (2.31)$$

and (2.12),

$$|\Psi_k^-\rangle = |\Psi_k^{\text{out}}\rangle + \frac{1}{E - H - i\varepsilon} V |\Psi_k^{\text{out}}\rangle, \quad (2.32)$$

(2.31) and the dual space element of (2.32) may be inserted back into (2.30). Using the adjoint properties of the Green's functions,

$$\begin{aligned}G_o^-(E) &= G_o^{+\dagger}(E) \\ G^-(E) &= G^{+\dagger}(E),\end{aligned}\quad (2.33)$$

one is left with three inner products:

$$S_{ks} = \langle \Psi_k^{\text{out}} | \Psi_s^{\text{in}} \rangle + \langle \Psi_k^{\text{out}} | (E_s - H_o + i\varepsilon)^{-1} V | \Psi_s^+ \rangle + \langle \Psi_k^{\text{out}} | V (E_k - H + i\varepsilon)^{-1} | \Psi_s^+ \rangle, \quad (2.34)$$

if the rightmost ket above is taken to represent the left hand side of equation (2.31). Recognizing that  $\Psi_k^{\text{out}}$  is an eigenfunction of  $H_o$  and that  $\Psi_s^+$  is an eigenfunction of  $H$ , (2.34) becomes

$$S_{ks} = \delta_{ks} + (E_s - E_k - i\varepsilon)^{-1} \langle \Psi_k^{\text{out}} | V | \Psi_s^+ \rangle + (E_k - E_s + i\varepsilon)^{-1} \langle \Psi_k^{\text{out}} | V | \Psi_s^+ \rangle. \quad (2.35)$$

This may be factored to obtain

$$S_{ks} = \delta_{ks} + \left( \frac{1}{E_k - E_s + i\varepsilon} - \frac{1}{E_k - E_s - i\varepsilon} \right) \langle \Psi_k^{\text{out}} | V | \Psi_s^+ \rangle, \quad (2.36)$$

where the remaining inner product is taken to be the transition matrix element  $T_{ks}$ . Formally there are two representations for  $T$  given by:

$$\begin{aligned}T_{ks}^+ &\equiv \langle \Psi_k^{\text{out}} | V | \Psi_s^+ \rangle \\ T_{ks}^- &\equiv \langle \Psi_k^- | V | \Psi_s^{\text{in}} \rangle.\end{aligned}\quad (2.37)$$

When the energy eigenvalues differ,  $k \neq s$ , the matrix elements are referred to as being *half-off-the-energy-shell* and are so indicated with the use of the appropriate superscript,  $\pm$ . If the energies are the same, however, the two formulations yield the same *on-the-energy-shell* value and the superscript is dropped. For our purposes we shall be utilizing only the top form and therefore relax our notation somewhat by dropping the superscript,  $T^+ \rightarrow T$  even for off-shell elements. Using the mathematical identity:

$$\frac{1}{x - x_o \pm i\varepsilon} = \frac{P}{x - x_o} \mp i\pi\delta(x - x_o), \quad (2.38)$$

where the operator  $P$  is defined as the Cauchy principal value, we see that the term given in the parentheses of (2.36) may be replaced by  $2\pi i\delta(E_k - E_s)$  to yield the relation

$$S_{ks} = \delta_{ks} - i2\pi\delta(E_k - E_s)T_{ks}. \quad (2.39)$$

The delta function in (2.39) allows only the on-shell  $T$  matrix elements to contribute. We see from this relation that having the on-shell terms of the transition matrix is equivalent to knowledge of the scattering matrix and thus provides a time independent, asymptotic, scattering picture. To deduce characteristics within the scattering region, such as the wave function there for example, we must have the additional half-off-shell terms of the transition matrix.

## 2.2 Additional Developments

The original work of [13] is applicable as it stands only to single-particle scattering or at best two-particle scattering as viewed from a center of mass frame. Six years later Lippmann published an additional paper [16] building on previous work in an effort to produce multi-channel multi-particle Lippmann-Schwinger equations appropriate for more complicated collision problems. Others also followed suit, such as Ekstein [17] and Gerjuoy [18], but their formalisms were mathematically unsound and plagued by spurious solutions when applied to scattering with any more than two particles. Faddeev was the first to offer a unique three-particle solution based on coupled integral equations in 1960 [19]. In 1962 Mitra published a paper [20] showing that the three-particle problem could be reduced to three one-body integral equations by decomposing the wave function into three components. It was soon realized that these two formalisms coincided, which served to stimulate a great deal of interest, as well as considerable advancements, in multichannel scattering in the years to follow.

The Fredholm theory was first applied to quantum scattering in a discussion on the convergence of the Born approximation by Res Jost and Abraham Pais [21]. The Born approximation is simply a

truncated Neumann series solution, which was the preferred solution method of the time. Rewriting (2.4) in operator notation,

$$T = V + VG_E^\pm T, \quad (2.40)$$

the first approximation is made by truncating the second term on the right hand side. Successive approximations are then obtained by substituting previous ones in place of  $T$  in the initially dropped term:

$$\begin{aligned} T_1 &= V, \\ T_2 &= V + VG_E^\pm V, \\ T_3 &= V + VG_E^\pm V + VG_E^\pm VG_E^\pm V, \\ T_4 &= V + VG_E^\pm V + VG_E^\pm VG_E^\pm V + VG_E^\pm VG_E^\pm VG_E^\pm V, \\ &\vdots \\ T_n &= V + VG_E^\pm T_{n-1} = \sum_{i=0}^{n-1} (VG_E^\pm)^i V. \end{aligned} \quad (2.41)$$

Jost and Pais found that the Fredholm theory of integral equations made it possible to express solutions as a quotient of infinite power series in  $\lambda$  which still converge when the Born expansion breaks down. Using the theory they rewrite (2.1) as

$$\Psi(\mathbf{r}) = \varphi(\mathbf{r}) + \lambda \int \frac{\Delta(\lambda; \mathbf{r}, \mathbf{r}')}{\Delta(\lambda)} \varphi(\mathbf{r}') d\mathbf{r}' \quad (2.42)$$

where

$$\begin{aligned} \Delta(\lambda; \mathbf{r}, \mathbf{r}') &= K(\mathbf{r}, \mathbf{r}') \\ &+ \sum_{n=1}^{\infty} \frac{(-\lambda^n)}{n!} \int d\mathbf{r}_1 \cdots \int d\mathbf{r}_n \begin{vmatrix} K(\mathbf{r}, \mathbf{r}') & K(\mathbf{r}, \mathbf{r}_1) & K(\mathbf{r}, \mathbf{r}_2) & \cdots & K(\mathbf{r}, \mathbf{r}_n) \\ K(\mathbf{r}_1, \mathbf{r}') & 0 & K(\mathbf{r}_1, \mathbf{r}_2) & \cdots & K(\mathbf{r}_1, \mathbf{r}_n) \\ K(\mathbf{r}_2, \mathbf{r}') & K(\mathbf{r}_2, \mathbf{r}_1) & 0 & \cdots & K(\mathbf{r}_2, \mathbf{r}_n) \\ \vdots & \vdots & \vdots & \ddots & \vdots \\ K(\mathbf{r}, \mathbf{r}') & K(\mathbf{r}, \mathbf{r}') & K(\mathbf{r}, \mathbf{r}') & \cdots & 0 \end{vmatrix} \end{aligned} \quad (2.43)$$

and

$$\Delta(\lambda) = 1 + \sum_{n=1}^{\infty} \frac{(-\lambda^n)}{n!} \int dr_1 \cdots \int dr_n \begin{vmatrix} 0 & K(\mathbf{r}_1, \mathbf{r}_2) & K(\mathbf{r}_1, \mathbf{r}_3) & \cdots & K(\mathbf{r}_1, \mathbf{r}_n) \\ K(\mathbf{r}_2, \mathbf{r}_1) & 0 & K(\mathbf{r}_2, \mathbf{r}_3) & \cdots & K(\mathbf{r}_2, \mathbf{r}_n) \\ K(\mathbf{r}_3, \mathbf{r}_1) & K(\mathbf{r}_3, \mathbf{r}_2) & 0 & \cdots & K(\mathbf{r}_3, \mathbf{r}_n) \\ \vdots & \vdots & \vdots & \ddots & \vdots \\ K(\mathbf{r}_n, \mathbf{r}_1) & K(\mathbf{r}_n, \mathbf{r}_2) & K(\mathbf{r}_n, \mathbf{r}_3) & \cdots & 0 \end{vmatrix} \quad (2.44)$$

which are given as equations ([21]-{48, 49, 50}).

Interest of the scientific community in Fredholm's method was again rekindled with a remark made by Schwinger in 1954 [22]. Subsequent development by Baker of this idea showed the direct relationship between the phase of the partial-wave Fredholm determinant and the potential-scattering phase shift [23]. In 1970 Reinhardt and Szabo suggested a procedure for calculating phase shifts which depends upon the solution of an integral equation derived from the partial-wave LS equation thereby reducing the calculation of the phase shift to the evaluation of a single finite-dimensional determinant [24]. The following year, Walters solved an integral equation derived from the LS equation for the full wave function which was not based on a partial wave expansion [25]. His method, however, was adapted only to central potentials. Solutions were obtained by conversion to matrix form through the use of numerical quadrature for a screened Coulomb potential,

$$V(r) = -\frac{C e^{-r}}{r}, \quad (2.45)$$

given as ([25]-28).

At that period in time a mismatch existed between the state of computers and the level of mathematical sophistication, putting the possibility of a multidimensional calculation out of reach.

### 2.2.1 Hard Potentials

First attempts at scattering from noncentral potentials would be carried out in coordinate space for scatterers with well defined boundary conditions. This entailed the potential strength being either zero or infinite with the interface falling on a simple geometrical contour. In this way the wave function must identically vanish on the boundaries and is propagated elsewhere via the free particle Green's function. We make references to two such papers [26, 27] in our work so we outline briefly the variation on the Korringa-Kohn-Rostoker (KKR) method chosen by the authors to solve the problem of scattering from hard discs.

### A Survey of the Gaspard-Rice Calculation

We begin by writing the solution to the Schrödinger/Helmholtz equation,

$$[\nabla^2 + k_o^2] \Psi(\mathbf{r}) = U(\mathbf{r})\Psi(\mathbf{r}); \quad U = \frac{2\mu V}{\hbar^2}, \quad (2.46)$$

with the aid of appendix A, in terms of an integral equation of the proper Green's function,

$$\Psi_{k_o}(\mathbf{r}) = \varphi_{k_o}(\mathbf{r}) + \int G_{k_o}(\mathbf{r}, \mathbf{r}') U(\mathbf{r}') \Psi_{k_o}(\mathbf{r}') d\mathbf{r}'; \quad [\nabla^2 + k_o^2] \varphi_{k_o}(\mathbf{r}) = 0, \quad (2.47)$$

which satisfies the point source equation,

$$(\nabla^2 + k_o^2) G_{k_o}(\mathbf{r}, \mathbf{r}') = \delta(\mathbf{r} - \mathbf{r}'). \quad (2.48)$$

We recognize (2.47) as being a general solution to the second order differential equation (2.46) in that it contains the homogeneous solution, given by  $\varphi_{k_o}(\mathbf{r})$ , followed by a particular solution. This has the correct form and will return the free particle state as the interaction is turned off,  $V \rightarrow 0$ .

We also cast Green's theorem,

$$\int (\Psi \nabla^2 G - G \nabla^2 \Psi) dv = \int (\Psi \nabla G - G \nabla \Psi) \cdot \hat{\mathbf{n}} da, \quad (2.49)$$

into two-dimensional form,

$$\int (\Psi(\mathbf{r}') \nabla'^2 G(\mathbf{r}, \mathbf{r}') - G(\mathbf{r}, \mathbf{r}') \nabla'^2 \Psi(\mathbf{r}')) da' = \oint (\Psi(\mathbf{r}') \nabla' G(\mathbf{r}, \mathbf{r}') - G(\mathbf{r}, \mathbf{r}') \nabla' \Psi(\mathbf{r}')) \cdot \hat{\mathbf{n}} ds' \quad (2.50)$$

to reflect the dimensionality of the problem. Because the wave function must vanish on the edges of the hard discs, the integration on the left hand side of (2.50) is carried out over an area that excludes the discs and falls within a contour that encircles them. The line integration of the right hand side must be carried out over the edges of all the discs in addition to the closing contour which is to be extended to asymptotic distances where the wave function falls off to negligible values. The Laplacians appearing on the left hand side of the above equation can be found from equations (2.46) and (2.48) if we keep in mind that the potential is zero everywhere outside of the hard disks and the symmetry property of the Green's function with respect to variable interchange,

$$\begin{aligned} (\nabla'^2 + k_o^2) \Psi(\mathbf{r}') = 0 &\longrightarrow \nabla'^2 \Psi(\mathbf{r}') = -k_o^2 \Psi(\mathbf{r}') \\ (\nabla'^2 + k_o^2) G(\mathbf{r}, \mathbf{r}') = \delta(\mathbf{r} - \mathbf{r}') &\longrightarrow \nabla'^2 G(\mathbf{r}, \mathbf{r}') = \delta(\mathbf{r} - \mathbf{r}') - k_o^2 G(\mathbf{r}, \mathbf{r}'). \end{aligned} \quad (2.51)$$

An expression valid within the region occupied by the hard disks is not needed, for the wave function must vanish where  $V = \infty$ . Plugging these expressions back into (2.50), the left hand side of that

equation becomes

$$\begin{aligned} & \int \Psi(\mathbf{r}') (\delta(\mathbf{r} - \mathbf{r}') - k_0^2 G(\mathbf{r}, \mathbf{r}')) d^2 r' - \int G(\mathbf{r}, \mathbf{r}') (-k_0^2 \Psi(\mathbf{r}')) d^2 r' \\ &= \int \Psi(\mathbf{r}') \delta(\mathbf{r} - \mathbf{r}') d^2 r' - \int \Psi(\mathbf{r}') k_0^2 G(\mathbf{r}, \mathbf{r}') d^2 r' + \int G(\mathbf{r}, \mathbf{r}') k_0^2 \Psi(\mathbf{r}') d^2 r'. \end{aligned} \quad (2.52)$$

As the terms in the last two integrands commute, we may cancel those integrals so that equation (2.50) now appears as

$$\int \Psi(\mathbf{r}') \delta(\mathbf{r} - \mathbf{r}') d^2 r' = \oint (\Psi(\mathbf{r}') \nabla' G(\mathbf{r}, \mathbf{r}') - G(\mathbf{r}, \mathbf{r}') \nabla' \Psi(\mathbf{r}')) \cdot \hat{\mathbf{n}} ds'. \quad (2.53)$$

If  $r$  is allowed to describe a point at the interface with the hard disks on which the wave function must vanish the left side of (2.53) drops out. The right side in turn must be evaluated along the full contour consisting of all three disk interfaces, indicated by  $\odot$ , as well as at infinity where the domain is closed,

$$0 = - \oint_{\odot} G(\mathbf{r}, \mathbf{r}') \nabla' \Psi(\mathbf{r}') \cdot \hat{\mathbf{n}} ds' + \oint_{\infty} (\Psi(\mathbf{r}') \nabla' G(\mathbf{r}, \mathbf{r}') - G(\mathbf{r}, \mathbf{r}') \nabla' \Psi(\mathbf{r}')) \cdot \hat{\mathbf{n}} ds'. \quad (2.54)$$

As the scattering is described at asymptotically large distances from the disks,  $r$  is also taken to approach infinity where the left side of (2.53) now becomes the wave function there and the right side must again be evaluated in the same manner,

$$\Psi(\mathbf{r}) = - \oint_{\odot} G(\mathbf{r}, \mathbf{r}') \nabla' \Psi(\mathbf{r}') \cdot \hat{\mathbf{n}} ds' + \oint_{\infty} (\Psi(\mathbf{r}') \nabla' G(\mathbf{r}, \mathbf{r}') - G(\mathbf{r}, \mathbf{r}') \nabla' \Psi(\mathbf{r}')) \cdot \hat{\mathbf{n}} ds'. \quad (2.55)$$

The Green's function takes on the free particle form,

$$G(\mathbf{r}, \mathbf{r}') = -\frac{i}{4} H_0^{(1)}(k|\mathbf{r} - \mathbf{r}'|) \xrightarrow{r' \rightarrow \infty} \frac{e^{i(k|\mathbf{r} - \mathbf{r}'| - \pi/4)}}{2i\sqrt{2\pi k|\mathbf{r} - \mathbf{r}'|}}, \quad (2.56)$$

which is proportional to the zeroth order Hankel function of the first kind, but the gradient of the wave function at the disk interface is as yet unknown. This is handled by using the additional equation, (2.54), to help deduce an expression for the gradient.

The free propagator (2.56) is expanded using the addition theorem for Bessel functions and the polar angles of the position vectors,

$$G(\mathbf{r}, \mathbf{r}') = \frac{1}{4i} \sum_{m=-\infty}^{\infty} H_m^{(1)}(kr') J_m(kr) e^{im(\phi - \phi')}. \quad (2.57)$$

Since  $\nabla G$  is only needed when integrating over the contour at infinity,  $r$  is fixed on a disk boundary so that we may use (2.54) and  $r' \rightarrow \infty$  giving the asymptotic form,

$$\lim_{r' \rightarrow \infty} G(\mathbf{r}, \mathbf{r}') = \frac{1}{2i\sqrt{2\pi kr'}} \sum_{m=-\infty}^{\infty} e^{i[kr' - m\pi/2 - \pi/4]} J_m(kr) e^{im(\phi - \phi')} \quad (2.58)$$

The gradient may now be taken directly,  $\nabla G \simeq ik\nabla G$ , and the asymptotic behavior of the wave function for large  $r'$  is given in terms of the  $S$  matrix [10],

$$\Psi_{kl}(\mathbf{r}') \simeq \frac{1}{\sqrt{2\pi kr'}} \sum_{l'=-\infty}^{\infty} \left[ e^{-i[kr' - l'\pi/2 - \pi/4]} \delta_{ll'} + S_{ll'} e^{i[kr' - l'\pi/2 - \pi/4]} \right] e^{il'\phi}. \quad (2.59)$$

With this information, the right most integral of the homogeneous equation (2.54) may be evaluated and set equal to the left integral which in turn is the unknown expression needed for (2.55). Gaspard and Rice, however, did not take the additional step to calculate the wave function. What they sought were resonances and cross sections so steps are tailored to provide this information.

The gradient of the wave function is given a representation,

$$\nabla' \Psi(\mathbf{r}') \cdot \hat{\mathbf{n}} = \sum_{m=-\infty}^{\infty} A_{lm} e^{im\theta}, \quad (2.60)$$

determined by periodic boundary conditions [28]. Expressions for the nonzero terms of (2.54) are expanded in terms of Bessel and Hankel functions with  $\mathbf{r}$  set to a disk boundary. With this information  $\mathbf{A}$  is obtained and similar steps may be repeated for (2.55) with  $\mathbf{r}$  set to large distances obtaining an expression for the wave function. This expression is then compared to the asymptotic form given by (2.59) to identify the  $S$  matrix,

$$S_{ll'} = \delta_{ll'} + i\pi a \sum_{j=1}^3 \sum_{m=-\infty}^{\infty} A_{ljm} e^{-il'\phi} J_{l'-m}(ks) J_m(ka) = \delta_{ll'} - i \sum_{j=1}^3 \sum_{m=-\infty}^{\infty} A_{ljm} D_{ljm}. \quad (2.61)$$

where  $j$  indexes the disks,  $a$  is the radius, and  $s$  the distance to their centers from a centered origin. In matrix notation this is

$$\mathbf{S} = \mathbf{I} - i\mathbf{A}\mathbf{D}, \quad (2.62)$$

where  $\mathbf{A}$  takes on a rather complicated form and is given in the paper [26].

## 2.2.2 Computations on Parallel Processors

By the late 1990's, supercomputers had been enlisted to square off against the noncentral multidimensional scattering problem [29, 30]. Highly refined parallel solvers were then subsequently utilized to investigate electron transmission through water in 2000 [31].

### Resonance Tunneling Through Water

Of particular interest are results by Peskin *et al.* [32] suggesting electron tunneling enhancement by resonances. They carried out their simulations on a cell holding 197 water molecules arranged

in three monolayers held between flat platinum electrodes separated by a distance of 10Å. Electron scattering wave functions were calculated in three dimensions and the effectiveness of the tunneling through the water monolayers was determined from probability densities.

Water molecules were allowed to thermally equilibrate, thereby creating representatives of a statistical ensemble, and then frozen, meaning that the electron dynamics are assumed to take place on a much shorter time scale than those of the molecules. The authors found that tunneling probabilities were in fact strongly peaked functions of the incident electron energy. Upon investigation of the energies of two such peaks for a specific frozen water configuration, it was found that probability densities for the electron within the water were several times larger than that found within the incident wave, suggesting resonances.

In the frozen water picture, transient structures, consisting of molecular cavities formed between repulsive oxygen cores, become static and allow for these resonances. Figures [32]-{5, 6} give the contour plots for the position probability of the transmitted electron as an overlay with the locations of the oxygen atoms, which are represented by Gaussians. It is evident from these figures that the electron probability peaks coincide with the molecular cavities at these energies of presumed resonance.

To verify the resonances, and also to determine their lifetime, eigenvalues were sought in the complex energy plane. Because the authors chose coordinate space for their computations, the resulting procedure is a little awkward. This is due to the difficulty of imposing a purely outgoing wave, or Sigert, boundary condition. Their method was to add a highly absorptive piece to the potential,

$$i\epsilon(z) = i\epsilon_o \left( \frac{2|z|}{L_z} \right)^7, \quad (2.63)$$

given by ([32]-5), which is localized to the boundaries of the tunneling axis to diminish the reflected wave component. Because for a given value of the absorption parameter there will still be a small reflected portion of the wave, the complex energy eigenvalues will in general be dependent on this parameter. At resonance, however, this dependency diminishes. Resonances were thus determined by a convergence of the energy eigenstates to fixed values which are independent of the absorption parameter.

The resonances were found to coincide with those energies, lying low in the potential, for which tunneling was enhanced by many orders of magnitude. Due to the complicated potential, however, the associated wave mechanics are difficult to analyze. A much simpler potential structure in our work allows us to see how the transmitted electron is able to negotiate its way between resonant cavities. It is shown in this thesis that a particle's wave function, at energies near low lying resonances,

is able to penetrate narrow passages by squeezing itself in the appropriate direction. Working with relatively simple potentials also afforded us the added benefit of being able to show that the symmetry characteristics of the wave function inside the potential at narrow, low-lying resonances reflect the symmetry of the potential itself.

## 2.3 Discrete Momentum Representation

We chose to work in momentum space to avoid two of the difficulties associated with the application of boundary conditions in the problem we chose to investigate. First, the task of assigning an outgoing wave boundary condition, prior to evaluating the Fredholm determinant for resonances, is greatly simplified in momentum space by simply choosing an integration contour as shown in section 3.2.1. The second concerns our choice of a soft potential. In coordinate space, such a potential supports an exponentially decaying solution in regions where the potential exceeds the energy. Tiny errors, or numerical uncertainties, in these regions then exponentially diverge from the wave function as the solution is propagated in a direction of decreasing potential strength. For this reason, its Fourier transform space is better suited for the scattering problem.

Because we further choose to scatter from a two-dimensional potential which does not commute with the angular momentum operator,  $[L, V] \neq 0$ , the standard partial wave expansion method offers little advantage. We thus chose to solve Schrödinger's equation in the full multi-dimensional momentum space. The first publication with an implementation of such a solution appeared in 2000 [33]. The procedure is referred to as the *Discrete Momentum Representation* (DMR) method and is credited to Polášek *et al.* We make use of the same procedure, which was implemented by the author of this thesis a year earlier, after a referral by R. H. Landau to the eighteenth chapter of his book [34]. In more recent publications the DMR method has been applied to different variations of a potential model [35, 36, 37, 38]. These publications, however, contain no calculations of wave functions or resonances. The first three DMR papers above use scaled radial coordinates with a long range cutoff to ensure convergence of a screened Coulomb potential that falls off more slowly than ours. The treatment of the singularities and principal value integrations is similar to that of Walters [25] and Sloan [39]. The fourth paper [37] presents a method for calculating the matrix elements between two plane waves interacting with a molecular Coulombic field, and the last deals with inelastic electron scattering on polyatomic molecules.

### 2.3.1 Literature Search

The paper [33] served as the starting point for the final phase of my literature search. Being the first published documentation of the DMR method, I searched forward in time using the Science Citation Index (*ISI Web of Science*<sup>®</sup>). This was a cascading search meaning that any successful outcomes were in turn similarly investigated, as were the references of these later papers. The term *Discrete Momentum Representation*, adopted by Polášek *et al.* to represent this particular method, was then additionally searched as a key phrase in the *INSPEC* and *Academic Search Premier* databases. Similar searches were performed on other key papers such as Peskin *et al.* [32].

## Chapter 3

# Exact Quantum Theory

### 3.1 Basic Equations

For a given potential  $V$  the scattering solutions to the time-independent Schrödinger equation,

$$(H_o + V)|\Psi\rangle = E|\Psi\rangle, \quad (3.1)$$

may be written in terms of a Green's function,  $G_E$ , by first introducing the unscattered wave  $|\varphi_{\mathbf{k}_o}\rangle = e^{i\mathbf{k}_o \cdot \mathbf{r}}/2\pi$  as a boundary condition,

$$|\Psi_{\mathbf{k}_o}\rangle = |\varphi_{\mathbf{k}_o}\rangle + G_E V |\Psi_{\mathbf{k}_o}\rangle; \quad G_E \equiv (E - H_o)^{-1}. \quad (3.2)$$

Explicit steps are outlined in appendix A. An outwardly scattered wave is imposed as the additional boundary condition by adding a small imaginary energy  $i\varepsilon$  to  $E$  in (3.2). A superscript is added to the resulting Green's function and wave function to reflect this choice. By introducing the transition matrix  $T$  for outward scattering, the previous equations may now be written more compactly:

$$|\Psi_{\mathbf{k}_o}^+\rangle = |\varphi_{\mathbf{k}_o}\rangle + G_E^+ T |\varphi_{\mathbf{k}_o}\rangle, \quad G_E^+ \equiv (E - H_o + i\varepsilon)^{-1}, \quad T |\varphi_{\mathbf{k}_o}\rangle = V |\Psi_{\mathbf{k}_o}^+\rangle. \quad (3.3)$$

To find the wave function we first find  $T$  by allowing the potential to operate on (3.2) from the left,

$$T |\varphi_{\mathbf{k}_o}\rangle = V |\varphi_{\mathbf{k}_o}\rangle + V G_E^+ T |\varphi_{\mathbf{k}_o}\rangle, \quad (3.4)$$

yielding a solution in terms of the Møller wave operator,

$$T = \Omega V; \quad \Omega \equiv (I - V G_E^+)^{-1}. \quad (3.5)$$

In terms of this new wave operator, (3.3) is expressible in its most concise form,

$$|\Psi_{\mathbf{k}_0}^+\rangle = \Omega|\varphi_{\mathbf{k}_0}\rangle. \quad (3.6)$$

This follows by using the operator equation

$$V = (I - VG_E^+)T, \quad (3.7)$$

deduced from (3.4), to eliminate  $T$  from

$$|\Psi_{\mathbf{k}_0}^+\rangle = (I + G_E^+T)|\varphi_{\mathbf{k}_0}\rangle, \quad (3.8)$$

which follows from (3.3). For an expanded treatment see a text on collision theory [10, 40, 41]. From the wave function, the current density and velocity field,

$$\mathbf{J}(\mathbf{r}) = \frac{\hbar}{2\mu i} [\Psi^*(\mathbf{r})\nabla\Psi(\mathbf{r}) - \Psi(\mathbf{r})\nabla\Psi^*(\mathbf{r})], \quad (3.9)$$

$$\mathbf{v}(\mathbf{r}) = \mathbf{J}(\mathbf{r})/[\Psi^*(\mathbf{r})\Psi(\mathbf{r})], \quad (3.10)$$

may also be calculated. As the scattering amplitudes are proportional to the transition matrix elements,

$$f_{\mathbf{k}\mathbf{k}_0} \propto T_{\mathbf{k}\mathbf{k}_0}, \quad (3.11)$$

solving (3.5) allows computation of both the differential and total cross sections.

The system's resonances correspond to complex energies for which  $\Omega$  is singular,

$$|\Omega_E^{-1}| = 0; \quad E \in \mathcal{Z}. \quad (3.12)$$

To better understand the added information this generalization provides, consider the consequence of an imaginary part added to the energy,

$$E = E_r \pm iE_i = E_r \pm i\Gamma/2; \quad 0 < E_r, \quad 0 < \Gamma, \quad (3.13)$$

by investigating how it affects the time dependence of a quantum state,

$$\Psi(t) \propto e^{-iEt/\hbar} = e^{-iE_r t/\hbar} e^{\pm\Gamma t/2\hbar}. \quad (3.14)$$

We see that the imaginary energy leads to a probability density,

$$|\Psi|^2 \propto e^{\pm\Gamma t/\hbar}, \quad (3.15)$$

that either grows or decays exponentially with time. Choosing the negative imaginary energy solution for a resonance, so that the probability density remains bounded, we are able to assign a lifetime parameter,  $\tau$ , such that

$$|\Psi|^2 \propto e^{-t/\tau}; \quad \tau = \frac{\hbar}{\Gamma}. \quad (3.16)$$

From Heisenberg's relation,

$$\Delta E \Delta t \geq \frac{\hbar}{2}, \quad (3.17)$$

we find that poles with larger  $\Gamma$  mark resonance states with shorter lifetimes which must be spread over a broader range of energies.

## 3.2 Representations of Equations

Operating on (3.4) from the left with the free-particle wave function in a basis of  $\delta$ -function normalized momentum eigenstates,  $|\mathbf{k}\rangle$ , and rearranging terms, gives

$$\langle \mathbf{k} | V | \mathbf{k}_o \rangle = \langle \mathbf{k} | T | \mathbf{k}_o \rangle - \int \frac{\langle \mathbf{k} | V | \mathbf{k}' \rangle \langle \mathbf{k}' | T | \mathbf{k}_o \rangle}{E(\mathbf{k}_o) - H_o(\mathbf{k}') + i\epsilon} d\mathbf{k}', \quad (3.18)$$

where we have used the closure identity. For a free particle Hamiltonian,

$$H_o(\mathbf{k}) = \frac{\mathbf{p}^2}{2\mu} = \frac{\hbar^2 k^2}{2\mu}; \quad k \equiv \sqrt{\mathbf{k}^2}, \quad (3.19)$$

the poles of (3.18) depend only on the magnitude of the momentum,  $k$ .

Since the energy is proportional to the square of the momentum, we are faced with a choice of two roots to use in our quest for poles (3.12). To decide which root to choose we write the incident momentum in the complex form

$$k_o \Rightarrow k_o e^{i\theta} = k_o (\cos \theta + i \sin \theta). \quad (3.20)$$

Then the energy appears in terms of doubled angles,

$$E = \frac{\hbar^2 k_o^2}{2\mu} \Rightarrow \frac{\hbar^2}{2\mu} k_o^2 e^{i2\theta} = \frac{\hbar^2}{2\mu} k_o^2 (\cos 2\theta + i \sin 2\theta). \quad (3.21)$$

We require that the real part of the energy be positive and the imaginary part be negative. This condition is satisfied with  $k_o$  falling in the fourth ( $3\pi/4 < \theta < \pi$ ) or eighth ( $7\pi/4 < \theta < 2\pi$ ) octant which can be visualized easily with the aid of figure 3.1. Because the real part of  $k_o$  is negative in the fourth octant, we focus our attention on values of  $k_o$  falling in the eighth octant when doing the analytical continuation. This rules out values of energy located on the first Riemann sheet of the complex energy plane in favor of those falling in the fourth quadrant of the second sheet.

Specializing to two dimensions, we simplify computations by choosing a polar representation in terms of  $k$  and the scattering angle,  $\theta$ . The explicit polar representation of the matrix elements of (3.18) is

$$V(k, \theta; k_o, \theta_o) = T(k, \theta; k_o, \theta_o) - \frac{2\mu}{\hbar^2} \int_0^{2\pi} \int_0^\infty \frac{V(k, \theta; k', \theta') T(k', \theta'; k_o, \theta_o)}{k_o^2 - k'^2 + i\epsilon} k' dk' d\theta'. \quad (3.22)$$

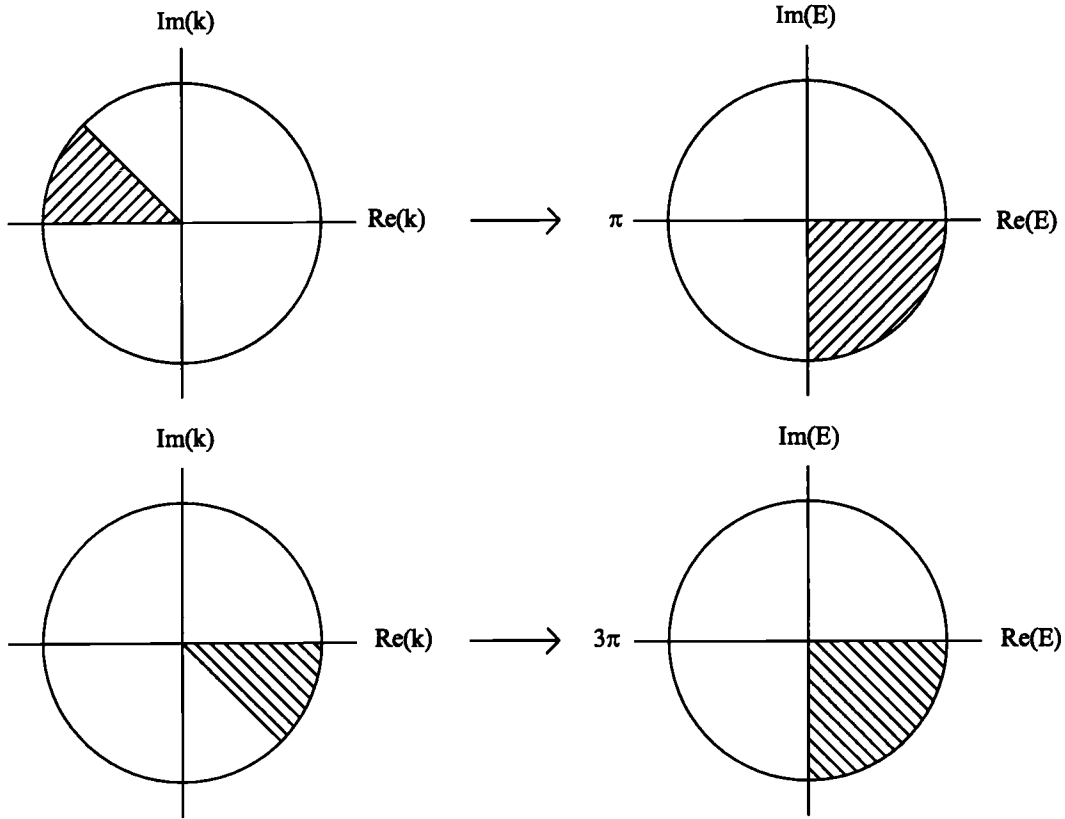


Figure 3.1: Complex momenta,  $k$ , of the fourth (top left) and eighth (bottom left) octants map to energies,  $E$ , in the fourth quadrant of the first (top right) and second (bottom right) Riemann sheets.

Similarly, (3.3) may be projected onto a coordinate basis,  $|\mathbf{r}\rangle$ ,

$$\langle \mathbf{r} | \Psi_{\mathbf{k}_o}^+ \rangle = \langle \mathbf{r} | \varphi \rangle + \frac{2\mu}{\hbar^2} \int \frac{\langle \mathbf{r} | \mathbf{k}' \rangle}{k_o^2 - k'^2 + i\epsilon} \langle \mathbf{k}' | T | \varphi \rangle d\mathbf{k}', \quad (3.23)$$

to arrive at an expression for the wave function,  $\Psi_{\mathbf{k}_o}^+(\mathbf{r}) \equiv \langle \mathbf{r} | \Psi_{\mathbf{k}_o}^+ \rangle$ ,

$$\Psi_{\mathbf{k}_o}^+(\mathbf{r}) = \frac{e^{i\mathbf{k}_o \cdot \mathbf{r}}}{2\pi} + \frac{\mu}{\pi \hbar^2} \int_0^{2\pi} \int_0^\infty \frac{e^{i\mathbf{k}' \cdot \mathbf{r}}}{k_o^2 - k'^2 + i\epsilon} T(k', \theta'; k_o, \theta_o) k' dk' d\theta'. \quad (3.24)$$

In two dimensions the propagator for the Helmholtz equation is proportional to the Hankel function of the first kind and order zero [42, 43].

$$G_{\mathbf{k}_o}^+(\mathbf{r}, \mathbf{r}') = \frac{\hbar^2}{2\mu} G_E^+(\mathbf{r}, \mathbf{r}') = \frac{1}{4i} H_o^{(1)}(k_o |\mathbf{r} - \mathbf{r}'|) \rightarrow \begin{cases} \frac{1}{2\pi} \ln(k_o |\mathbf{r} - \mathbf{r}'|) & : |\mathbf{r} - \mathbf{r}'| \rightarrow 0 \\ \frac{e^{i(k_o |\mathbf{r} - \mathbf{r}'| - \pi/4)}}{2i \sqrt{2\pi k_o |\mathbf{r} - \mathbf{r}'|}} & : |\mathbf{r} - \mathbf{r}'| \rightarrow \infty. \end{cases} \quad (3.25)$$

If the asymptotic form of this propagator is applied to (3.24) and the result then compared to the asymptotic form of the scattered wave,

$$\lim_{r \rightarrow \infty} \Psi_{\mathbf{k}_o}^+(\mathbf{r}) = \frac{1}{2\pi} \left[ e^{i\mathbf{k}_o \cdot \mathbf{r}} + \frac{f_{k_o}(\theta) e^{ik_o r}}{\sqrt{r}} \right], \quad (3.26)$$

the relationship between the scattering amplitude and transition matrix is revealed,

$$f_{k_o}(\theta) = -\frac{2\pi\mu}{\hbar^2} \sqrt{\frac{\pi}{k_o}} (1+i) T(\mathbf{k}, \mathbf{k}_o). \quad (3.27)$$

The steps have been detailed in appendix B. It follows, as is shown in appendix C, that the differential cross section in two-dimensional space is

$$\frac{d\lambda}{d\theta} = |f_{k_o}(\theta)|^2 = \frac{8\pi^3\mu^2}{\hbar^4 k_o} |T(\mathbf{k}, \mathbf{k}_o)|^2. \quad (3.28)$$

Because the cross section in two dimensions has units of length,  $\lambda$  is used here.

### 3.2.1 Migrating Poles

The adding of a small imaginary energy to  $E$  in (3.2) amounts to a prescription for how to distort the contour into the complex plane to avoid the pole which falls on the path of integration. From the resulting form of the radial integration,

$$\int_0^\infty \frac{f(k')}{k_o^2 - k'^2 + i\epsilon} dk', \quad (3.29)$$

two simple poles are evident upon factoring the denominator,

$$z^2 = k_o^2 + i\epsilon \implies z = \pm(k_o + i\epsilon), \quad (3.30)$$

only one of which need be considered ( $0 < k'$ ). We notice that this pole ( $k_o + i\epsilon$ ) will now reside just above the real line. Alternatively one can think of distorting the radial integration paths counterclockwise in the complex, not angular, direction about  $k' = k_o$  in the form of a small semicircle that encapsulates the pole as shown in figure 3.2. Evaluation is carried out as a limiting process where the pole is moved back to the real line, or the radius,  $\rho$ , of the small half-circle is allowed to shrink to zero,  $\rho \rightarrow 0$ . The way in which the pole is displaced from, and then moved back to, the real line is equivalent to the boundary condition that must be explicitly specified when dealing with equations written in differential form.

If one could guarantee the right asymptotic behavior, a closed contour could be established and (3.29) evaluated using Cauchy's theorem. We desire, however, the freedom to work with a wide

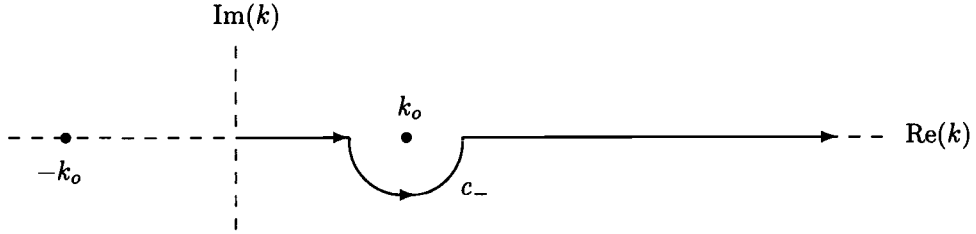


Figure 3.2: Radial integration contour specified with a  $+i\epsilon$  prescription.

variety of potentials for which a closed form technique may not always be possible. For this reason, direct evaluation is carried out numerically,

$$\int_0^{\infty} \frac{f(k')}{k_o^2 - k'^2 + i\epsilon} dk' = P \int_0^{\infty} \frac{f(k')}{k_o^2 - k'^2} dk' + \int_{c_-} \frac{f(z')}{k_o^2 - z'^2} dz', \quad (3.31)$$

where 'P' is understood to be the Cauchy principal value operator. Carrying out the evaluation of the limiting process on the semicircular  $c_-$  contour, in which we move around the pole at  $k_o$  in the counterclockwise direction, we may write

$$\int_0^{\infty} \frac{f(k')}{k_o^2 - k'^2 + i\epsilon} dk' = P \int_0^{\infty} \frac{f(k')}{k_o^2 - k'^2} dk' - i\pi R(k_o). \quad (3.32)$$

Here  $R$  is the residue of the pole at its argument, which is evaluated to yield

$$\int_0^{\infty} \frac{f(k')}{k_o^2 - k'^2 + i\epsilon} dk' = P \int_0^{\infty} \frac{f(k')}{k_o^2 - k'^2} dk' - i\pi \frac{f(k_o)}{2k_o}. \quad (3.33)$$

An alternate approach would be to utilize energy representation. With a change of variables,

$$dk = \frac{2\mu}{\hbar^2} \frac{dE}{2k}, \quad (3.34)$$

followed by letting the energy be complex about our infinitesimal semicircle centered at  $E_o = \hbar^2 k_o^2 / 2\mu$ ,

$$E \Rightarrow E_o + \rho e^{i\phi}, \quad (3.35)$$

we may equate the integrals

$$\int_{c_-} \frac{f(z')}{k_o^2 - z'^2} dz' = \lim_{\rho \rightarrow 0} \frac{1}{2k_o} \int_{\pi}^{2\pi} \frac{f(E_o - \rho e^{i\phi})}{-\rho e^{i\phi}} i\rho e^{i\phi} d\phi. \quad (3.36)$$

Upon evaluation and reinsertion into (3.31), this will again produce the desired result (3.33).

## Chapter 4

# Numerical Methods

To find discretized approximations to our equations that could be implemented on computers, we constructed a polar grid in momentum space having mesh points  $(k_i, \theta_j)$  and associated weights given by  $w_i$  and  $\omega_j$ . In the angular direction we used Gauß-Legendre points distributed symmetrically about  $\pi$  on a full azimuthal interval of  $[0, 2\pi]$  to take advantage of cancellations stemming from the differences of derivatives at interval boundaries.

The radial integrals posed two challenges, at  $k' = k_o$  and  $k' \rightarrow \infty$ . Aside from the singularities, the local potentials we studied depend on the differences  $k_x - k'_x$  and  $k_y - k'_y$ , requiring that these integrals be carried out to large values of  $k'$ . To regularize the poles we employed two different methods and confirmed that their results agree.

For the scattering problem  $k_o$  is real and we were able to remove the poles through a standard subtraction technique [44, 45]. Applying the identity

$$\lim_{\epsilon \rightarrow 0} \int_0^{\infty} \frac{f(k')}{k_o^2 - k'^2 + i\epsilon} dk' = \int_0^{\infty} \frac{f(k') - f(k_o)}{k_o^2 - k'^2} dk' - \frac{i\pi}{2k_o} f(k_o) \quad (4.1)$$

to (3.22) produces the equation

$$\begin{aligned} V(k, \theta; k_o, \theta_o) &= T(k, \theta; k_o, \theta_o) \\ &- \frac{2\mu}{\hbar^2} \sum_{j=1}^m \omega_j \sum_{i=1}^n w_i \frac{V(k, \theta; k'_i, \theta'_j) T(k'_i, \theta'_j; k_o, \theta_o) k'}{k_o^2 - k_i'^2} \\ &+ \frac{2\mu}{\hbar^2} \sum_{j=1}^m \omega_j V(k, \theta; k_o, \theta_j) T(k_o, \theta_j; k_o, \theta_o) k_o \sum_{i=1}^n \frac{w_i}{k_o^2 - k_i'^2} \\ &+ i\pi \frac{\mu}{\hbar^2} \sum_{j=1}^m \omega_j V(k, \theta; k_o, \theta_j) T(k_o, \theta_j; k_o, \theta_o), \end{aligned} \quad (4.2)$$

used to solve for the matrix elements of  $T$ . Because the subtraction technique redistributes the information held at a singularity across the entire real line, the radial integration may be sensitive to truncation, dictating our use of appropriately scaled Gauß-Legendre points in the radial direction as well. Systems of equations were constructed by allowing  $(k, \theta)$  to take on the values of each of the mesh points in addition to the on-shell momenta  $(k_o, \theta_j)$ . Observing the restriction  $k' \neq k_o$ , these resulting systems of up to  $N = 7500$  (which represents the upper limit for a gigabyte of physical memory) double-precision complex equations were then solved simultaneously using the well optimized, 'canned' LAPACK subroutine ZGESV and its subroutines provided in the netlib repository ([www.netlib.org](http://www.netlib.org)). Subsequently, the wave functions, (3.24), were then calculated by matrix multiplication.

We tested our coding for the  $T$ -matrix calculation on an azimuthally symmetric potential which could include both attractive and repulsive regions by the choice of two parameters,  $V_a$  and  $V_b$ ,

$$V(r) = \frac{[V_a r^2 - V_b]}{\exp(r^2)}. \quad (4.3)$$

Resulting cross sections from our code were compared with those obtained from the partial wave shifts of the angular momentum eigenfunctions. Agreement was established in all cases. A couple of typical results are shown in figure 4.1 while the corresponding phase shifts and the particulars of their computation are left for appendix D. As in the rest of this paper, results are displayed for the elastic channel only with the following choice for energy units:

$$2\mu = \hbar^2 \quad \Rightarrow \quad E = k_o^2. \quad (4.4)$$

Resonances and their widths have been discussed in section 3.1 as solutions of (3.12) where the energy,  $E$ , of the system is analytically continued to the fourth quadrant of the second Riemann sheet of the complex plane. Because on-shell terms are no longer needed and the Green's function is nonsingular for complex energies, the radial integration may be truncated where contributions from the integrand are no longer significant. Near  $E$ , however, the integrand will vary rapidly as the complex energy approaches the real axis (see figure 4.2). To treat this region we exploit the fact that the numerator of the integrand is still smooth and apply a Taylor-Laurent series expansion,

$$\begin{aligned} \int_{E_1}^{E_2} \frac{f(E')}{E - E'} dE' &= \int_{E_1}^{E - \varepsilon_1} \frac{f(E')}{E - E'} dE' + \int_{E + \varepsilon_2}^{E_2} \frac{f(E')}{E - E'} dE' \\ &+ \int_{E - \varepsilon_1}^{E + \varepsilon_2} \frac{1}{E - E'} \left[ f(E) + (E' - E)f'(E) + \frac{(E' - E)^2}{2} f''(E) + O(E' - E)^3 \right] dE', \end{aligned} \quad (4.5)$$

(here  $\mu dE' = \hbar^2 k' dk'$ ) for which now

$$E = (k_{or}^2 - k_{oi}^2, 2k_{or}k_{oi}) \in \mathcal{Z}, \quad (4.6)$$

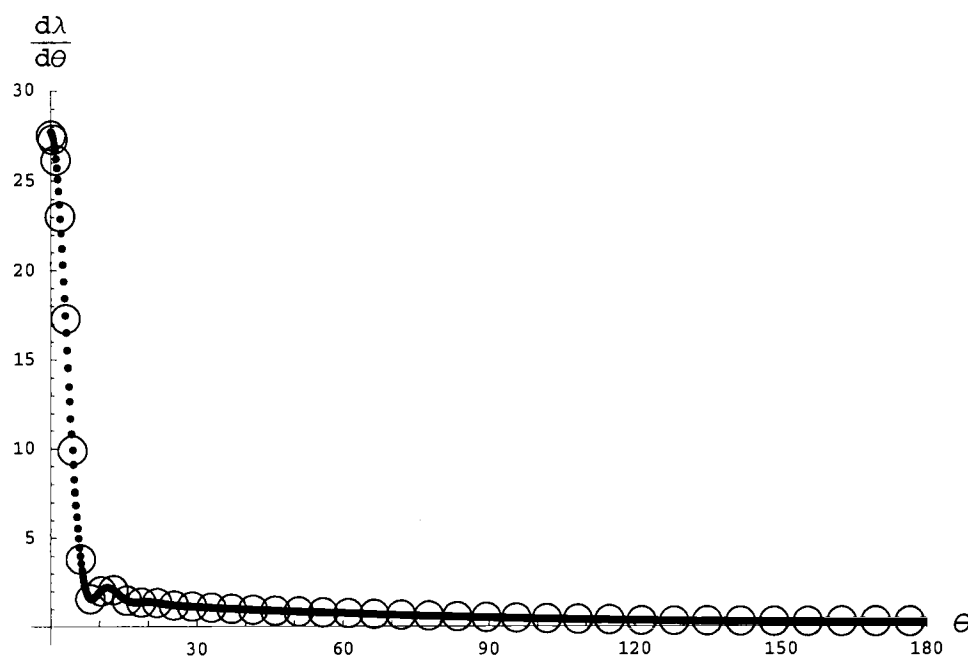
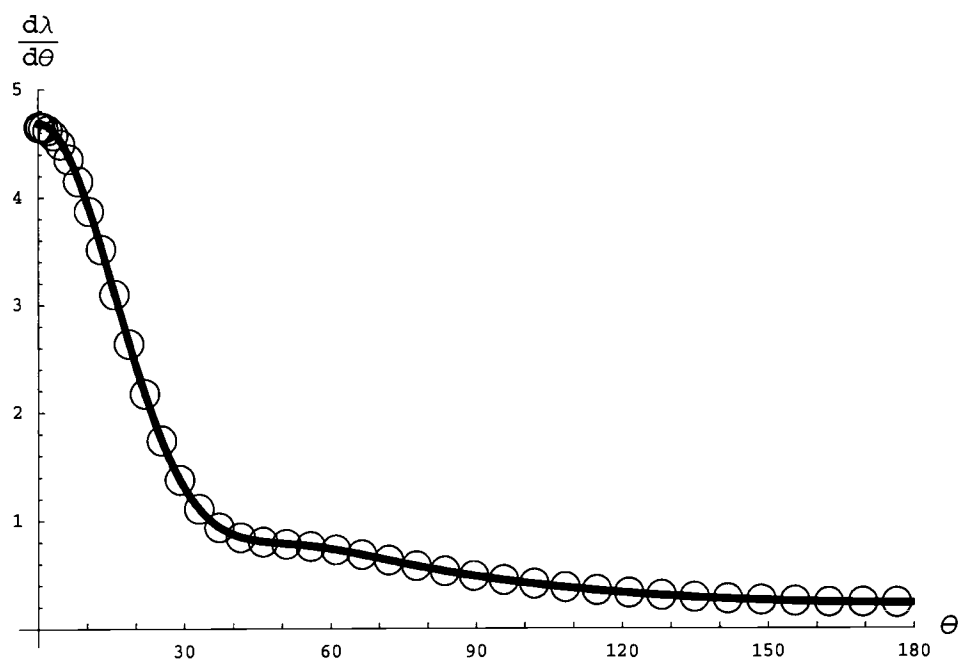


Figure 4.1: Verification of differential cross section output (open circles) by comparison against a partial wave analysis (filled dots) for the central test potential (4.3) where  $V_a=0$ ,  $E_o/V_{\max} = e^2/(4\pi)$ , and  $V_b=-16$  (top)  $V_b=-256$  (bottom).

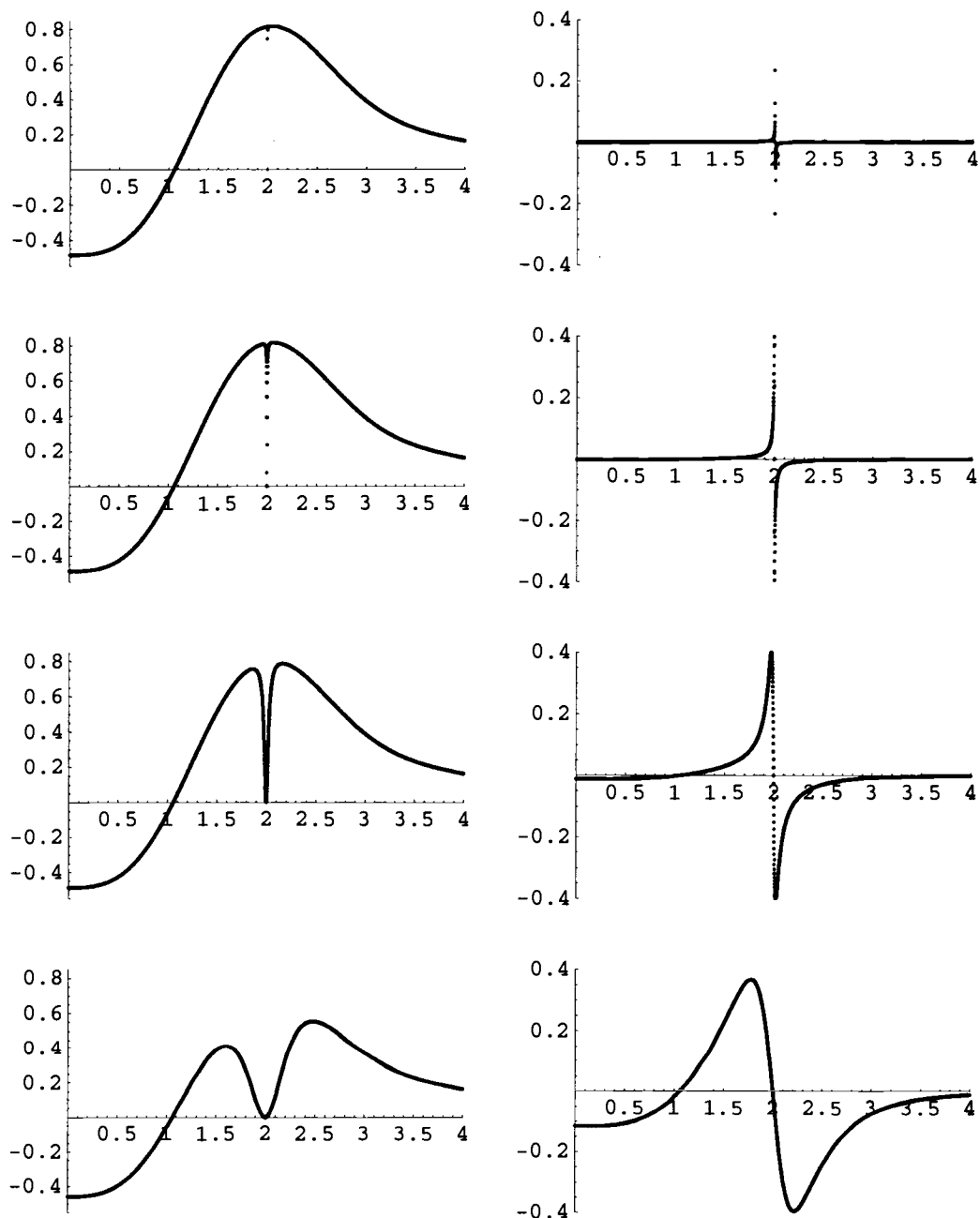


Figure 4.2: First Born approximations ( $VG^+V$ ) to the corrected radial integrands with the subtraction given by (4.1) after they have been analytically continued to complex energies of (from top to bottom row)  $E = \{(4.0, .001), (4.0, .01), (4.0, .1), (4.0, 1.0)\}$ , as a function of  $k'$ . Here  $k_x = .75$ ,  $k_y = .75$  and  $\theta = \pi/4$ . Real (left) and imaginary (right) parts plotted. Note how the undulation widens as the energy moves away from the real axis.

giving this expansion both a real and imaginary part. Uniform radial intervals in  $k$ -space of width  $\sqrt{\varepsilon_2} - \sqrt{\varepsilon_1}$  were used which allow for the determination of  $f(E)$  in (4.5), along with its first and second derivatives, through the simultaneous solution of the following three approximations:

$$\begin{aligned} f(E_{p-1}) &\approx f(E) + (E_{p-1} - E) f'(E) + \frac{(E_{p-1} - E)^2}{2} f''(E) \\ f(E_p) &\approx f(E) + (E_p - E) f'(E) + \frac{(E_p - E)^2}{2} f''(E) \\ f(E_{p+1}) &\approx f(E) + (E_{p+1} - E) f'(E) + \frac{(E_{p+1} - E)^2}{2} f''(E). \end{aligned} \quad (4.7)$$

The resulting three complex integrals represented by the last term of (4.5) are easily evaluated and we then proceed to assemble the inverse wave operator  $\Omega_E^{-1}$ . It would be possible to use an expansion of higher order, but nothing would be gained since a trapezoidal rule is used for the remainder of the radial integration for which the error is proportional to  $(\Delta k)^2$ .

The discretized characteristic equation (3.12) must have  $N$  roots. Most of these solutions will not be resonances but rather artifacts of the discretization. These artificial roots are expected to lie near the real axis between the discrete grid points. They are related to the approximate representation of the potential as the sum of delta functions along the real axis. Actual resonances may be recognized from their independence of the numerical implementation and from widths that decrease with increasing potential heights.

To confirm our resonances, we required verification from a second code that was written using the alternate identity (4.1) for regularization. For this code the on-shell momenta were retained and an irregular radial grid spacing of Gauß-Legendre points on  $[0, \infty)$ , as required by the subtraction method, replaced the truncated radial points of uniform spacing from the code discussed above. Both codes were specifically designed to find the zeros of a system of  $n$  nonlinear functions in  $n$  variables through the use of a modified Powell hybrid method. In our case  $n = 2$ , where the real and imaginary parts of the determinant (3.12) are functions of the real and imaginary parts of the analytically continued energy,  $E$ .

We did not seek to find all the resonances in the complex plane. Because we lacked any prior knowledge of resonance positions for the unfamiliar systems investigated, we would ideally initialize independent searches on the vertices of a hypothetical grid placed over the complex energy plane. If the grid were tight enough, we would expect that the result would be overlapping neighborhoods of searched areas for which we would have exhausted the possible dwellings of any elusive poles. In reality, however, we lacked the resources for such an extensive search, so we had to settle for an alternate plan. This was to look for signatures of long-lived resonances in the cross sections and

initialize searches only in their immediate neighborhoods.

## Chapter 5

# 3-center scattering potential

The first potential chosen was the soft hyperbolically defocusing scatterer plotted in figure 5.1. It

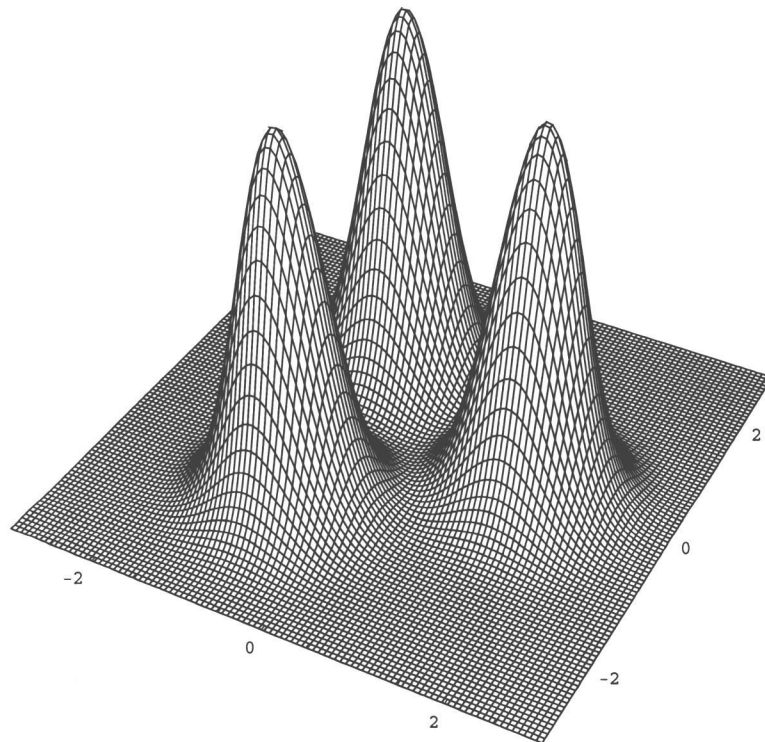


Figure 5.1: Three center scatterer.

has a three-fold symmetry defined by three overlapping Gaussian peaks, each of height  $V_0$  and width

$1/a$ , lying on the vertices of an equilateral triangle with sides of length  $R$ ,

$$V(\mathbf{r}) = \frac{V_o}{\exp\left(\left[a\left(x - \frac{R}{\sqrt{3}}\right)\right]^2 + [ay]^2\right)} + \frac{V_o}{\exp\left(\left[a\left(x + \frac{R}{2\sqrt{3}}\right)\right]^2 + \left[a\left(y - \frac{R}{2}\right)\right]^2\right)} + \frac{V_o}{\exp\left(\left[a\left(x + \frac{R}{2\sqrt{3}}\right)\right]^2 + \left[a\left(y + \frac{R}{2}\right)\right]^2\right)}. \quad (5.1)$$

This spatial dependence allows low-energy quantum particles to be briefly trapped between the peaks within its central region. The degree of trapping of these resonant states may be determined from their widths and the probability densities. For a narrow resonance the trapping is more stable, and the magnitude of the wave function at the center of the potential is large relative to the incident plane wave, resembling a bound state. For this reason we expect the wave function within the scatterer's interior to exhibit symmetry properties reflecting those of the potential, described by the dihedral group  $D_3$ , characteristic of an equilateral triangle. The character table (5.1) for this specific group, which is covered in many texts on the topic [46], is given with the irreducible symmetry representations labeled by the appropriate Mulliken symbols which are the most commonly used symmetry labels. The  $A$  label is given to singly degenerate states which are symmetric with respect to rotation about the principal axis. Adding a subscript,  $A_1$  or  $A_2$ , indicates inversion symmetry or asymmetry respectively through the reflection planes ( $3\sigma_\nu = 1 \Rightarrow A_1$  or  $3\sigma_\nu = -1 \Rightarrow A_2$ ). The symbol  $E$  indicates a doubly degenerate state. The  $B$  label, which is first used in the following chapter, specifies a singly degenerate state which is antisymmetric with respect to rotation by  $\pm\pi/2$  about the principal axis which is normal to the plane. Visual renderings of the  $A_1$  and  $A_2$  irreducible symmetry

$C_{3\nu}$	$E$	$2C_3$	$3\sigma_\nu$
$A_1$	1	1	1
$A_2$	1	1	-1
$E$	2	-1	0

Table 5.1:  $D_3$  dihedral character table.

representations are provided in figure 5.2 for the purpose of comparisons with wave functions by visual inspection. The two-dimensional  $E$  representation is not representable by a simple pair of pictures for this symmetry group because its symmetry operators introduce a complex phase.

Use of the potential (5.1) provided a means of further validating results by reproducing a long lived resonance reported by Gaspard and Rice [26] for three hard discs. A peak-to-peak distance

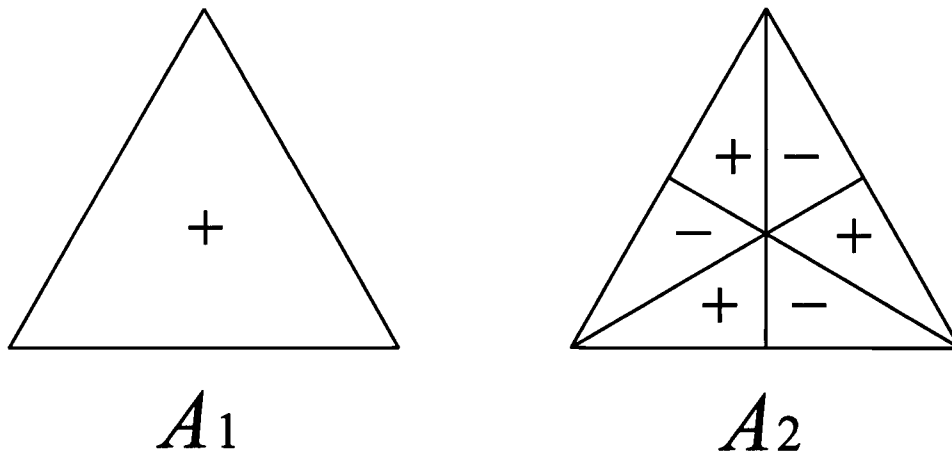


Figure 5.2:  $D_3$  irreducible abstract representations.

of  $R = 2.5$  was chosen for our potential to match the interdisc distance chosen in [26]. For a fixed potential height, the parameter  $a$  was adjusted to reproduce the resonance of Gaspard and Rice at  $k_o = 11.547$ . For this value of  $k_o$ , we could then examine how the phase shifts from a single peak of the soft potential compared to those of a hard disc with unit radius. For increasing potential heights of up to  $V_o = 4000$  (notice that  $V_{\max} > V_o$  with near equality for large values of  $a$  for which the peaks of (5.1) are narrow and overlap is minimized) we were able to show that the phase shifts for the soft Gaussian peaks approached those of the hard disc by tracking the differences of the pairs of phase shifts for angular momentum quantum numbers  $m$  from 0 to 7. In figure 5.3 we plot the natural log of the differences of the first and seventh phase shifts, for the hard and soft potential, against the natural log of the potential height. For each value of the potential height in this figure, the width parameter is adjusted so that the zeroth order phase shifts match. We see the last eight data points from each plot have an approximately linear relationship suggesting that convergence is proportional to a power of the potential height,

$$V^n \propto \Delta\delta(\text{hard} - \text{soft}) \equiv \delta_m(\text{hard}) - \delta_m(\text{soft}). \quad (5.2)$$

After carrying out the regression we find that  $n = -2.97 \times 10^{-6}$  for  $\Delta\delta_1$  and  $n = -3.74 \times 10^{-2}$  for  $\Delta\delta_7$ . This convergence is extremely slow, but nevertheless monotonic. The fact that  $|n_1| < |n_7|$  together with positive second derivatives in the plots of figure 5.3 suggest that this convergence will continue to slow as the potential height increases.

For most of the computations in this document we used the parameters  $V_o = 1200$  and  $a = 1.6$ , because computations become more difficult for increasing potential heights. A comparison of the

phase shifts for these values is shown in figure 5.4. This corresponds to the equipotential curve of a single Gaussian having a radius of 0.92644 at the energy of the resonance reported by Gaspard and Rice. For the full potential, built from three such Gaussian peaks, there will be slight overlap.

Given the momentum space representation of the  $D_3$  scatterer computed in appendix E,

$$\begin{aligned}
 V(\mathbf{k}, \mathbf{k}_o) = & \frac{V_o}{4\pi a^2 \exp\left[\frac{(k'_x - k_x)^2 + (k'_y - k_y)^2}{4a^2}\right]} \\
 & \times \left[ \left( \cos\left[\frac{(k'_x - k_x)R}{\sqrt{3}}\right] + 2 \cos\left[\frac{(k'_x - k_x)R}{2\sqrt{3}}\right] \cos\left[\frac{(k'_y - k_y)R}{2}\right] \right) \right. \\
 & \left. + i \left( \sin\left[\frac{(k'_x - k_x)R}{\sqrt{3}}\right] - 2 \sin\left[\frac{(k'_x - k_x)R}{2\sqrt{3}}\right] \cos\left[\frac{(k'_y - k_y)R}{2}\right] \right) \right], \quad (5.3)
 \end{aligned}$$

a plane wave incident on one of the lateral faces, for example  $\mathbf{k}_o = k_o \hat{\mathbf{x}}$ , produces the upper total cross section given in figure 5.5. We notice that the peak corresponding to the aforementioned Gaspard-Rice resonance is absent from this cross section. The reason is that this particular resonance carries an  $A_2$  symmetry representation. From figure 5.2 we note that this representation is asymmetric with respect to an axis parallel to a wavefront incident normally upon the lower face. We break the symmetry by directing the incident wave vector off axis by  $\pi/6$  radians. The resulting total cross sections are displayed in figure 5.5. The resonance peak is now clearly visible and tabulated in table 5.2 along with two additional long-lived resonances we marked for investigation. The probability

$V_o$	$E$	$\Gamma/2$	$k_r$	$k_i$	Order	Symmetry
1200	46.1718	$4.0252 \times 10^{-3}$	6.7950	$2.9617 \times 10^{-4}$	1	$A_1$
1200	69.9163	$1.0250 \times 10^0$	8.3618	$6.1292 \times 10^{-2}$	2	$E$
1200	133.264	$3.8954 \times 10^0$	11.545	$1.6870 \times 10^{-1}$	1	$A_2$

Table 5.2: First three 'long-lived' resonances with  $a=1.6$  and  $R=2.5$ .

densities for the resonances in table 5.2 are given in figures 5.6-5.8.

Due to the resolution of the plot, the effect on the total cross section of the lowest resonance in the table is difficult to see because of its narrow width. Its energy,  $E=46.1718$ , is just above that of the three saddle points,  $E=44$ , which connect the peaks and surround a central local minimum at  $E=18$ . Classically, a particle with the energy of this resonance is unbound, as it would be able to escape between the pillars by exiting over any of the saddle points. At energies just exceeding the height of the saddle points, the spacing between pillars is still small which leads to resonances with longer lives than those at higher energies. From figure 5.6 it is evident that the effective trapping of

this long-lived resonance inside the cage generates a probability density much larger than the incident wave, which is hardly visible by comparison. Being the fundamental resonance, it is associated with the  $A_1$  symmetry representation of figure 5.2.

In figure 5.9 we show the probability peak of the fundamental resonance from 5.6 scaled to clearly show the leaking of probability from inside the cage out around the potential's exit pillar. Figure 5.10 shows the probability, scaled to the same ratio with respect to the incident wave, for a slightly higher energy for comparison. With a shortening of the wavelength, one might naively expect that transmission of the incident wave through the potential would be improved since the wave function would seem to fit between the pillars more easily. As figure 5.10 shows, however, this is not the case. As the energy moves off resonance, the transmission of the incident wave through the potential drops off drastically. This is in agreement with results reported by Peskin *et al.* [32] discussed in section 2.2.2.

The second resonance is not as narrow so the trapped particle density is not as large, figure 5.7. We can begin to see the details of the incident wave approaching from the upper left and the interference with the scattered portion. In the longitudinal direction there is now a full standing wave within the potential's interior. Here again the leaking of probability can be seen around the potential's exit pillar.

Calculations involving the third resonance carry with them the least accuracy since its energy is among the greatest of all the resonances considered. To estimate the accuracy we inspect the three regions void of probability density in figure 5.8, where the pillars of the potential are seated. The wave function is small in these regions because of interference between the incident and scattered waves and is not due to an imposed boundary condition. Because the energy is low compared to the height of the potential, we expect the wave function to essentially vanish near the centers of these regions. In figure 5.11 we plot the real part of the wave function which has been clipped so that values below a negative cutoff are black and those above a positive one appear white. From this format the  $A_2$  symmetry representation, which is displayed in figure 5.2, is readily recognizable. By tracking the breakup of the gray areas between cutoffs near zero, we may estimate the precision of our calculation. In this case our incident wave,  $e^{ik \cdot r}/2\pi$ , has an amplitude relative to the gray regions that put numerical accuracy at about 0.12 percent. When a comparison is made against the trapped portion of the wave function for the lowest order resonance, this estimate improves to roughly 0.003 percent.

At an energy of  $E = 45.0$ , slightly lower than the fundamental resonance, we see from the probability density, figure 5.12, that the transverse wavelength is such that ingress between the

potential's entrance pillars is not possible and a strong reflection peak builds in front of it. As the energy increases toward resonance, we see from figure 5.13 that particles, with wavelengths that are still seemingly too large, are able to squeeze through the narrow passage into the scatterer's interior region. This occurs at the expense of the longitudinal wavelength. Energy being conserved, the longitudinal wavenumber,  $k_l = \sqrt{E - k_t^2}$ , goes imaginary as the transverse wavelength shortens, allowing for passage. This *quantum pinching* effect is evident from the longitudinal curvature away from the  $z=0$  plane and simultaneous transverse narrowing which can be seen from the wave function between the entrance pillars given by figures 5.14 and 5.15. Figure 5.16 shows quantum pinching again for a lower potential height,  $E=100$ , and the same value for the width parameter,  $a=1.6$ .

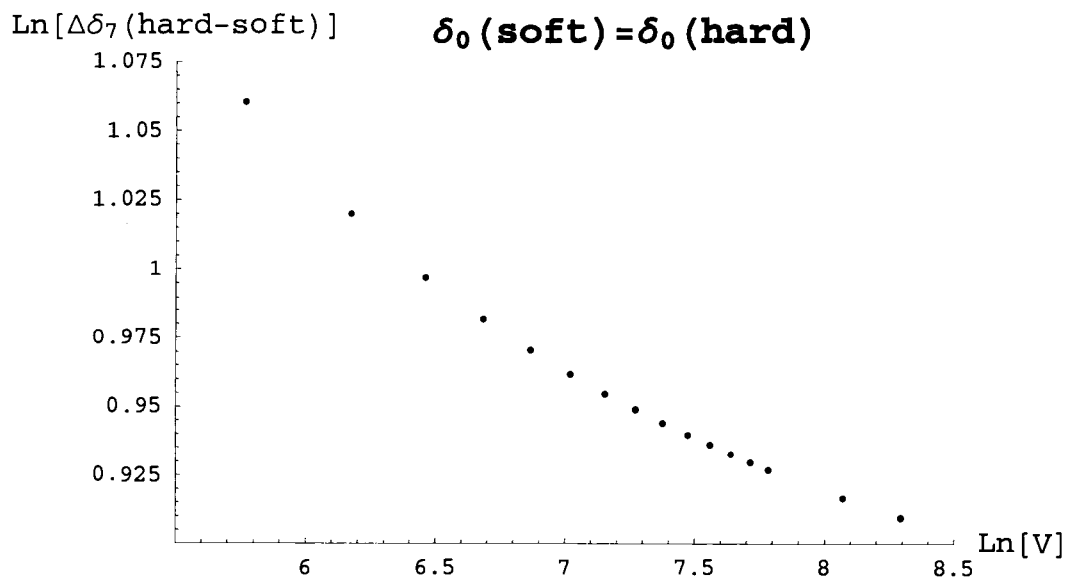
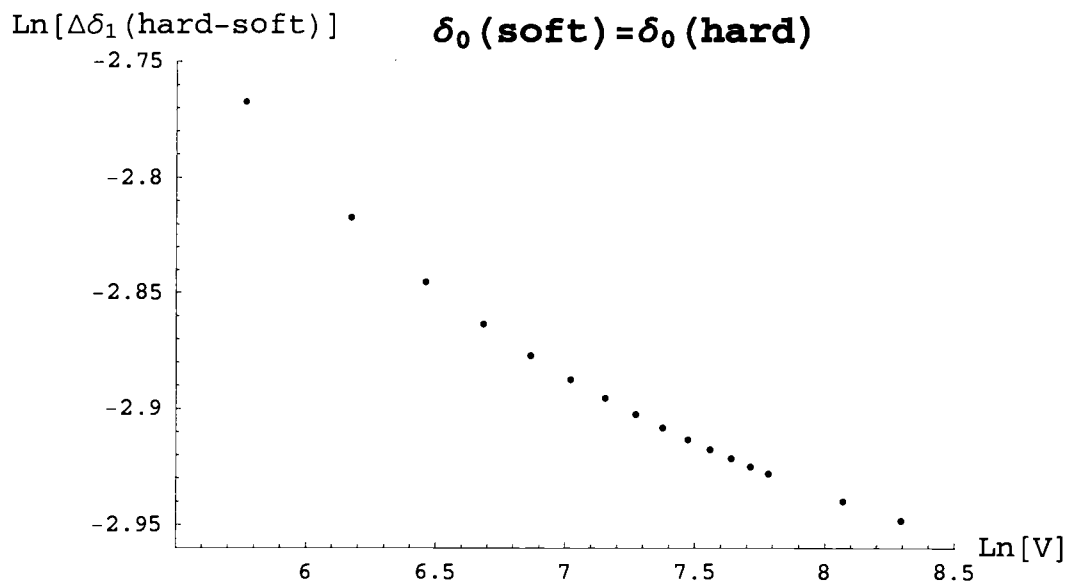


Figure 5.3: Difference of first (top) and seventh (bottom) phase shifts for soft and hard potentials with  $\delta_0$  matched. From fits of the last eight data points,  $\Delta\delta(\text{hard-soft}) \propto V^n$  where  $n = -2.97 \times 10^{-6}$  (top) and  $n = -3.74 \times 10^{-2}$  (bottom).

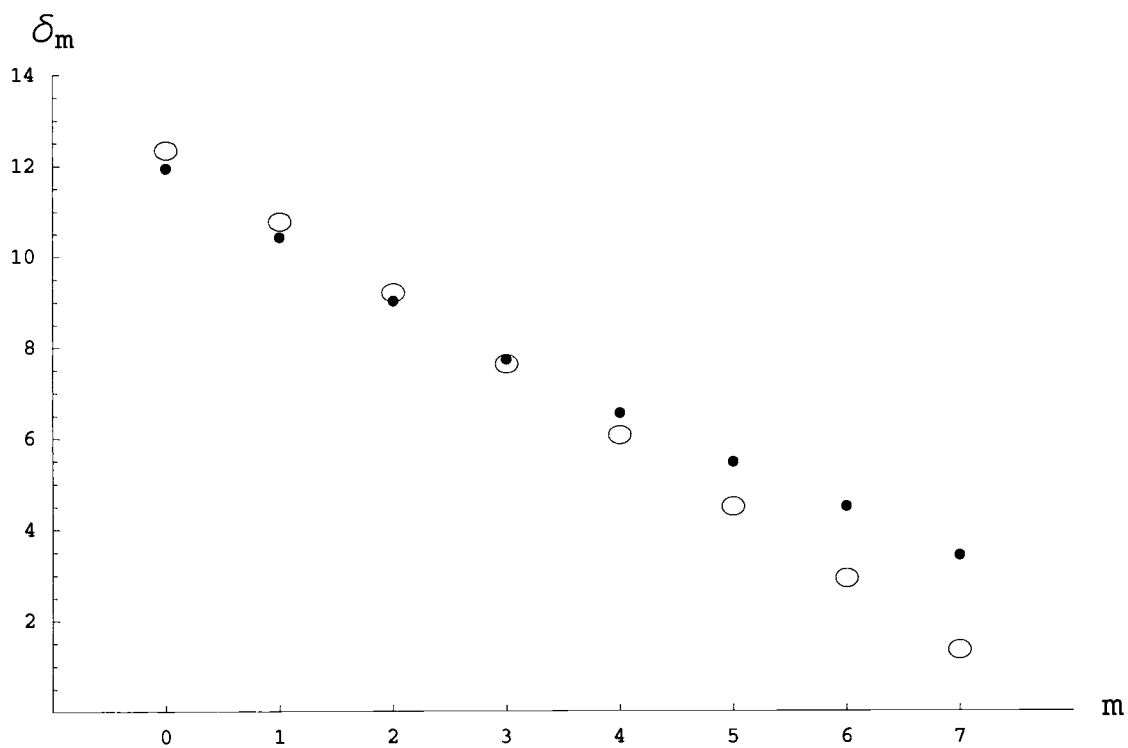


Figure 5.4: Partial wave phase shifts for a central hard disc of unitary radius (open circles) and one centralized exponential peak from (5.1) with  $V_0=1200$  and  $a=1.6$  (dots).

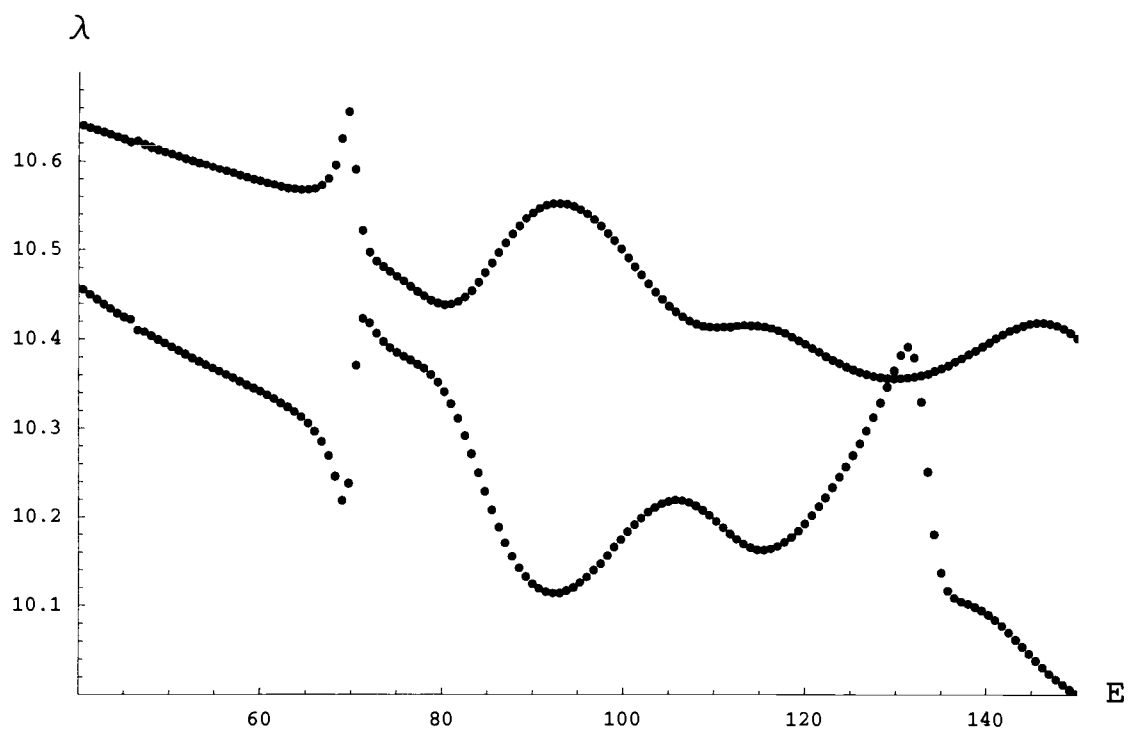


Figure 5.5: Total differential cross section on-axis (upper) and 30° off-axis (lower) for (5.1) with  $V_0=1200$ ,  $a=1.6$  and  $R=2.5$ .

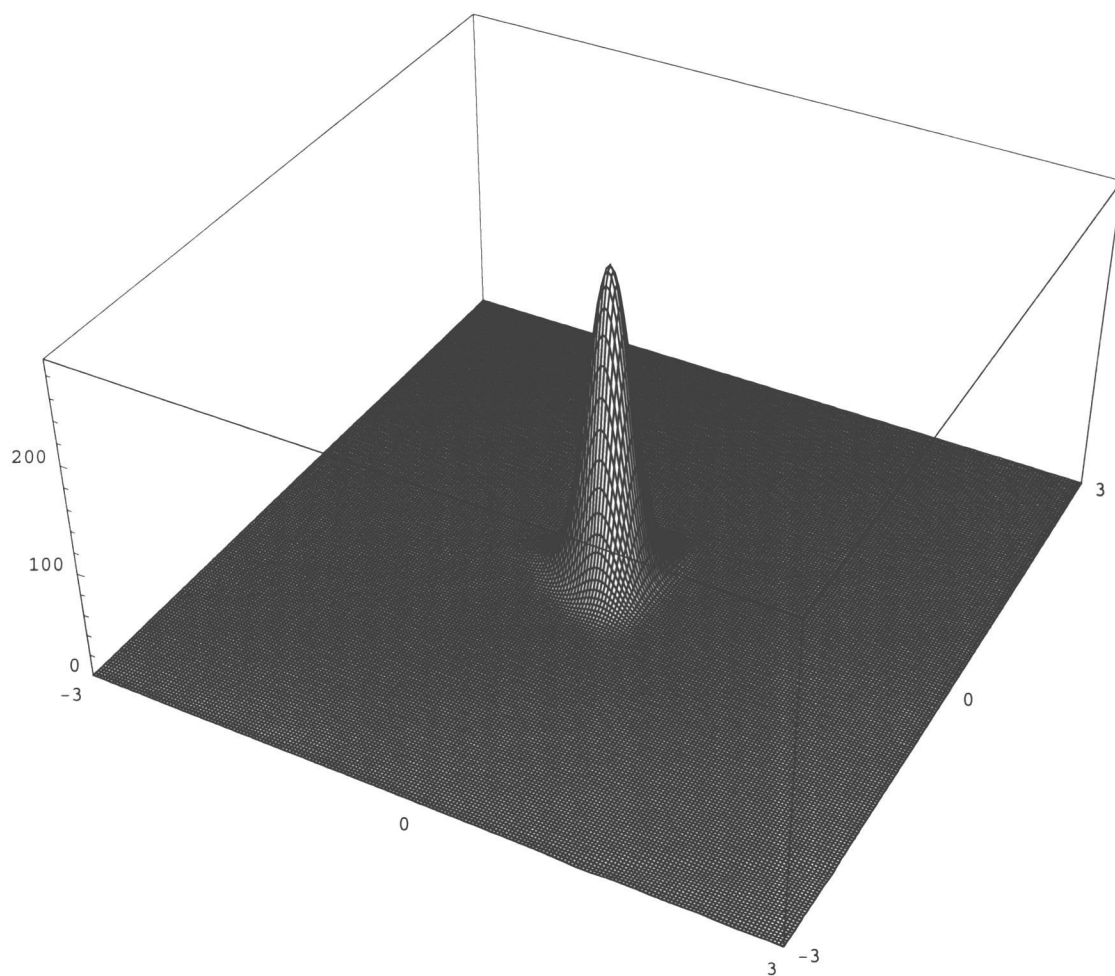


Figure 5.6: Probability density for the first resonance of table 5.2 for which  $V_o = 1200$ ,  $a = 1.6$  and  $E = 46.1718$  with normal incidence.

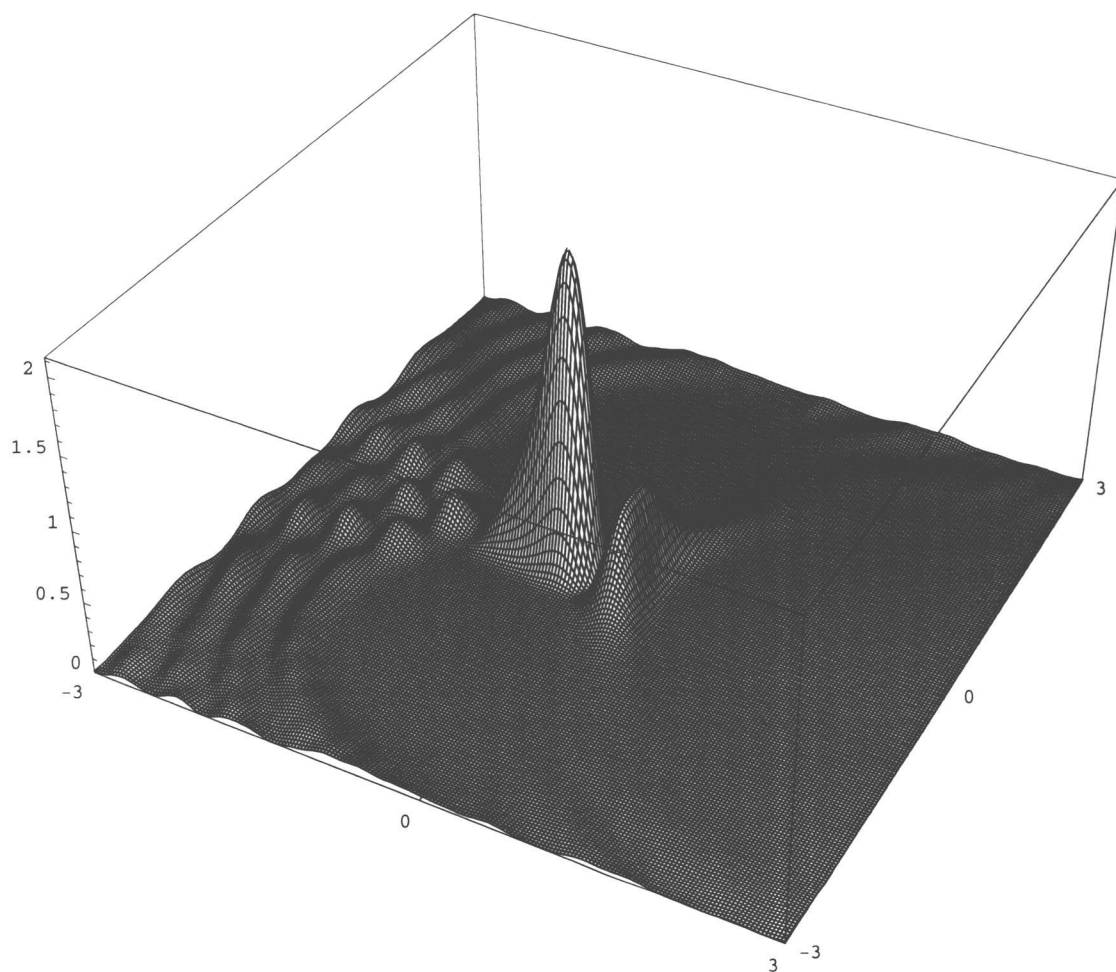


Figure 5.7: Probability density for the second resonance of table 5.2 for which  $V_0=1200$ ,  $a=1.6$  and  $E=69.9163$  with normal incidence.

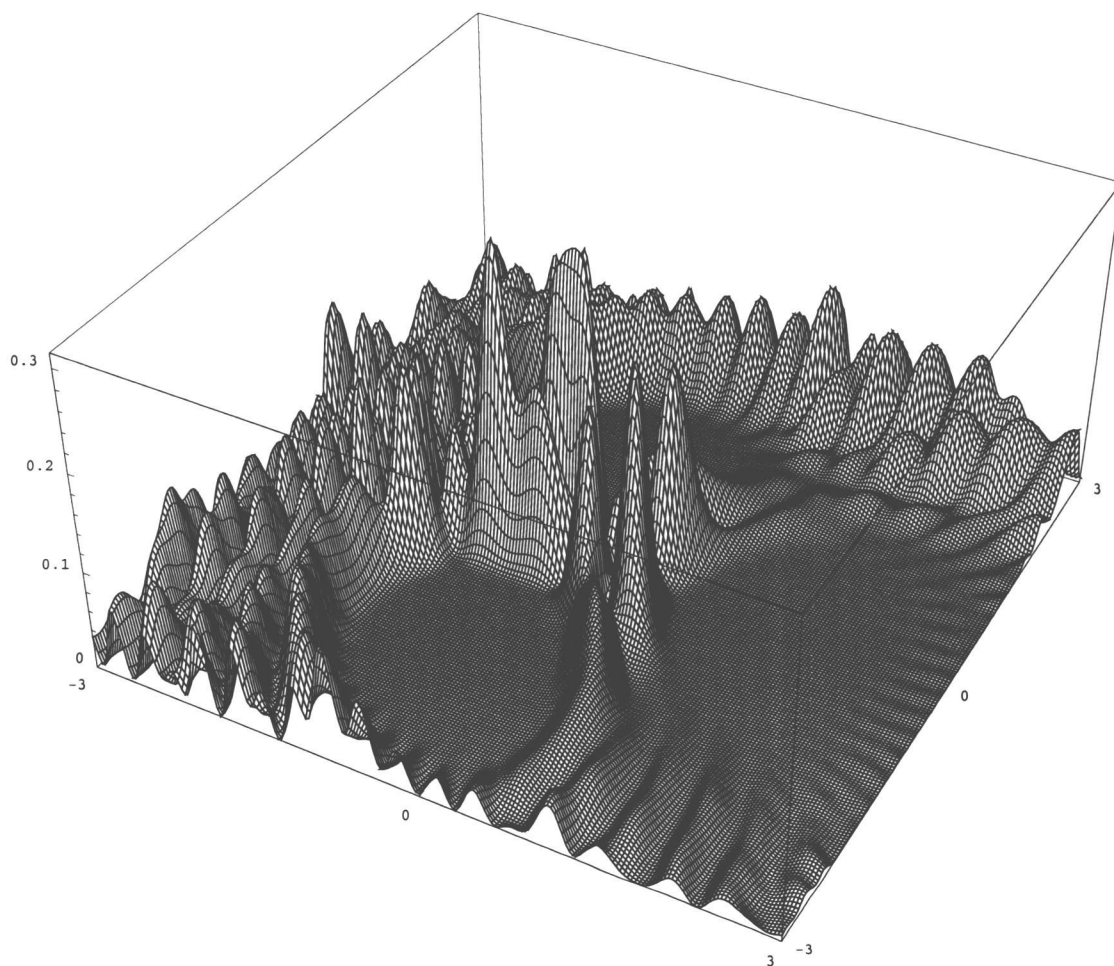


Figure 5.8: Probability density for the third resonance of table 5.2 for which  $V_o = 1200$ ,  $a = 1.6$  and  $E = 133.5$ . Here the incident angle is  $\theta_o = \pi/12$ .

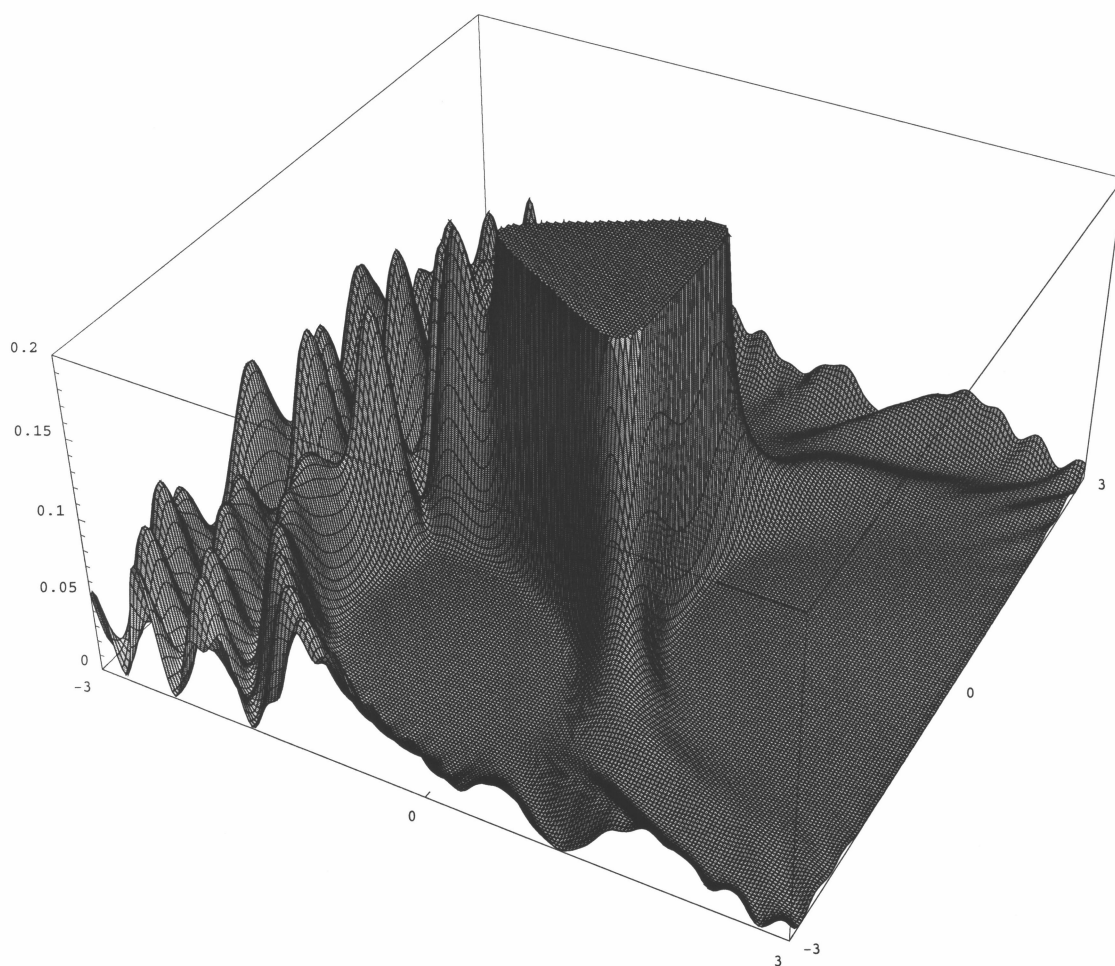


Figure 5.9: Clipped probability density for the first resonance of table 5.2 for which  $V_0 = 1200$ ,  $a = 1.6$  and  $E = 46.1718$  with normal incidence. Note how the particle flux is able to move through the potential.

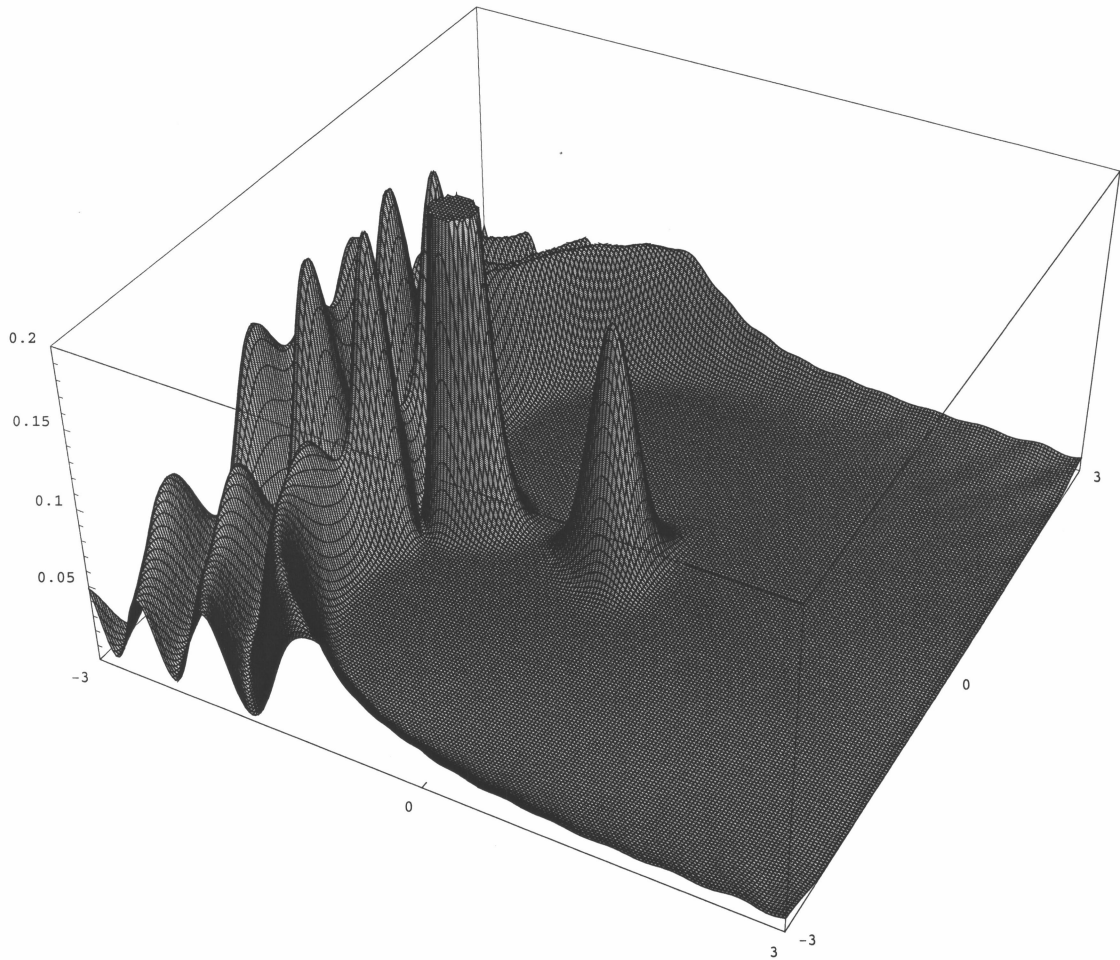


Figure 5.10: Clipped probability density just above,  $E = 46.3500$ , the fundamental resonance,  $E = 46.1718$ , for  $V_0 = 1200$  with a normal angle of incidence. Note that the particle flux exiting the potential's interior region is greatly reduced as compared to that at resonance given by figure 5.9.

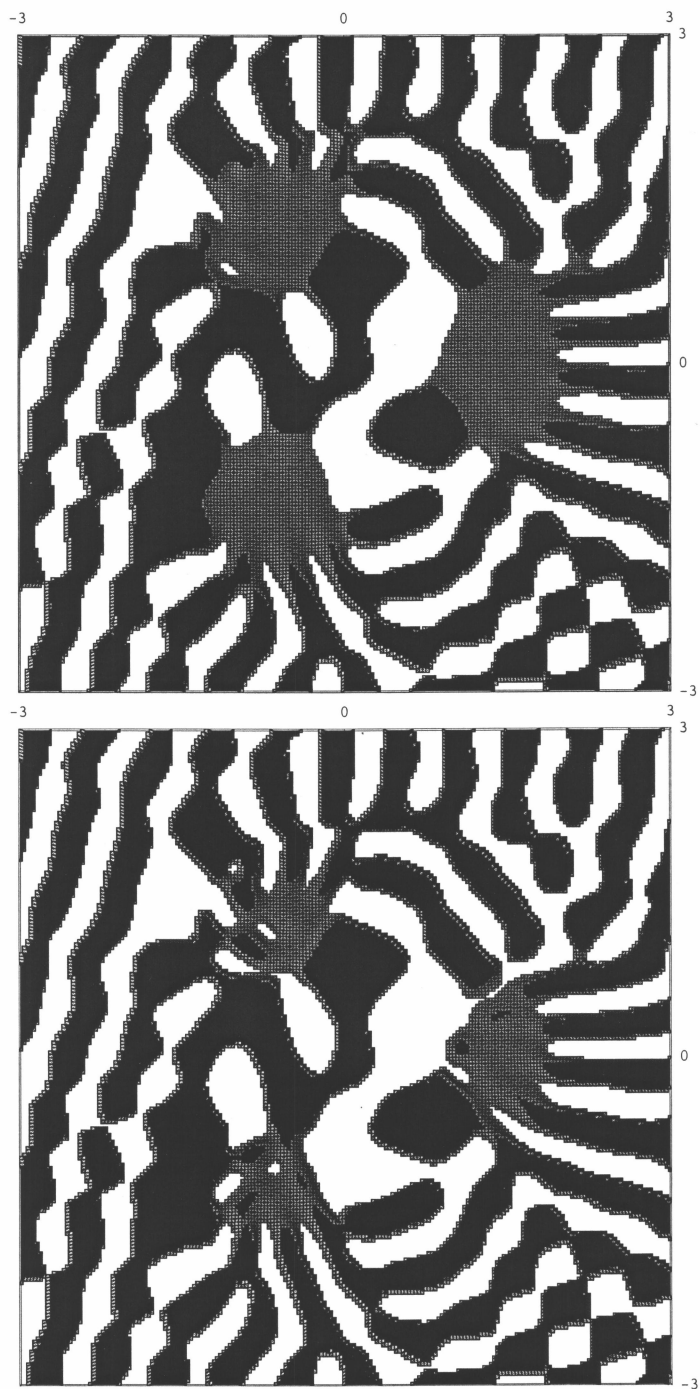


Figure 5.11: Real part of the third resonance's clipped wave function. Black  $< -0.001 < \text{Gray} < 0.001 < \text{White}$  (top). Black  $< -0.0002 < \text{Gray} < 0.0002 < \text{White}$  (bottom). The incident plane wave is seen to approach from the left at a  $15^\circ$  downward angle.

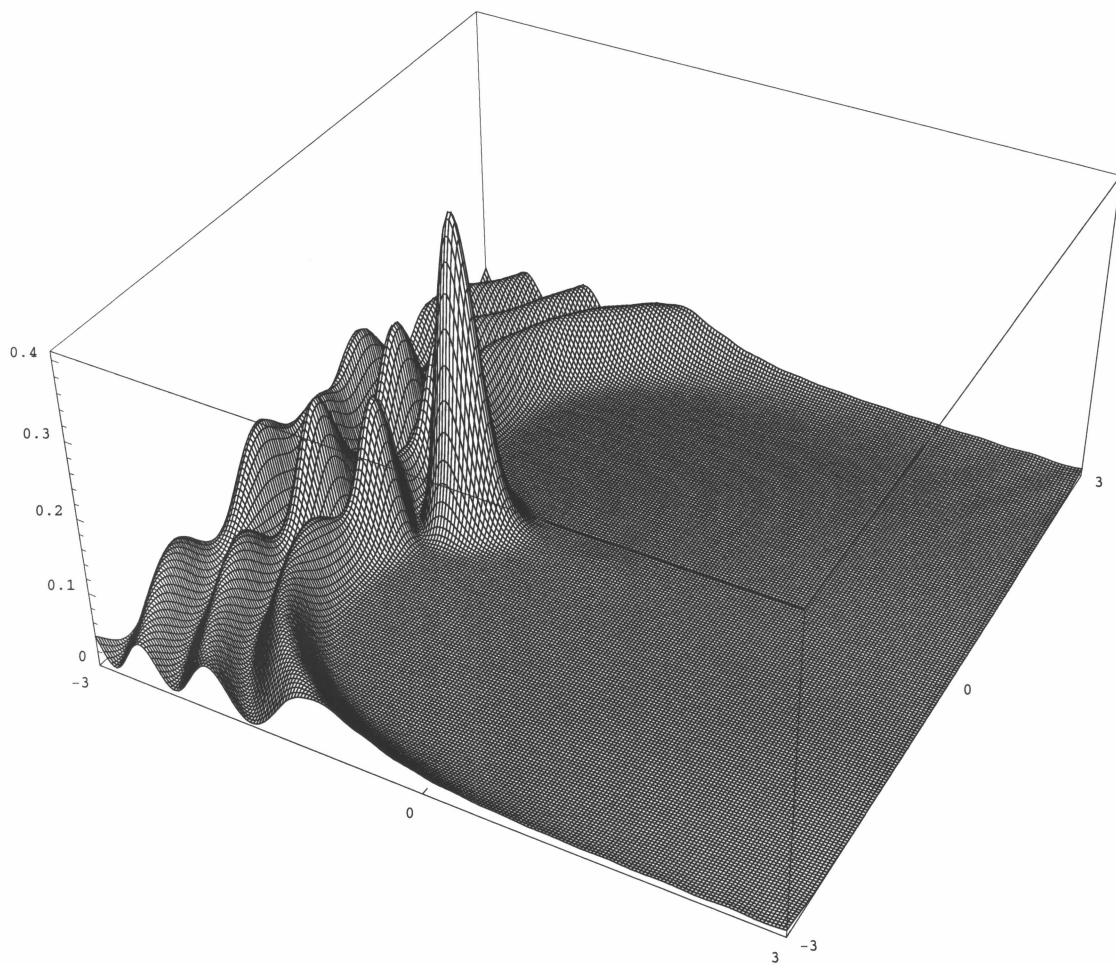


Figure 5.12: Probability density below,  $E = 45.0$ , the fundamental resonance,  $E = 46.1718$ , for  $V_0 = 1200$  with a normal angle of incidence. Note that the particle flux is unable to penetrate into the potential's interior region.

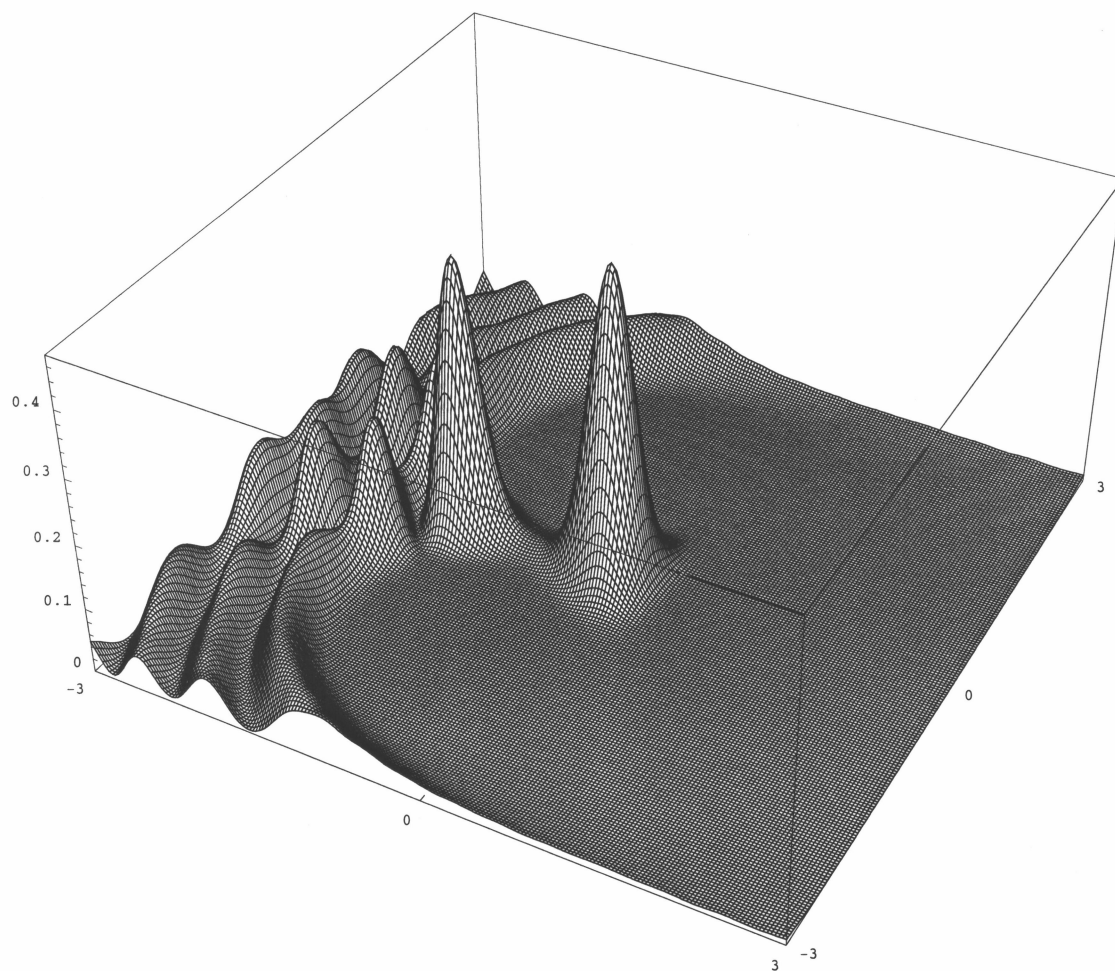


Figure 5.13: Probability density below,  $E=46.0725$ , the fundamental resonance,  $E=46.1718$ , for  $V_0 = 1200$  with a normal angle of incidence. At this energy the particle flux is first able to squeeze into the potential's interior region.

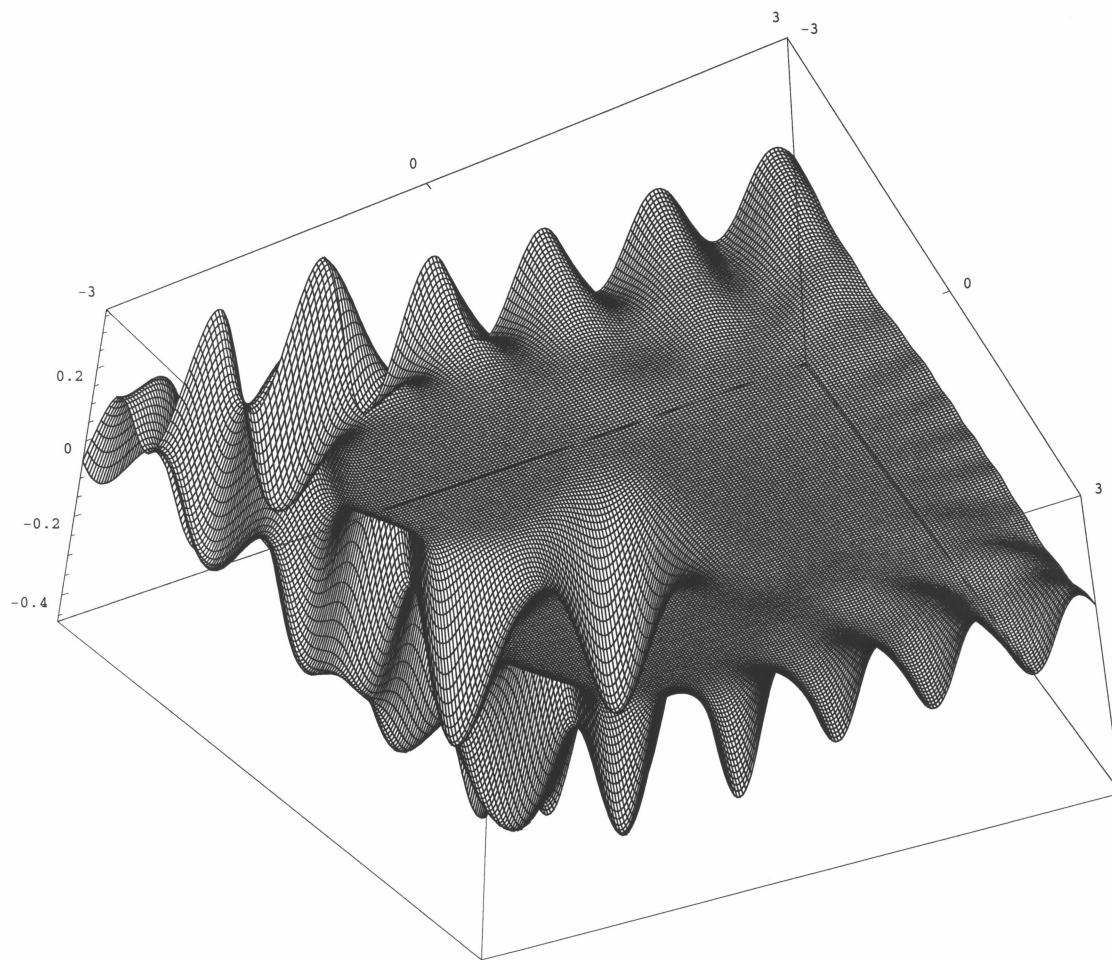


Figure 5.14: Real part of wave function below,  $E = 46.0725$ , the fundamental resonance of  $E = 46.1718$  for  $V_0 = 1200$  with a normal angle of incidence showing quantum pinching (viewed from underneath).

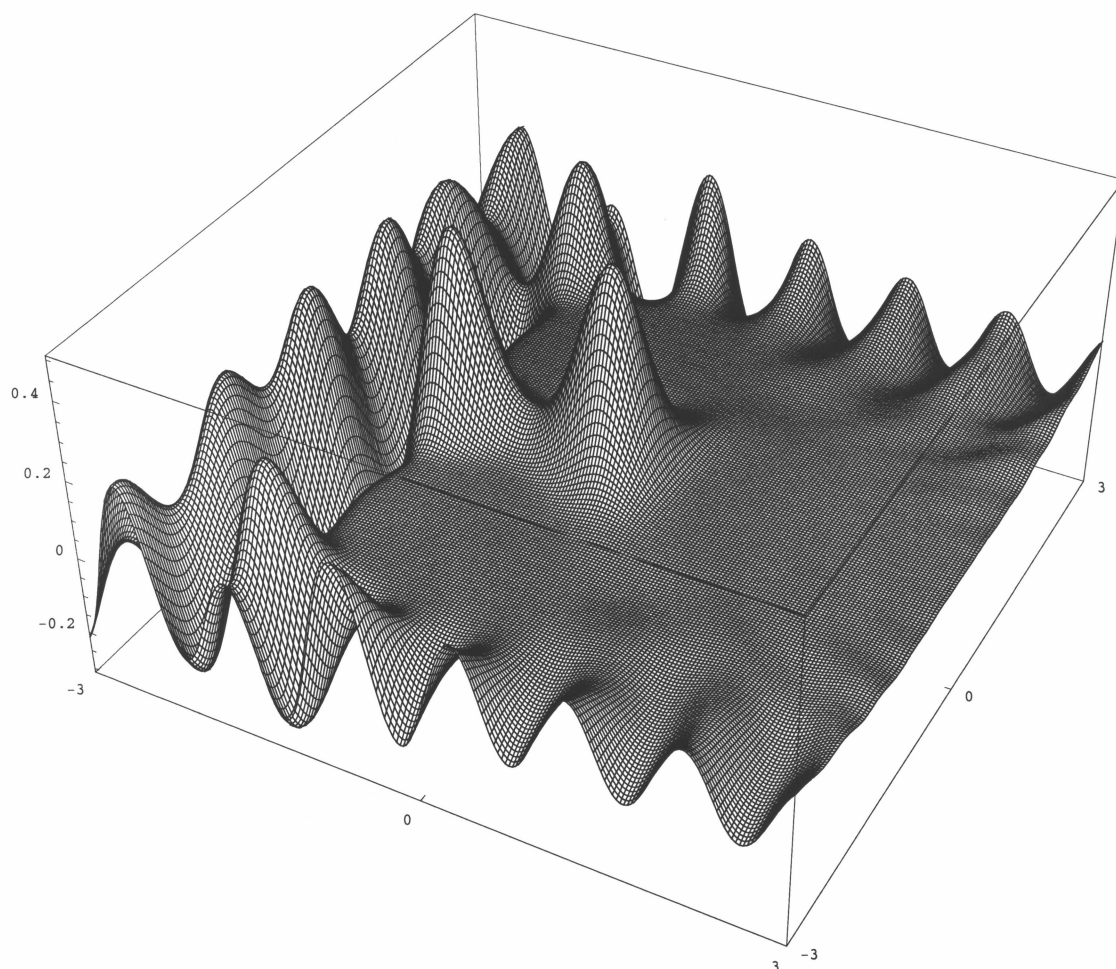


Figure 5.15: Imaginary part of wave function below,  $E=46.0725$ , the fundamental resonance of  $E=46.1718$  for  $V_0=1200$  with a normal angle of incidence showing quantum pinching.

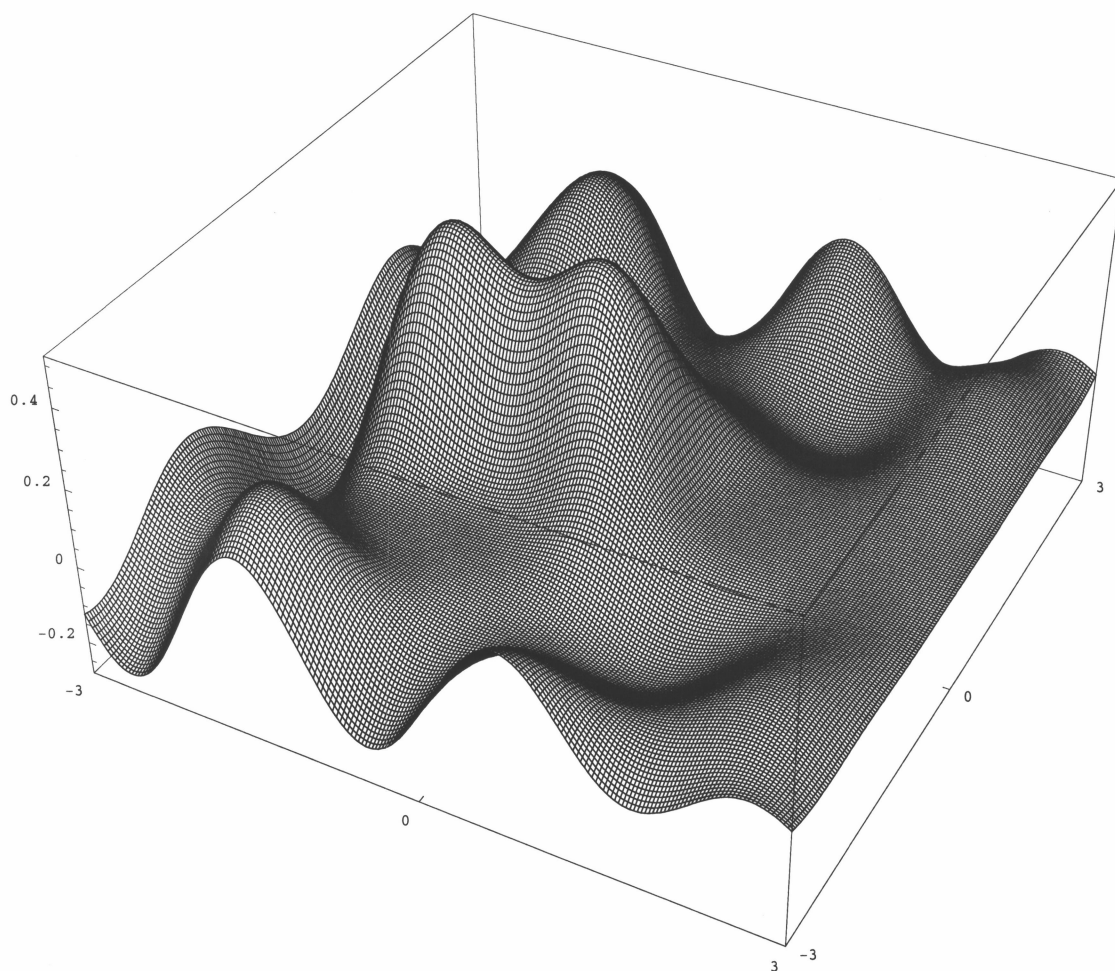


Figure 5.16: Imaginary part of wave function below,  $E = 9.56$ , the fundamental resonance of  $E = 9.8326$  for  $V_0 = 100$  with a normal angle of incidence showing quantum pinching.

## Chapter 6

# 4-center scattering potential

The second potential is quad-peaked with scattering centers placed on the vertices of a square with sides  $R$ ,

$$\begin{aligned}
 V(\mathbf{r}) = & \frac{V_o}{\exp\left(\left[a\left(x-\frac{R}{2}\right)\right]^2 + \left[a\left(y+\frac{R}{2}\right)\right]^2\right)} + \frac{V_o}{\exp\left(\left[a\left(x+\frac{R}{2}\right)\right]^2 + \left[a\left(y-\frac{R}{2}\right)\right]^2\right)} \\
 & + \frac{V_o}{\exp\left(\left[a\left(x+\frac{R}{2}\right)\right]^2 + \left[a\left(y+\frac{R}{2}\right)\right]^2\right)} + \frac{V_o}{\exp\left(\left[a\left(x-\frac{R}{2}\right)\right]^2 + \left[a\left(y-\frac{R}{2}\right)\right]^2\right)}. \quad (6.1)
 \end{aligned}$$

The parameter controlling the slope of the peaks is again set to the same value,  $a = 1.6$ , which produces a partial wave phase shift pattern similar to that of a hard disc for  $V_o = 1200$  (see figure 4.1). For uniformity, a bulky repeller,  $R = 2.5$ , was again chosen giving a basis of comparison with the results of the previous chapter. The resulting potential is displayed in figure 6.1. In figure 6.2 we again illustrate the abstract geometric representations of the irreducible symmetry groups given in the character table 6.1 for square symmetry.

$C_{4\nu}$	$E$	$2C_4$	$C_2$	$2\sigma_\nu$	$2\sigma_d$
$A_1$	1	1	1	1	1
$A_2$	1	1	1	-1	-1
$B_1$	1	-1	1	1	-1
$B_2$	1	-1	1	-1	1
$E$	2	0	-2	0	0

Table 6.1:  $D_4$  dihedral character table.

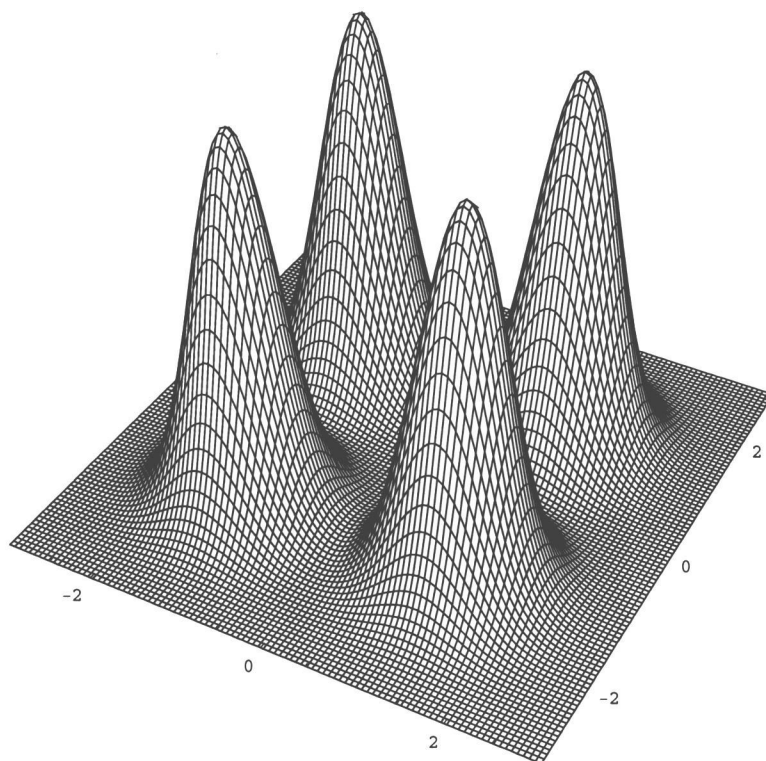
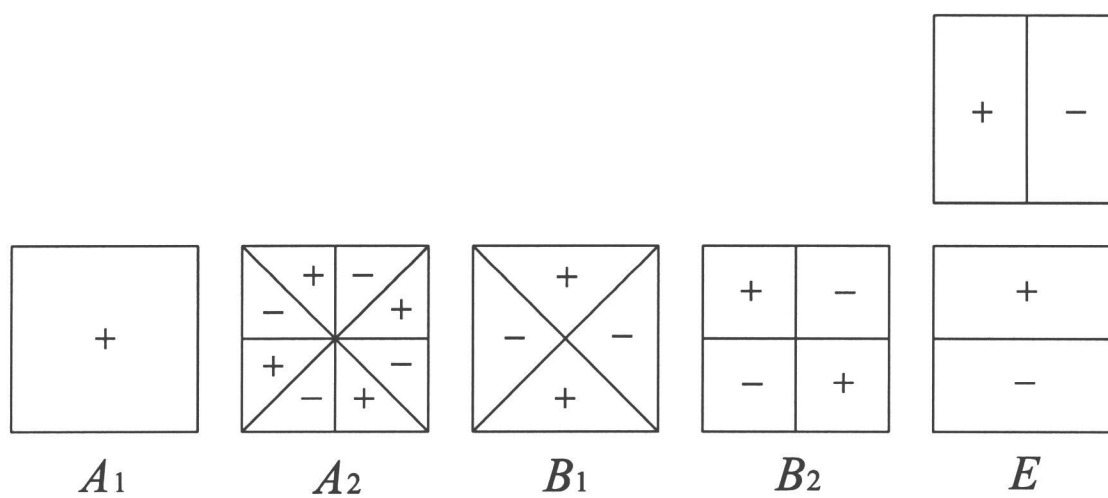


Figure 6.1: Four center scatterer.

Figure 6.2:  $D_4$  irreducible abstract representations.

After finding the potential's momentum-space representation,

$$V(\mathbf{k}, \mathbf{k}_o) = \frac{V_o}{\pi a^2} \left( \frac{\cos \left[ \frac{R}{2}(k_x - k'_x) \right] \cos \left[ \frac{R}{2}(k_y - k'_y) \right]}{\exp \left[ \frac{(k_x - k'_x)^2 + (k_y - k'_y)^2}{4a^2} \right]} \right), \quad (6.2)$$

as required for equations (3.18, 3.22, 4.2), the cross sections are calculated from the on-shell transition matrix elements. Notice that (6.2) is real while the momentum space representation of the  $D_3$  scatterer, given by (5.3), is complex. The higher degree of symmetry here results in the cancellation of all imaginary parts for real  $k$ . Given in figure 6.3 are the total cross sections for incident angles of 0 and  $\pi/12$  radians. For  $V_o = 1200$  and  $a = 1.6$  the saddle points that signal the separation of the potential's pillars again occur at  $E = 44$  (compare this with the energy of the third resonance appearing in table 6.2). The local minimum, however, now occurs at  $E = 2$  making the resulting potential well deeper than the tri-peaked potential introduced in chapter 5. From these cross sections the two lowest order resonances cannot be seen for this potential height because they correspond to classically bound states that fall within the well. The quantum particles will be able to tunnel out of this well, but their lifetimes are so great that the resonances are too narrow to see in figure 6.3. For this reason additional plots (6.4) are provided for a reduced potential height  $V_o = 100$  for which the saddle points, at an energy of  $E = 3.7$ , now fall below the two lowest resonances entered in table 6.2. Note that the differential cross section becomes angle independent for very low energy scattering, as expected.

Several resonances of higher energy are still reasonably long-lived and thus produce characteristic wave patterns that are of particular interest. These have also been tabulated in 6.2. Probability densities for these resonances are displayed in figures 6.5-6.16.

$V_0$	$E$	$\Gamma/2$	$k_r$	$k_i$	Order	Symmetry
100	5.51305	$8.0678 \times 10^{-3}$	2.3480	$1.7180 \times 10^{-3}$	1	$A_1$
100	11.3781	$2.5449 \times 10^{-1}$	3.3734	$3.7775 \times 10^{-2}$	2	$E$
1200	45.7994	$1.5048 \times 10^{-3}$	6.7675	$1.1118 \times 10^{-4}$	1	$B_1$
1200	50.9141	$5.6243 \times 10^{-3}$	7.1354	$3.9411 \times 10^{-4}$	1	$A_1$
1200	61.8927	$1.2089 \times 10^{-1}$	7.8672	$7.6834 \times 10^{-3}$	2	$E$
1200	74.0325	$4.1675 \times 10^0$	8.6076	$2.4208 \times 10^{-1}$	1	$A_1$
1200	78.8937	$5.4588 \times 10^{-1}$	8.8823	$3.0728 \times 10^{-2}$	2	$E$
1200	105.017	$8.3296 \times 10^{-3}$	10.248	$4.0641 \times 10^{-4}$	1	$B_2$
1200	109.108	$1.2639 \times 10^0$	10.447	$6.0501 \times 10^{-2}$	1	?
1200	114.780	$1.7712 \times 10^{-1}$	10.715	$8.2660 \times 10^{-3}$	2	$E$
1200	131.429	$1.1741 \times 10^0$	11.464	$5.1208 \times 10^{-2}$	1	$A_2$
1200	134.587	$1.1474 \times 10^0$	11.601	$4.9450 \times 10^{-2}$	2	$E$
1200	147.285	$1.0664 \times 10^0$	12.136	$4.3936 \times 10^{-2}$	1	$B_1$

Table 6.2: First thirteen 'long-lived' resonances with  $a=1.6$  and  $R=2.5$ .

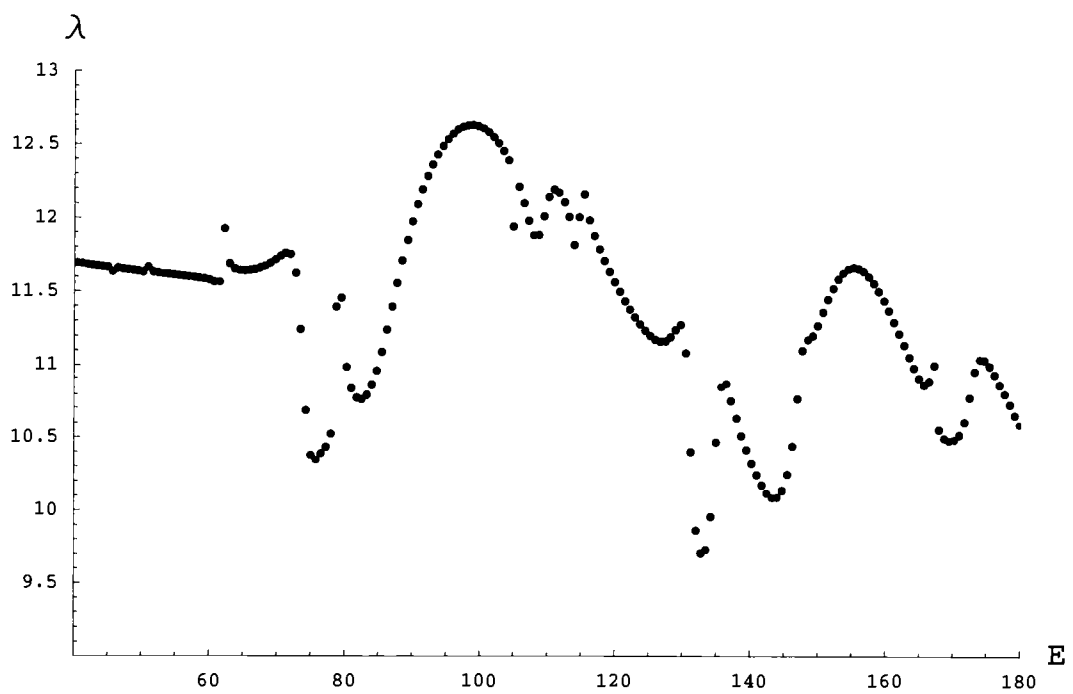
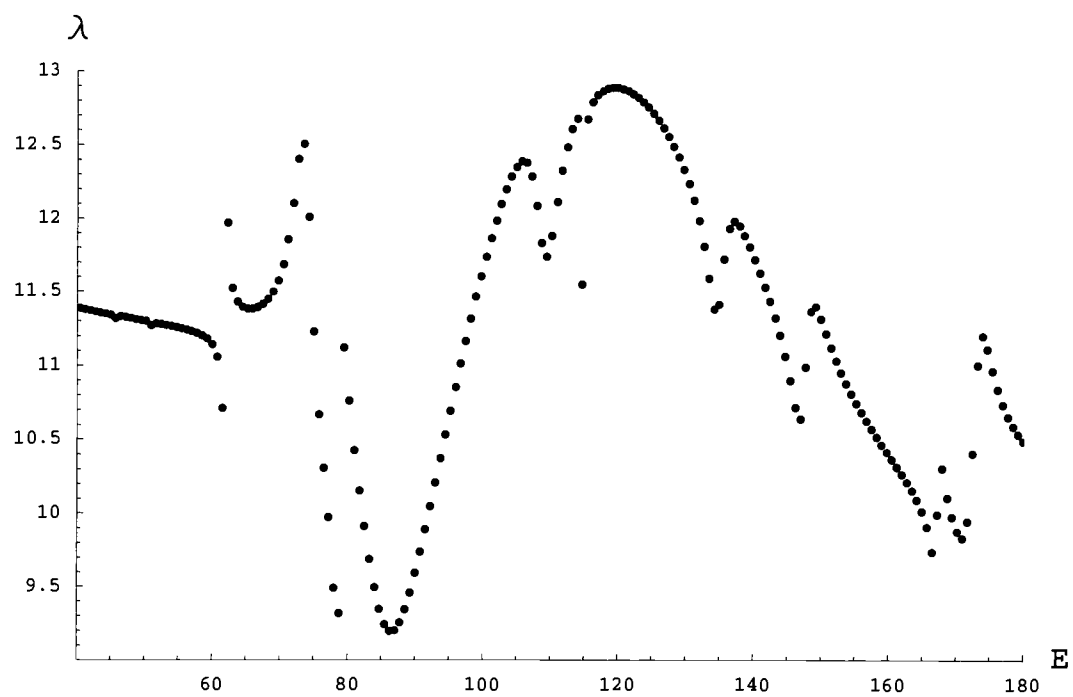


Figure 6.3: Total differential cross section on-axis (top) and  $15^\circ$  off-axis (bottom) for (6.1) with  $V_0 = 1200$ ,  $a = 1.6$  and  $R = 2.5$ .

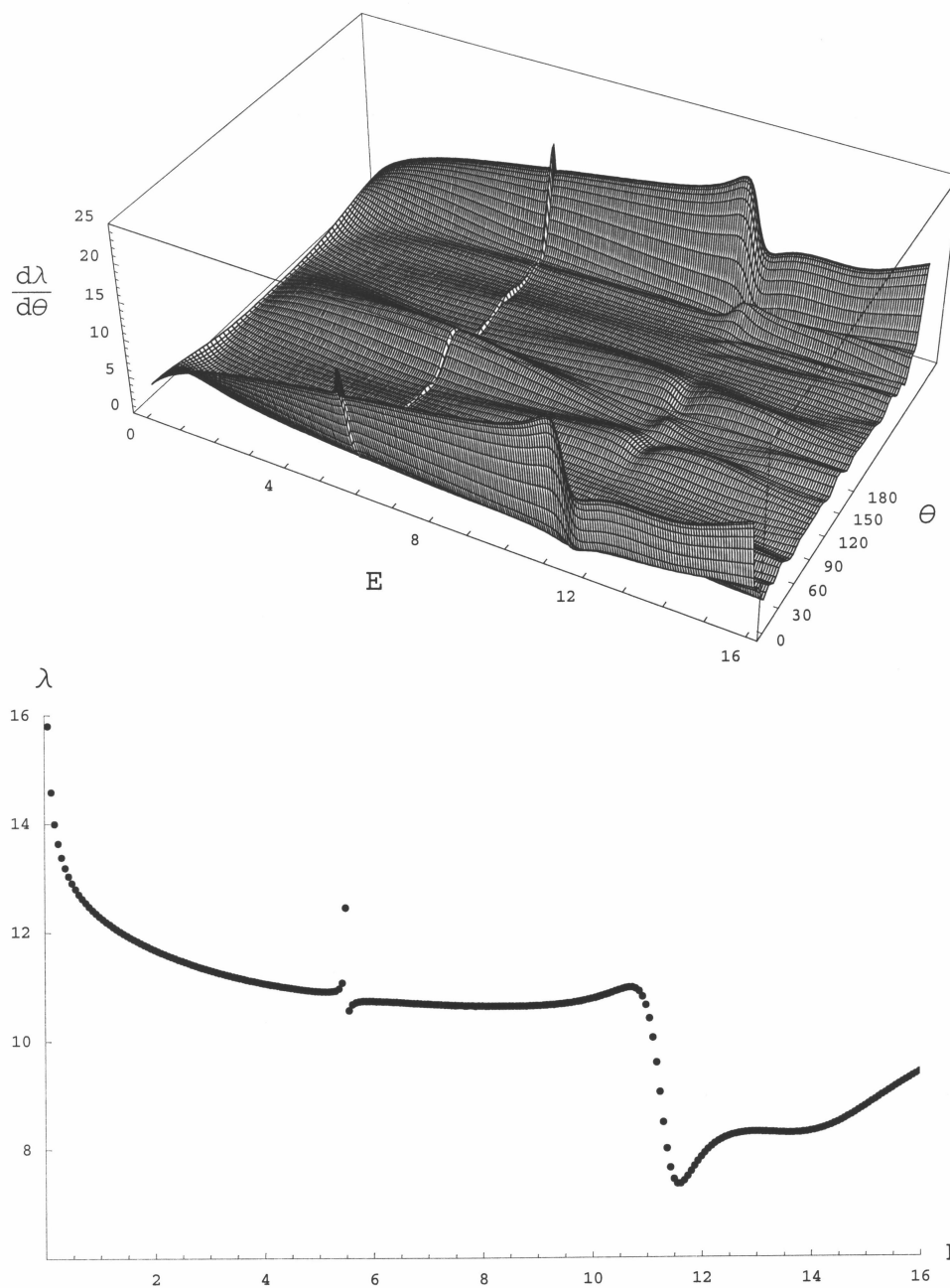


Figure 6.4: Differential cross sectional surface (top) with the corresponding integrated total cross section (bottom) for (6.1) with  $V_o=100$ ,  $a=1.6$ ,  $R=2.5$  and an incident angle of  $0^\circ$ .

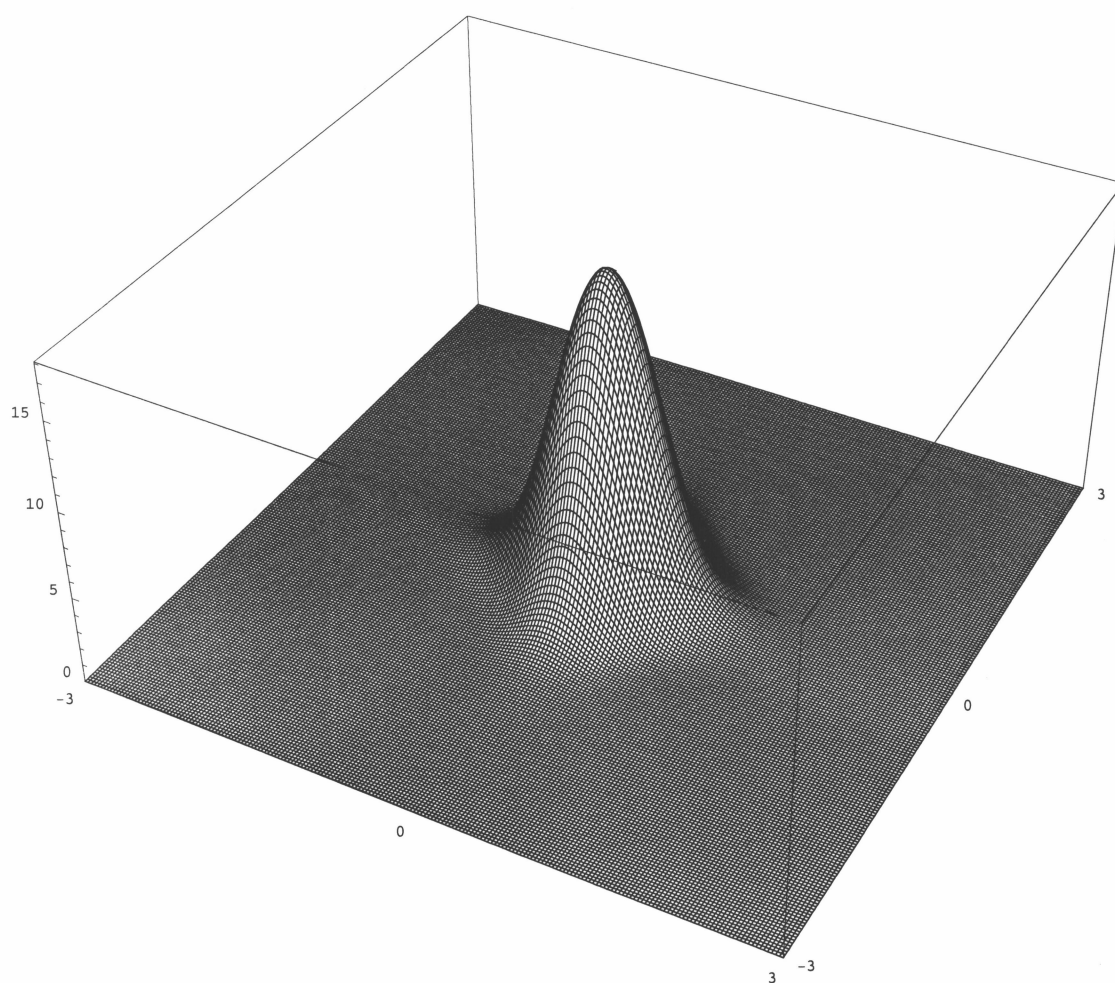


Figure 6.5: Probability density for the first resonance of table 6.2 for which  $V_o=100$ ,  $a=1.6$  and  $E=5.51305$  with normal incidence.

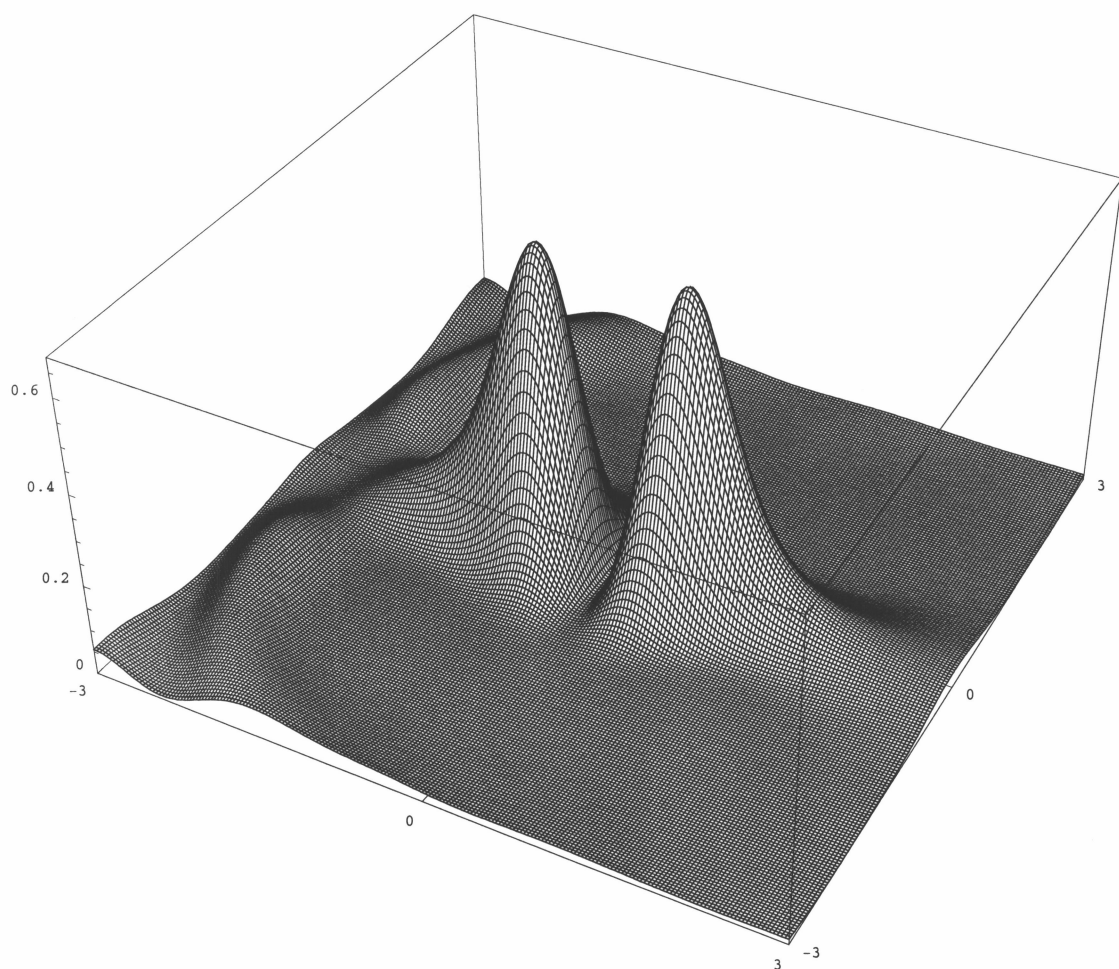


Figure 6.6: Probability density for the second resonance of table 6.2 for which  $V_o=100$ ,  $a=1.6$  and  $E=11.3781$  with normal incidence.

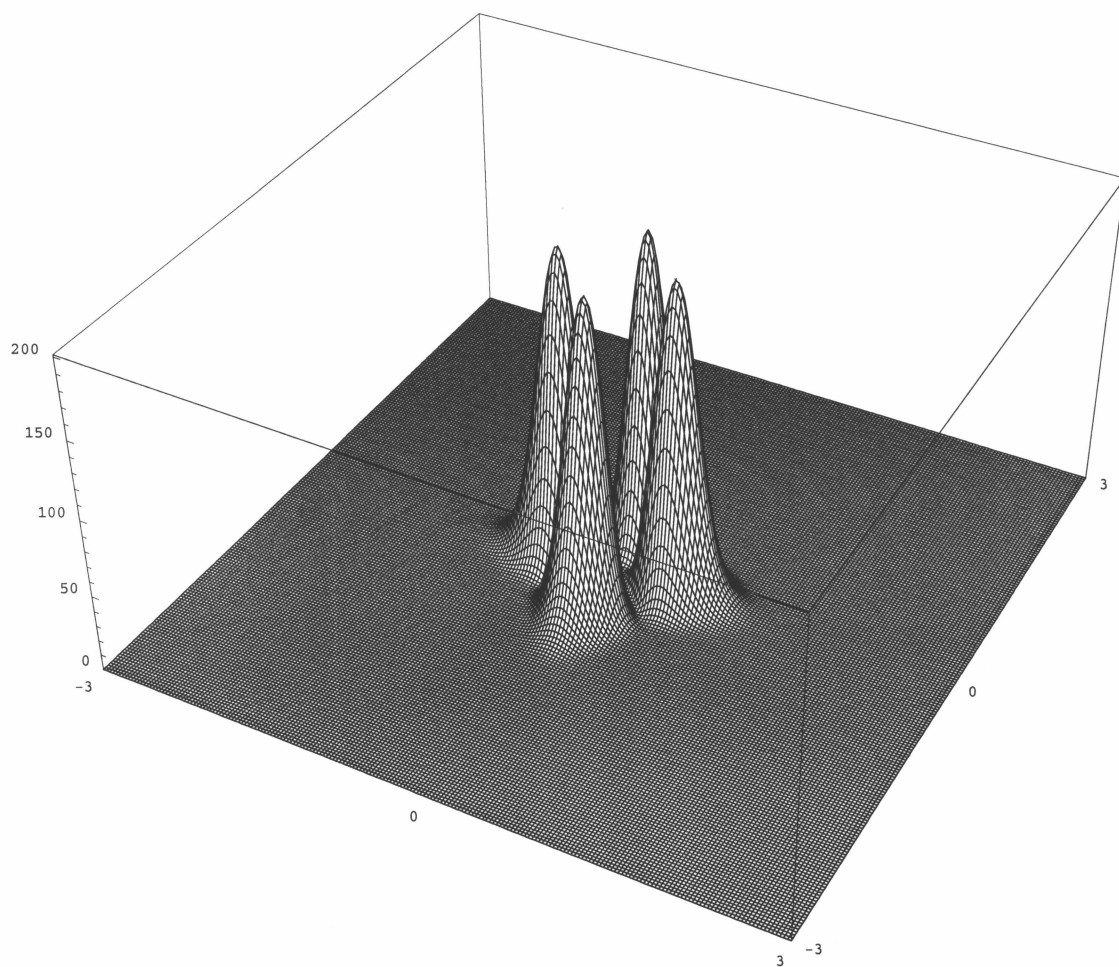


Figure 6.7: Probability density for the third resonance of table 6.2 for which  $V_o = 1200$ ,  $a = 1.6$  and  $E = 45.7994$  with normal incidence.

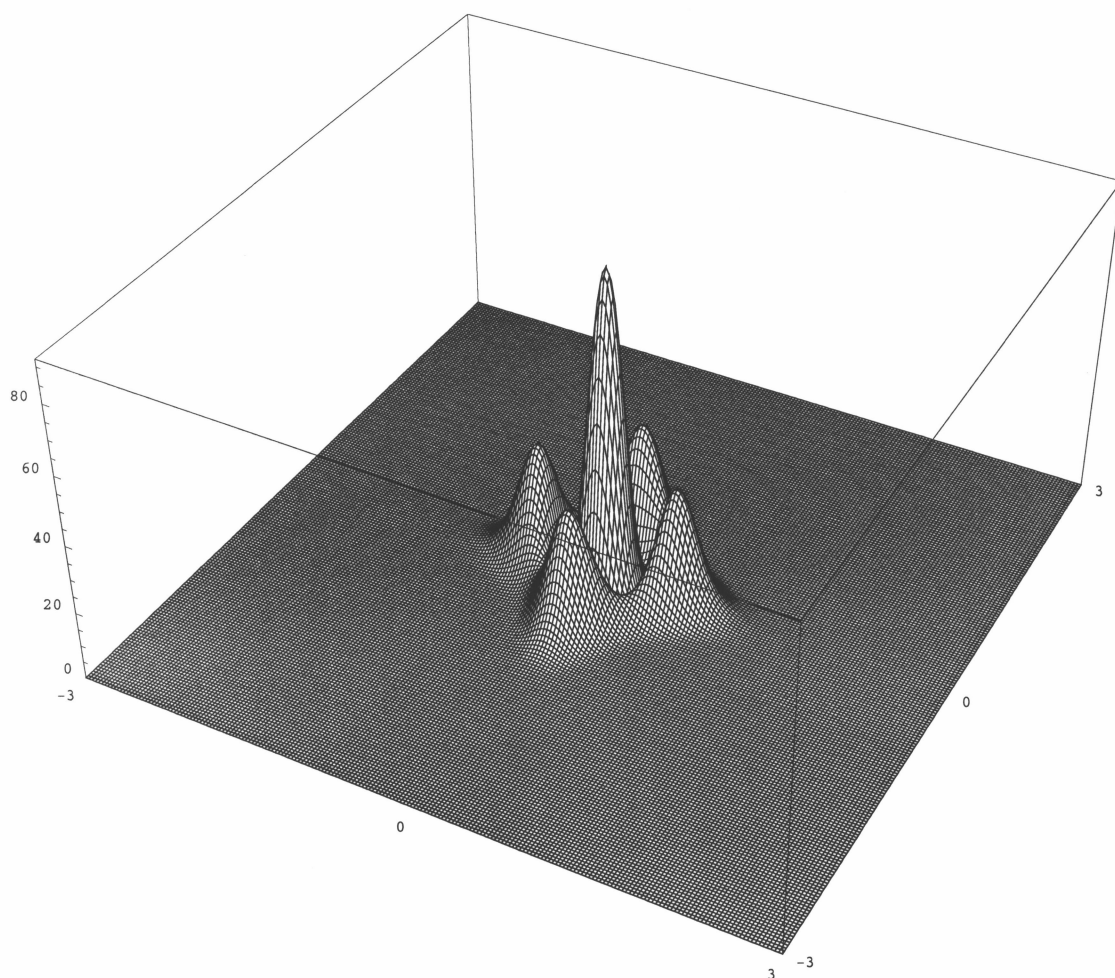


Figure 6.8: Probability density for the fourth resonance of table 6.2 for which  $V_0=1200$ ,  $a=1.6$  and  $E=50.9141$  with normal incidence.

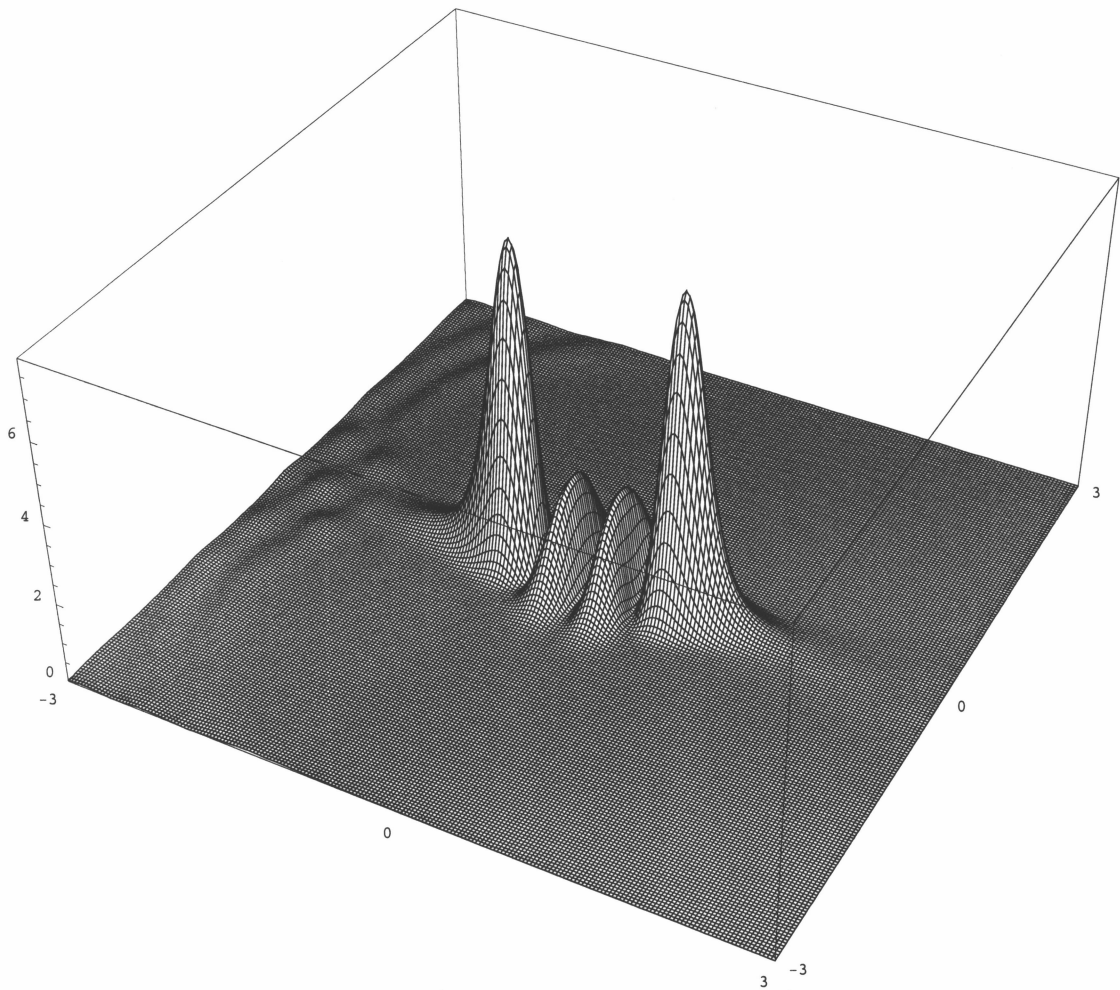


Figure 6.9: Probability density for the fifth resonance of table 6.2 for which  $V_o = 1200$ ,  $a = 1.6$  and  $E = 61.8927$  with normal incidence.

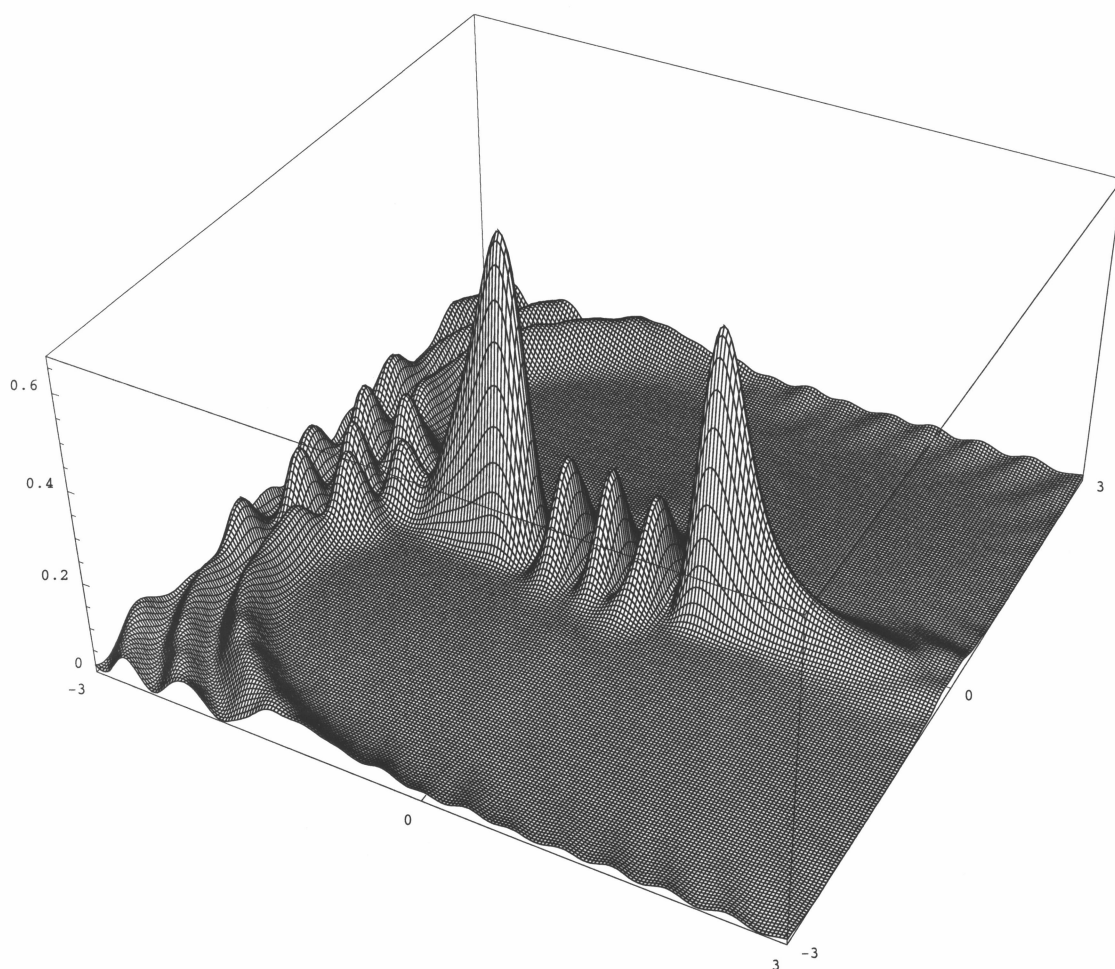


Figure 6.10: Probability density for the sixth resonance of table 6.2 for which  $V_0=1200$ ,  $a=1.6$  and  $E=74.0325$  with normal incidence.

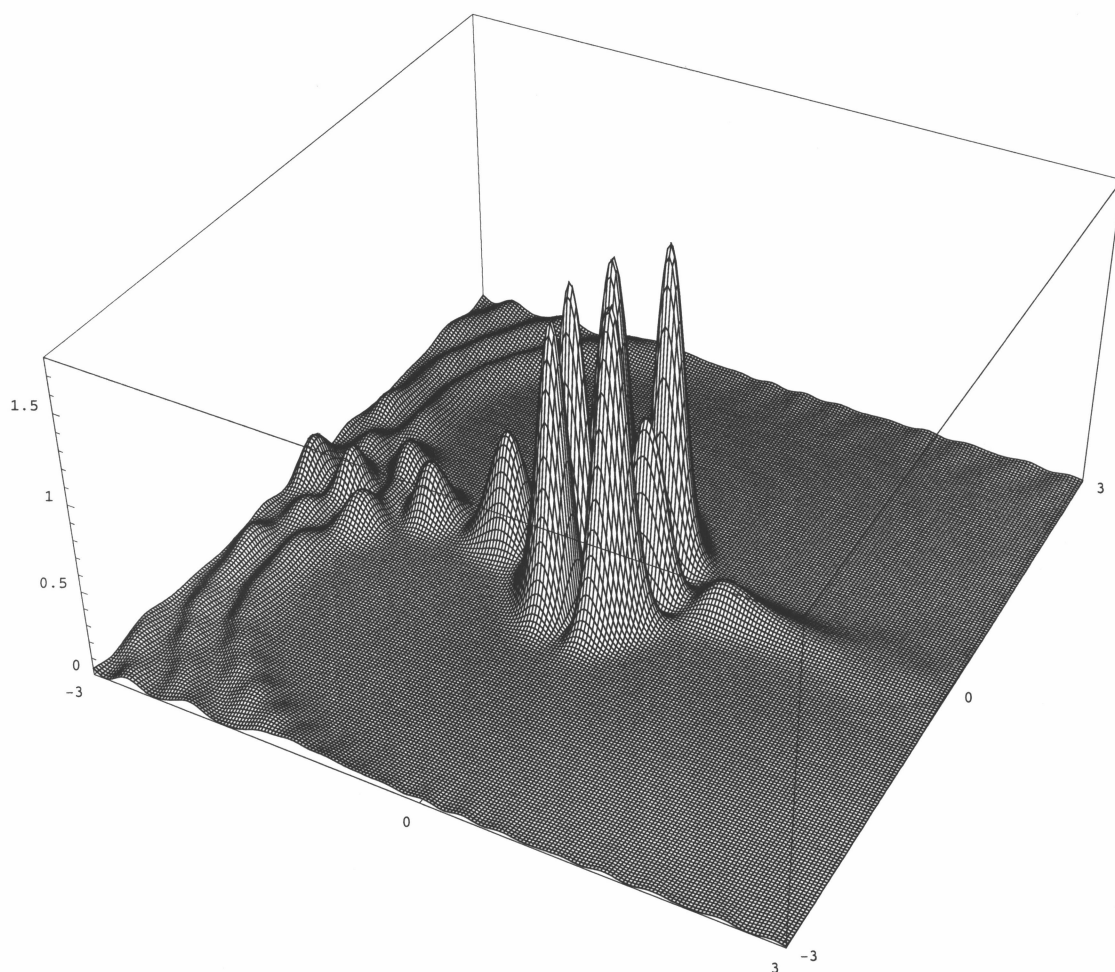


Figure 6.11: Probability density for the seventh resonance of table 6.2 for which  $V_o = 1200$ ,  $a = 1.6$  and  $E = 78.8937$  with normal incidence.

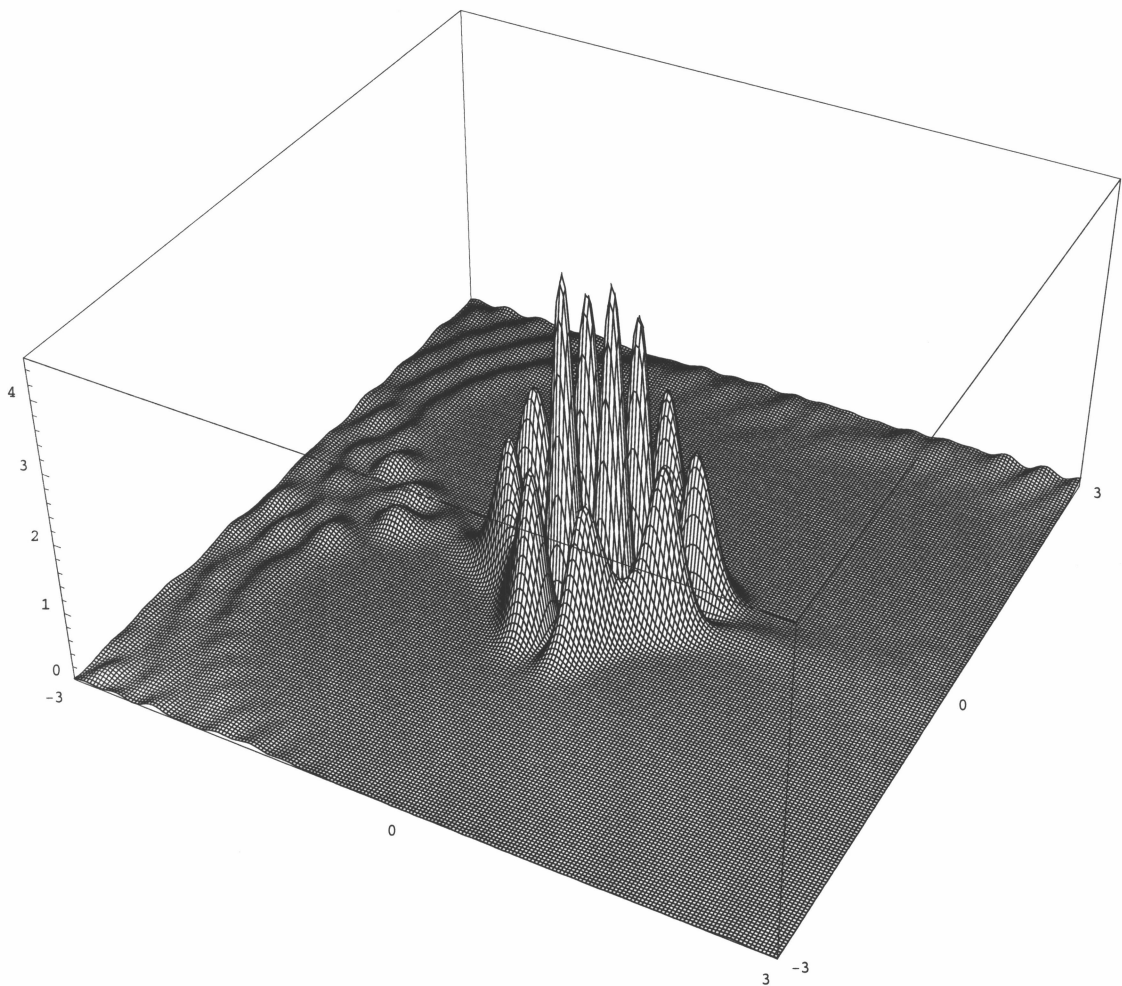


Figure 6.12: Probability density for the eighth resonance of table 6.2 for which  $V_o=1200$ ,  $a=1.6$  and  $E=105.017$ . Here the incident angle is  $\theta_o=\pi/12$ .

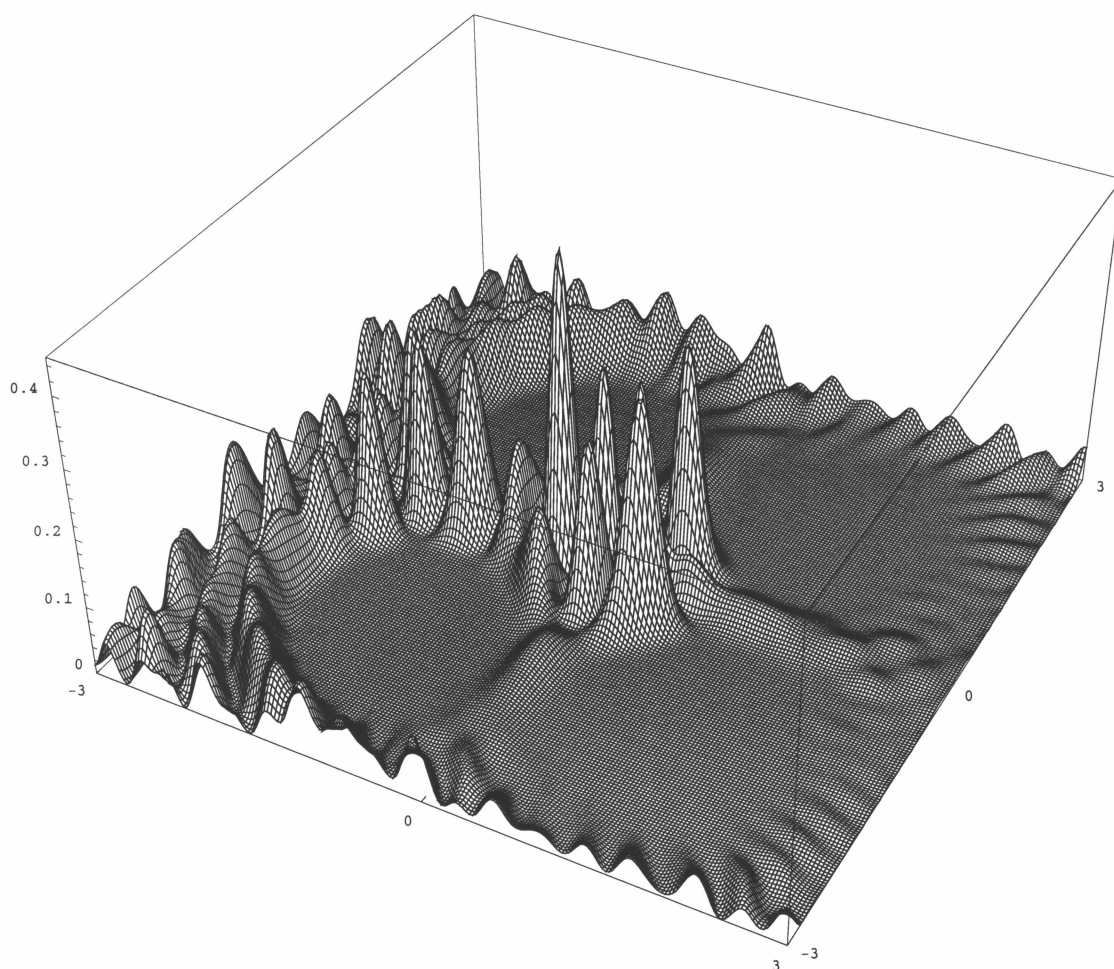


Figure 6.13: Probability density for the ninth resonance of table 6.2 for which  $V_0=1200$ ,  $a=1.6$  and  $E=109.108$  with normal incidence.

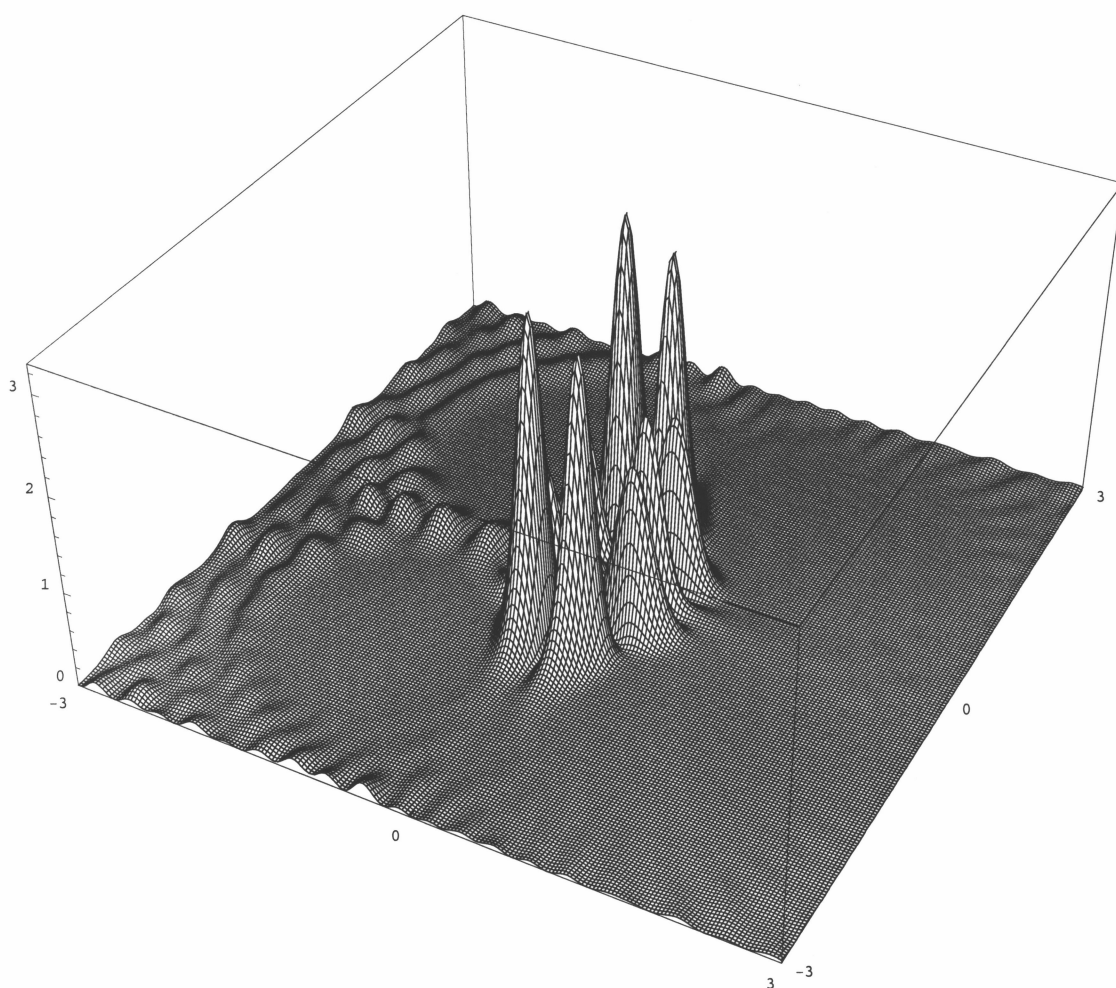


Figure 6.14: Probability density for the tenth resonance of table 6.2 for which  $V_0=1200$ ,  $a=1.6$  and  $E=114.780$  with normal incidence.

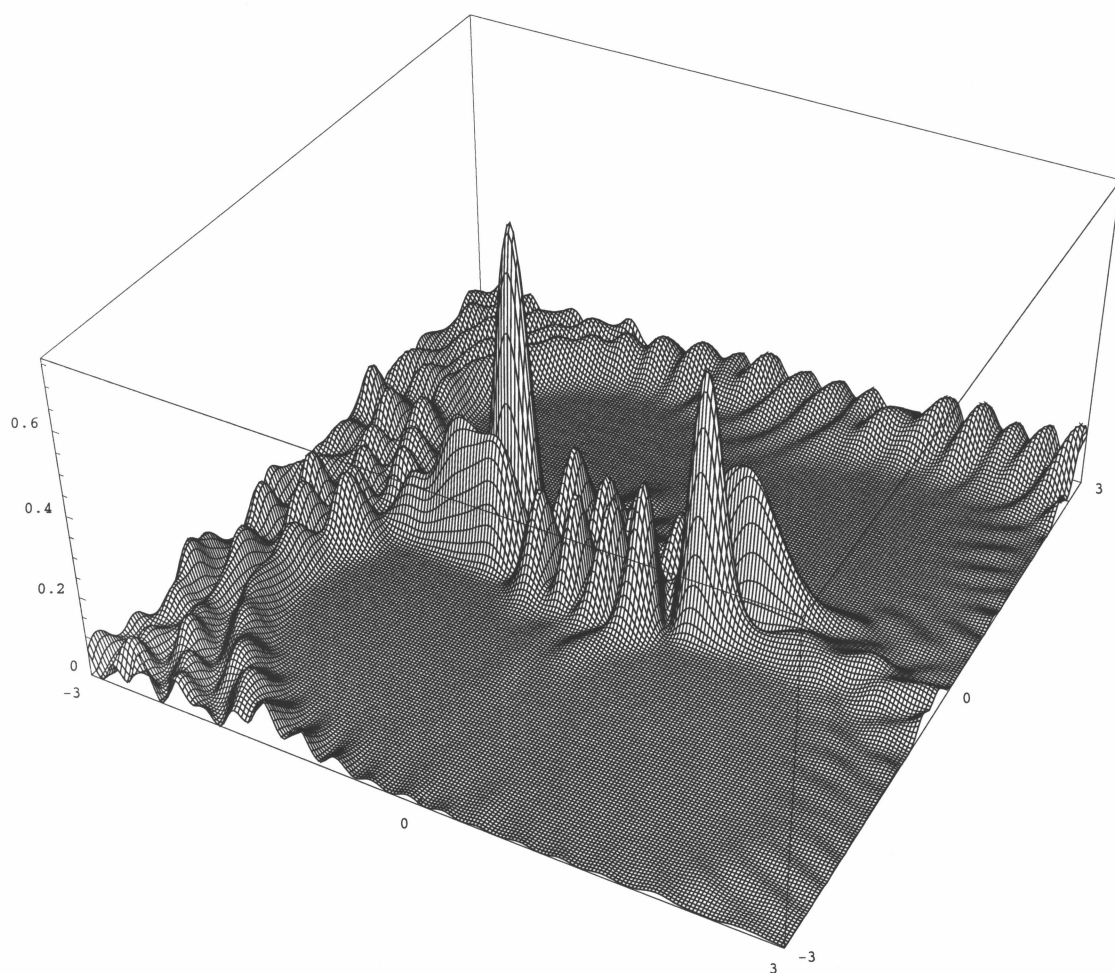


Figure 6.15: Probability density for the eleventh resonance of table 6.2 for which  $V_o = 1200$ ,  $a = 1.6$  and  $E = 131.429$ . Here the incident angle is  $\theta_o = \pi/12$ .

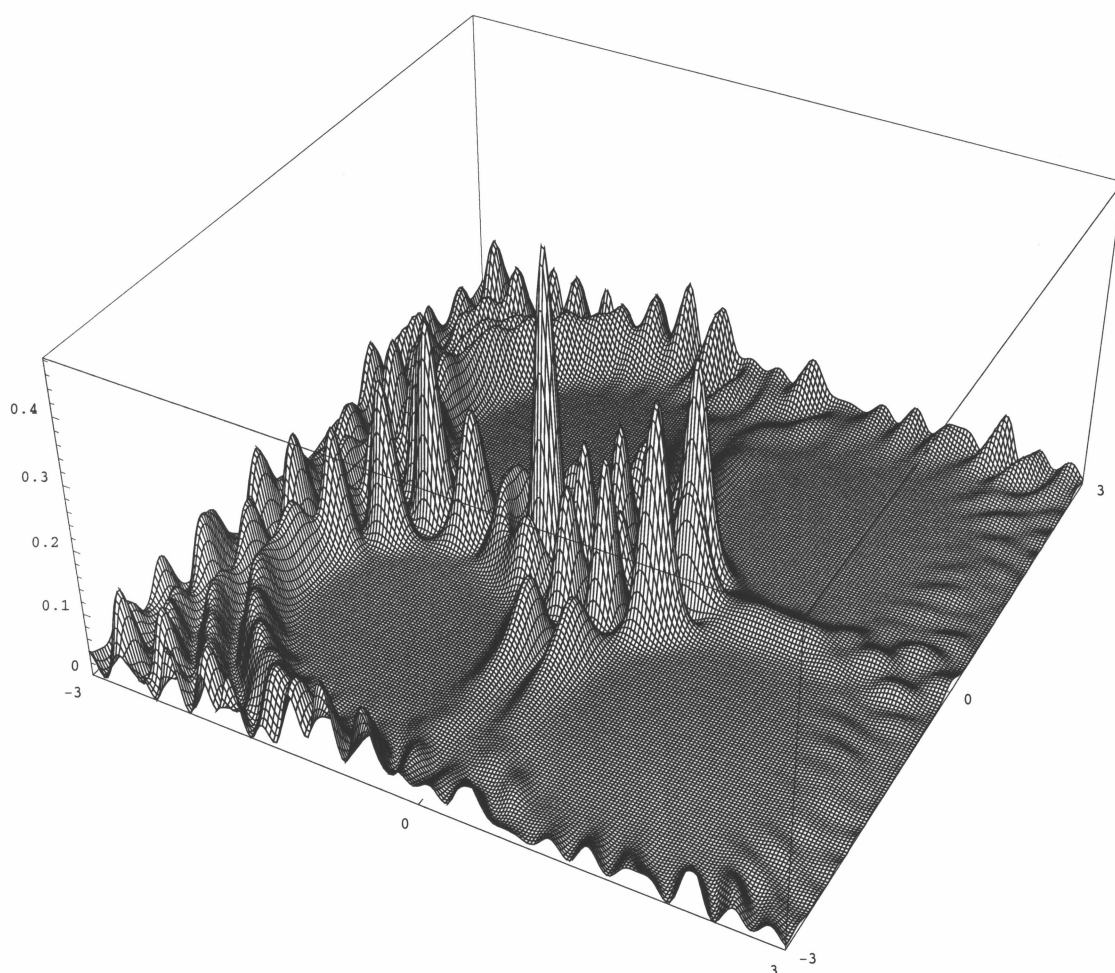


Figure 6.16: Probability density for the twelfth resonance of table 6.2 for which  $V_o=1200$ ,  $a=1.6$  and  $E=134.587$  with normal incidence.

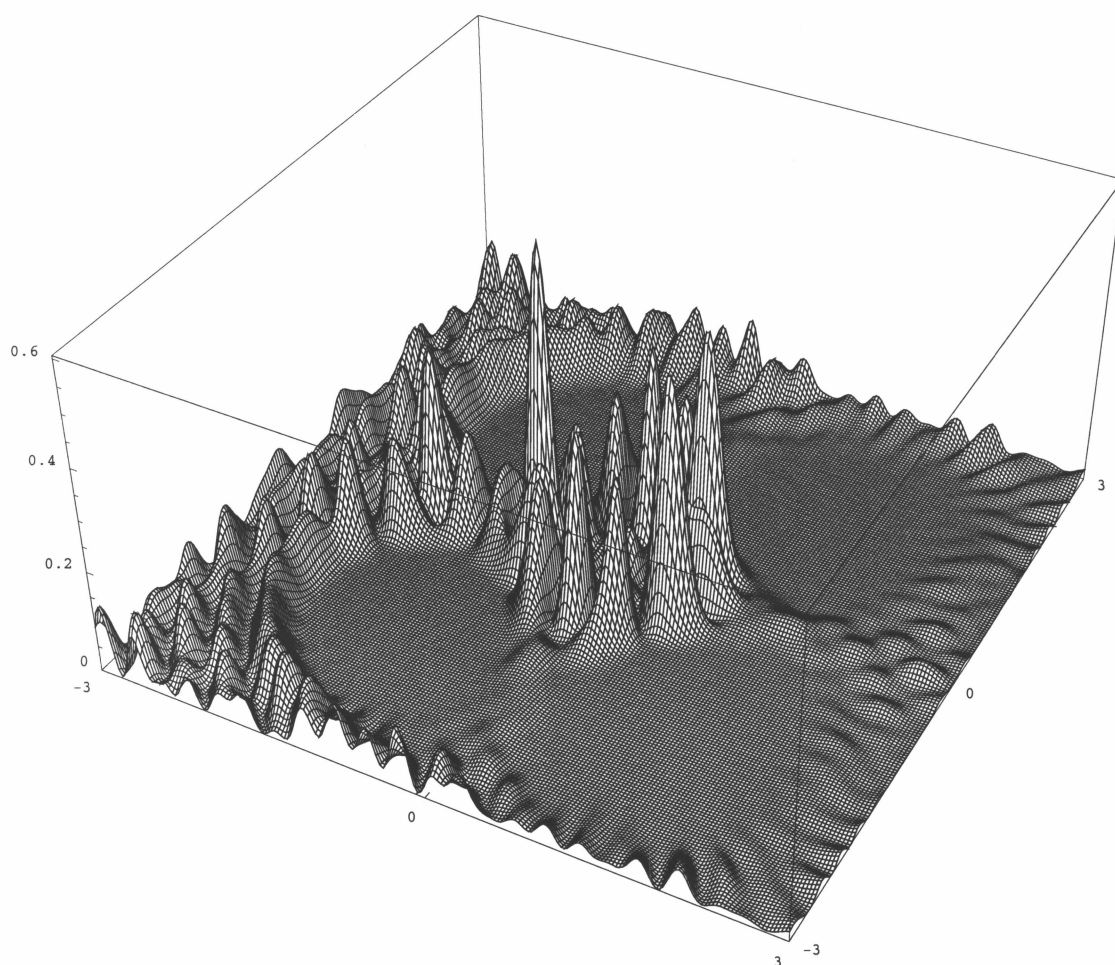


Figure 6.17: Probability density for the thirteenth resonance of table 6.2 for which  $V_0 = 1200$ ,  $a = 1.6$  and  $E = 147.285$  with normal incidence.

Corresponding symmetries may be quickly determined for most of these resonances. The wave function of the third tabulated resonance, for example, given in figure 6.21 is seen from figure 6.2 to belong to the  $B_1$  irreducible representation which has inversion symmetry about a line which intersects the centers of either pair opposing sides. The wave function of the eighth resonance, on the other hand, is antisymmetric with respect to either of these two lines as shown in figures 6.23 and 6.24. As a result, the corresponding peak is absent from the upper cross section of figure 6.3, which has normal incidence, and appears only in the lower. A similar analysis of their wave functions assigns the first and second tabulated resonances to the  $A_1$  and  $E$  representations respectively. The fourth resonance is the second occurrence of the  $A_1$  symmetry and its wave function will thus display a single nodal line at a fixed radius within the scatterer as shown in figure 6.19. At least one representative from each irreducible symmetry class is displayed in figures 6.18-6.25.

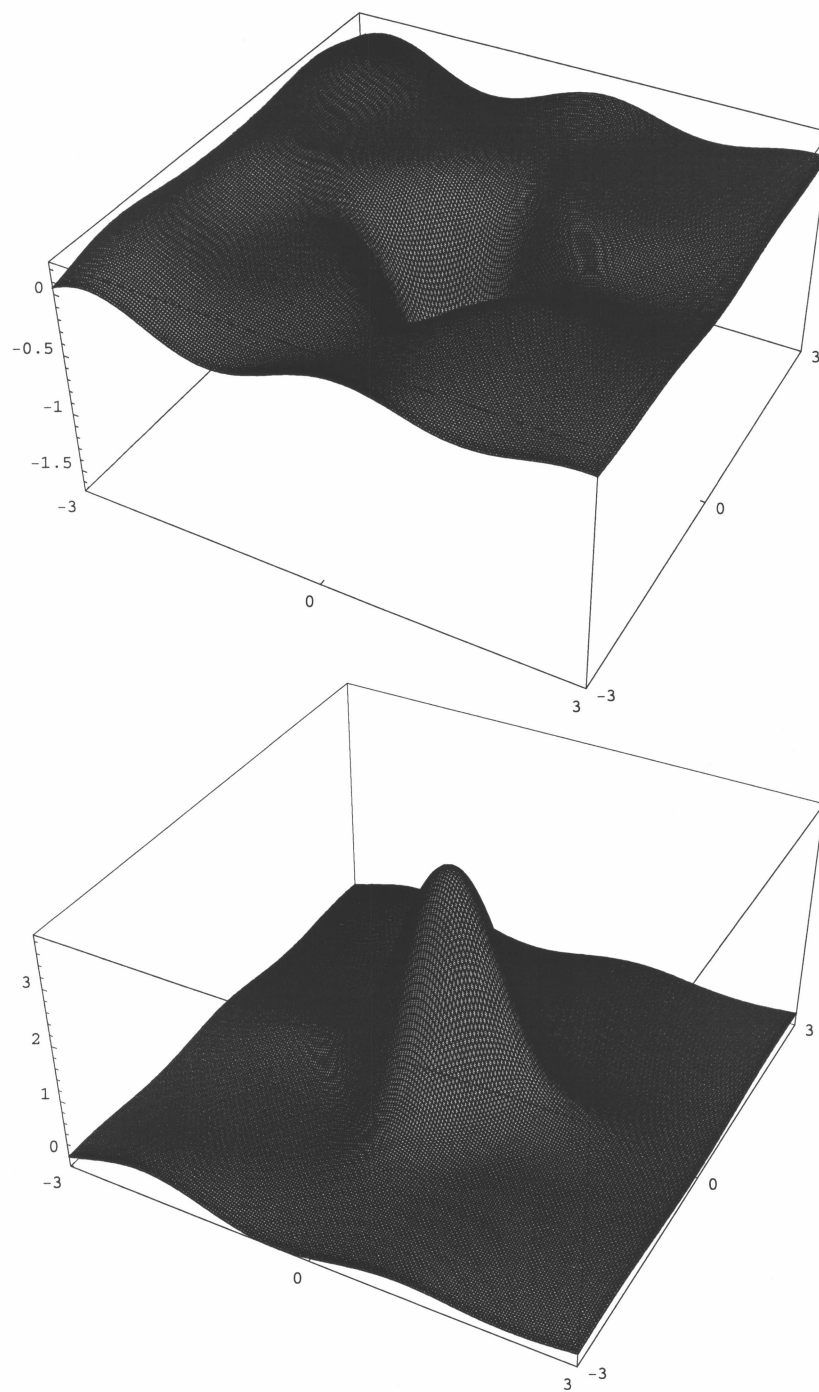


Figure 6.18: Real (top) and imaginary (bottom) parts of the wave function belonging to the first resonance of table 6.2 which carries the fundamental  $A_1$  symmetry.

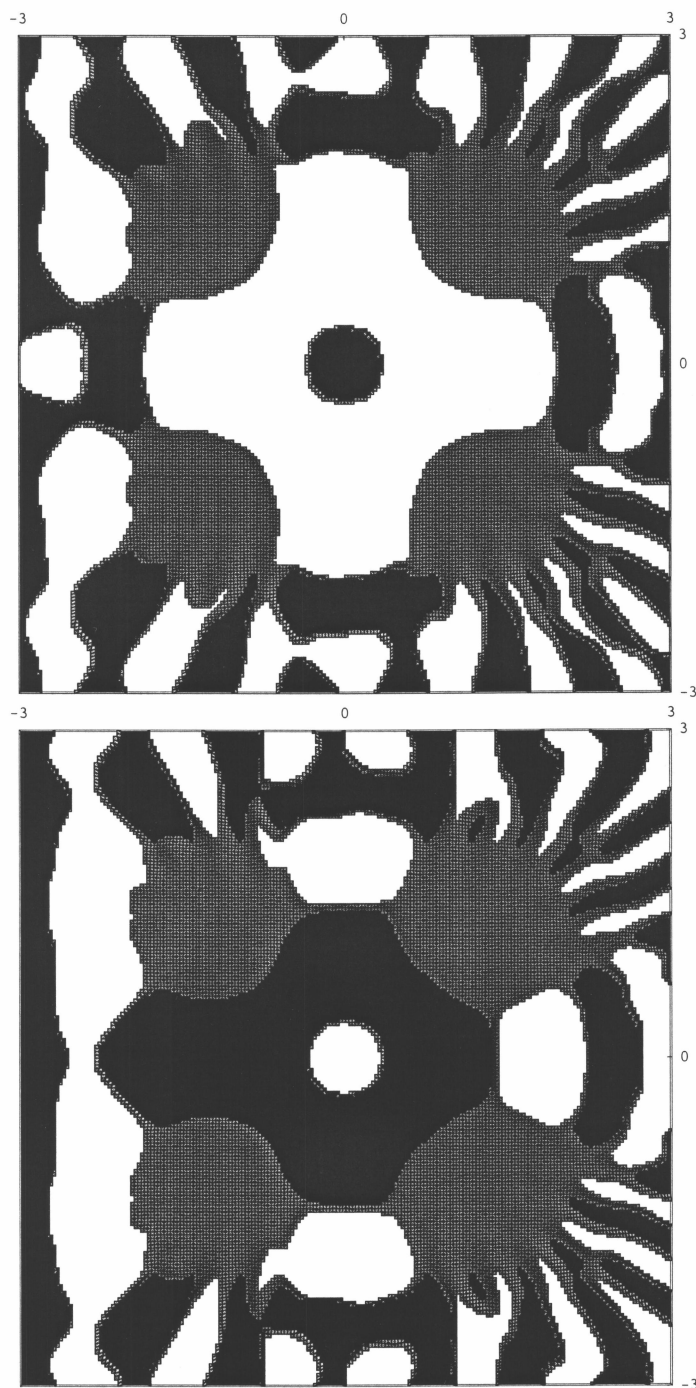


Figure 6.19: Real (top) and imaginary (bottom) parts of the fourth resonance's clipped wave function showing the second  $A_1$  symmetry (note the single nodal ring at fixed radius). Black  $< -0.002$  < Gray  $< 0.002$  < White (top). The incident plane wave is seen to approach from the left.

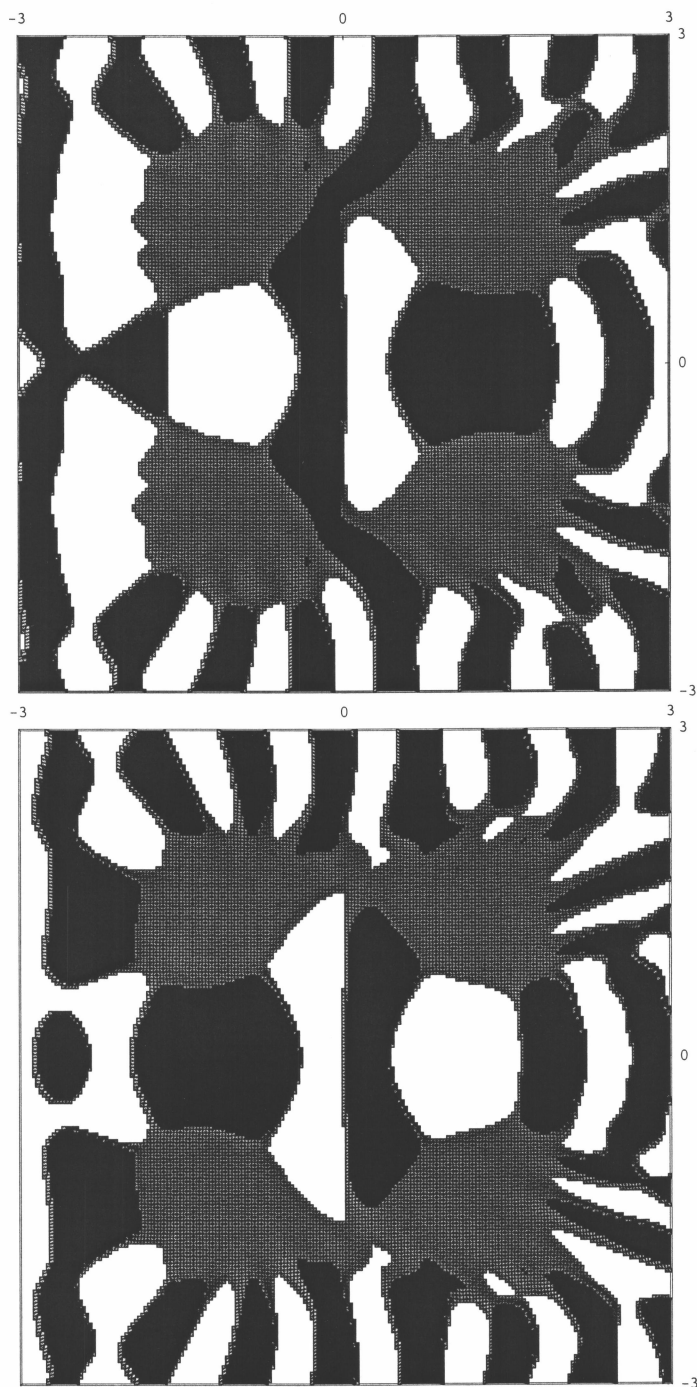


Figure 6.20: Real (top) and imaginary (bottom) parts of the fifth resonance's clipped wave function showing  $E$  symmetry. Black  $< -0.001 < \text{Gray} < 0.001 < \text{White}$  (top). The incident plane wave is seen to approach from the left.

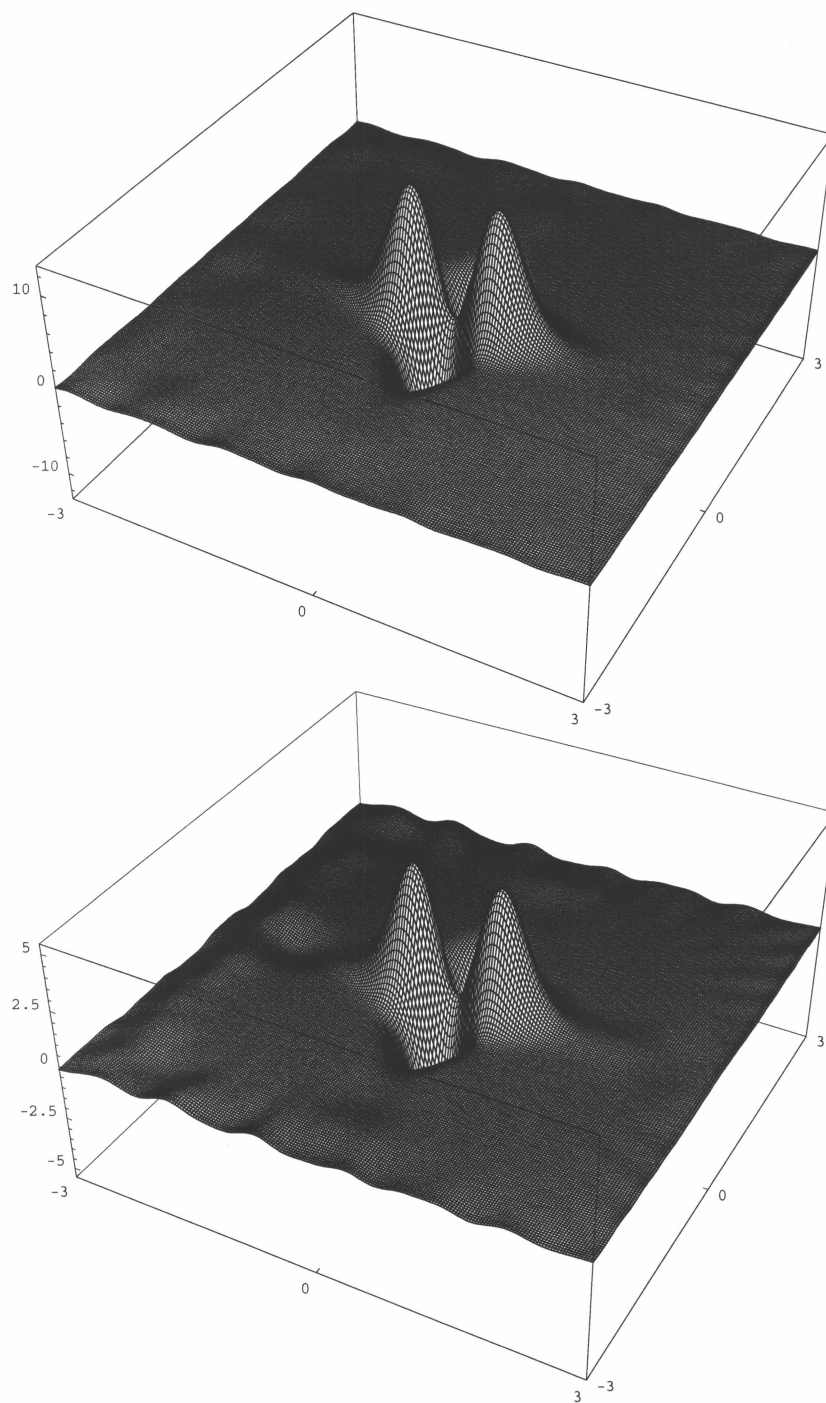


Figure 6.21: Real (top) and imaginary (bottom) parts of the wave function belonging to the third resonance of table 6.2 which carries  $B_1$  symmetry.

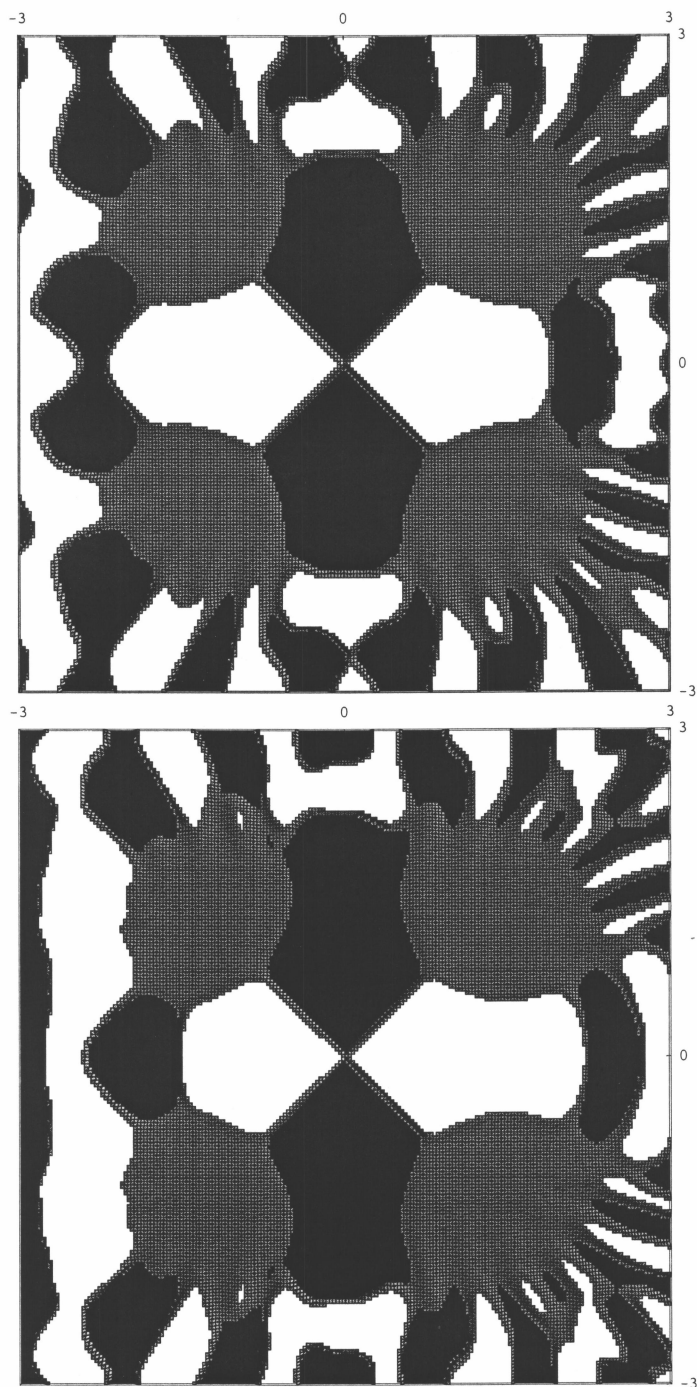


Figure 6.22: Real (top) and imaginary (bottom) parts of the third resonance's clipped wave function showing  $B_1$  symmetry. Black  $< -0.005 < \text{Gray} < 0.005 < \text{White}$  (top). The incident plane wave is seen to approach from the left.

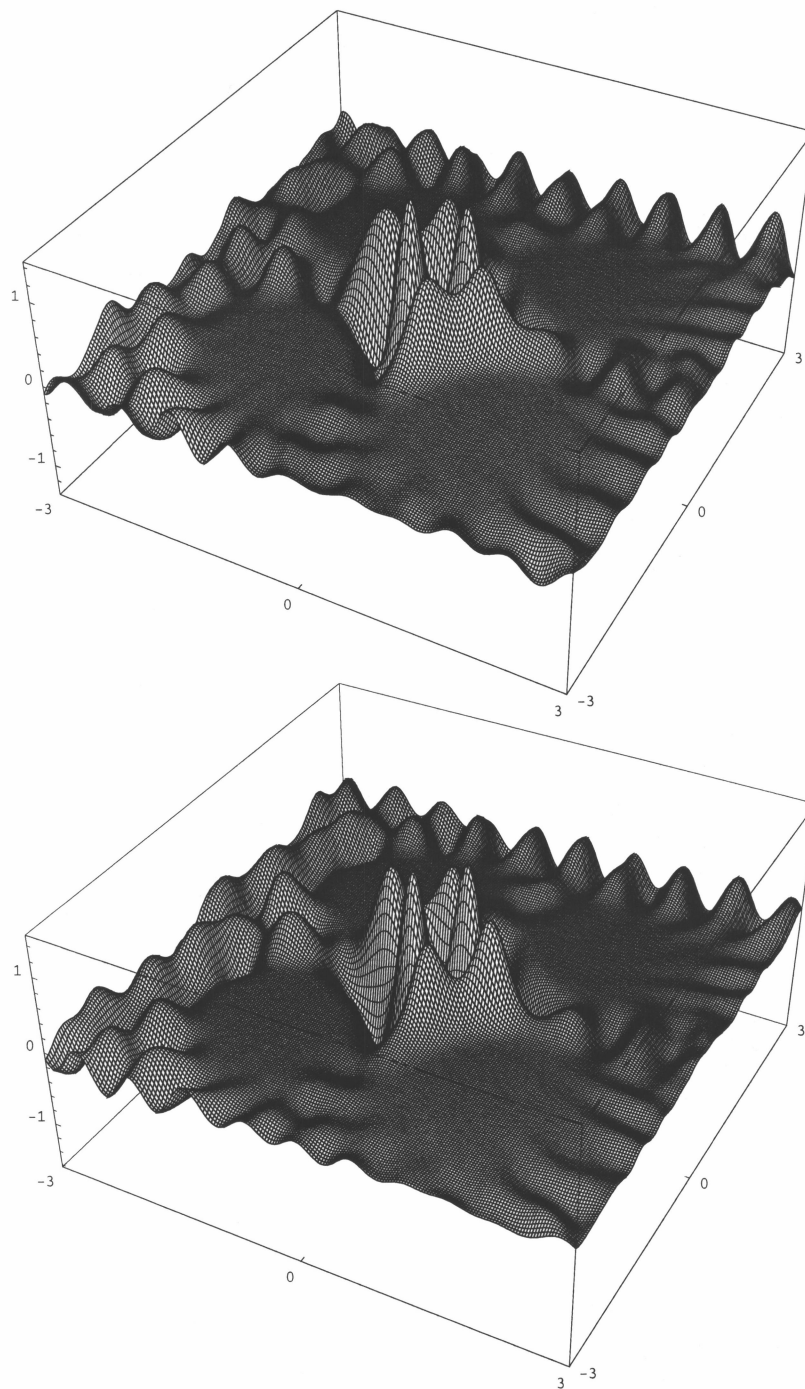


Figure 6.23: Real (top) and imaginary (bottom) parts of the wave function belonging to the eighth resonance of table 6.2 which carries  $B_2$  symmetry. The incident plane wave is seen to approach from the left at a  $15^\circ$  downward angle.

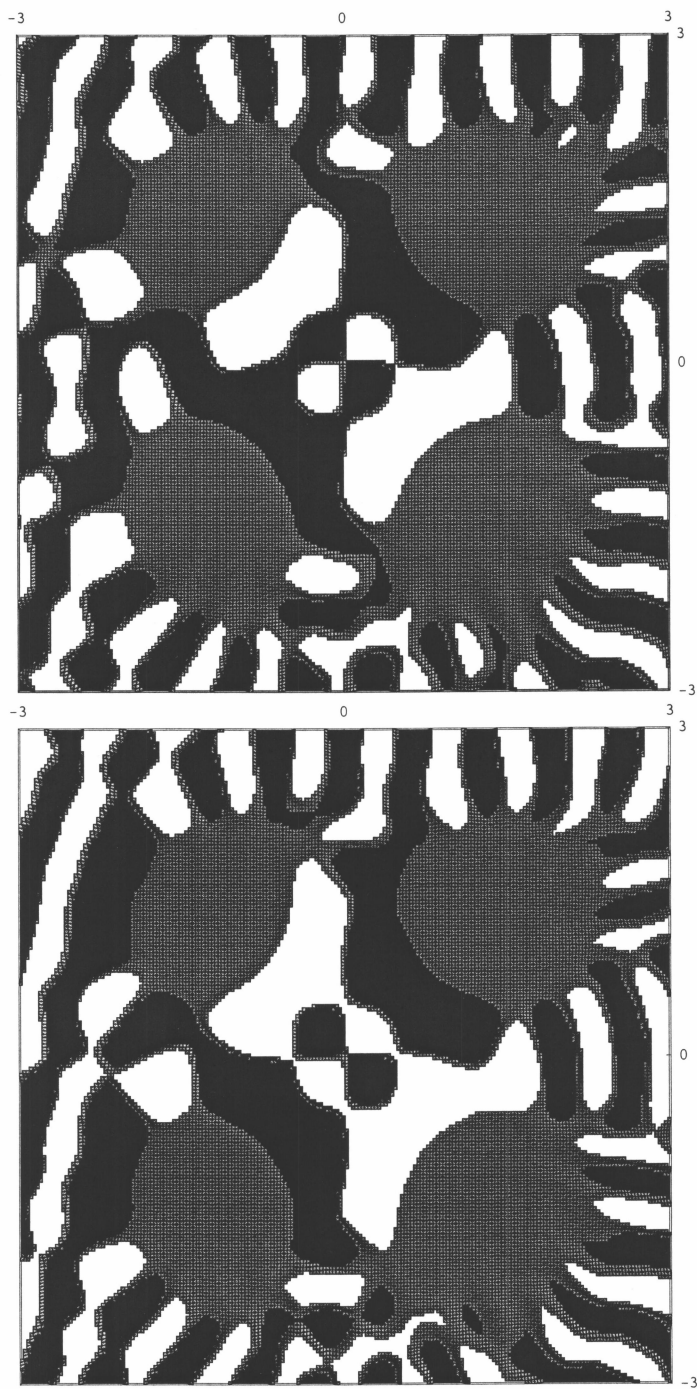


Figure 6.24: Real (top) and imaginary (bottom) parts of the eighth resonance's clipped wave function showing  $B_2$  symmetry. Black  $< -0.01 < \text{Gray} < 0.01 < \text{White}$  (top). The incident plane wave is seen to approach from the left at a  $15^\circ$  downward angle.

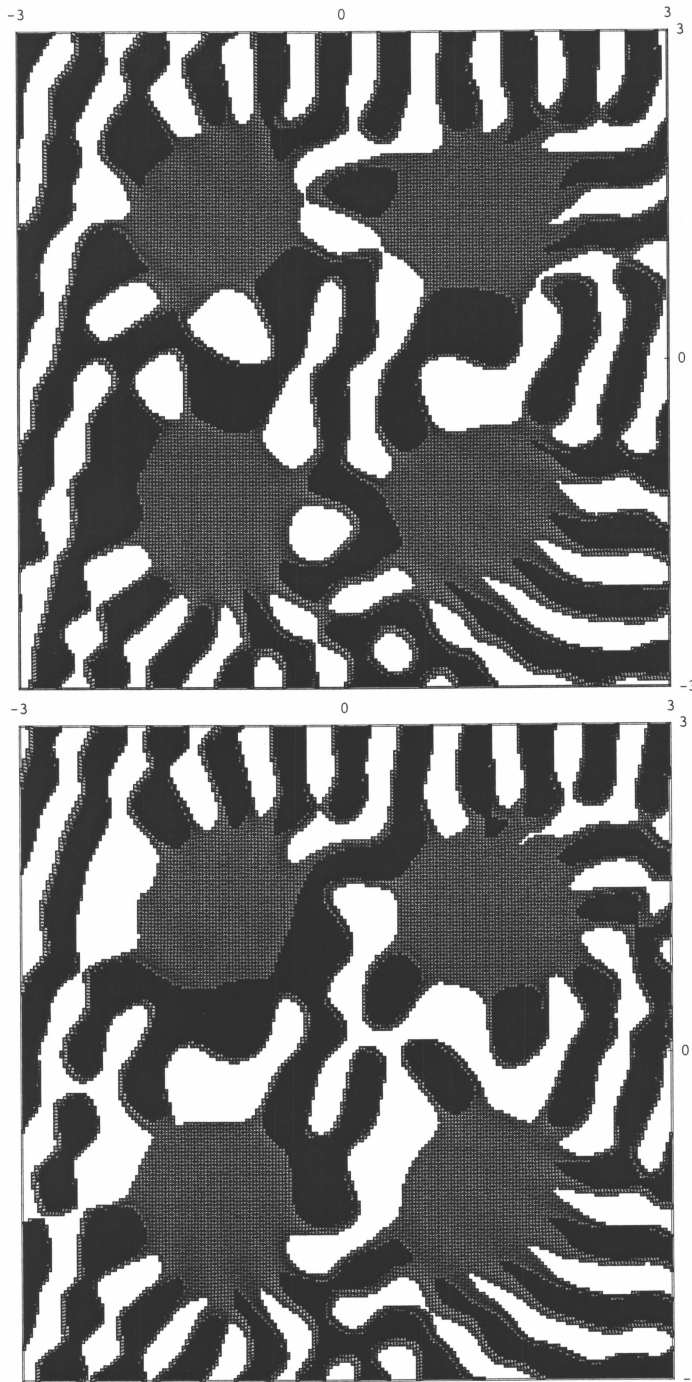


Figure 6.25: Real (top) and imaginary (bottom) parts of the eleventh resonance's clipped wave function showing  $A_2$  symmetry. Black  $< -0.005 < \text{Gray} < 0.005 < \text{White}$  (top). The incident plane wave is seen to approach from the left at a  $15^\circ$  downward angle.

The orders given in table 6.2 show that wave function symmetries belonging to the two dimensional  $E$  representation are degenerate and correspond to double poles of the wave operator. The order of each pole is determined by evaluating the determinant  $|\Omega_E^{-1}|$  on a ring, with a small radius, of complex energies that encompass the energy of the pole. In a small neighborhood about the pole, the complex function will be governed by the pole structure and the function  $g(z)$  may be taken to vary slowly enough that it can be approximated by a constant on a ring with a sufficiently small radius.

$$f(z) = \frac{g(z)}{(z - z_0)^n} \xrightarrow{z \rightarrow z_0} \frac{C e^{in\theta}}{\|z - z_0\|^n} \quad (6.3)$$

When graphing the real and imaginary parts of the determinant on the periodic interval  $[0, 2\pi]$ , each part will exhibit an even number of sign changes, returning to the initial value. The order of the pole is equated with the number of pairs of sign changes.

The irreducible representations comprise a type of symmetry basis from which less symmetric waves may be constructed, such as those belonging to the sixth and seventh resonance from table 6.2. We notice from table that the spacing between these two resonances is similar to the width of the lower one. A hybridization of wave function symmetries is thus expected for the overlapping resonances. This mechanism is somewhat analogous to one that was offered by Ericson and others [47, 48, 49], during the early part of the 1960's, as an explanation for fluctuations appearing in nuclear cross sections for transition state spectroscopy experiments. The assumption is that a group of resonances may exist whose widths exceed nearest neighbor spacings. From the energy uncertainty argument, (3.17), all the intermediate states within the group are interpreted as being simultaneously populated. The consequent interference results in the Ericson fluctuations appearing in cross sections (compare this with figure 6.3).

Upon investigating the wave functions of the sixth and seventh tabulated resonances, we find their real parts to be more strongly mixed than the imaginary parts for which hybridization is minimal. We attempt to separate the real parts of the wave function and reveal their symmetry by a rotation of the state vectors. As diagramed in figure 6.26, we add to each real part a piece of the other,

$$\begin{aligned} \text{Re}(\Psi_{6'}) &= 0.08 \text{Re}(\Psi_7) \\ \text{Re}(\Psi_{7'}) &= -0.2 \text{Re}(\Psi_6). \end{aligned} \quad (6.4)$$

Because the seventh tabulated resonance is comparatively much narrower than the sixth,  $\Psi_7$  will be larger than  $\Psi_6$  in the region internal to the scatterer. The resulting representative vectors, shown in figure 6.26, thus have different lengths and we expect their ratio to be similar to that of

the coefficients  $\alpha$  and  $\beta$  given in (6.4). We point out that because the scattering wave functions are not square-integrable, they are not normalizable in the conventional sense. In figure 6.27 we

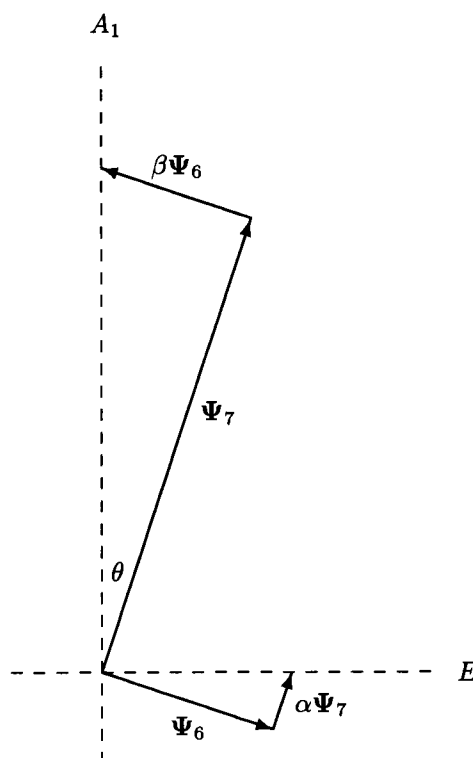


Figure 6.26: Schematic for the rotation of the real parts of mixed state vectors, neglecting normalization, belonging to the sixth and seventh resonance.

display the real part of the wave function for the sixth resonance both before and after rotation. In figure 6.28 we do the same for the seventh. After rotation, we see that the real part of the sixth resonance displays the angular independence of the  $A_1$  representation. Being the third occurrence of this representation, we expect to see two nodal rings. The symmetry is not as evident as others displayed due to distortions stemming from the fact that this is among the two widest resonances, resulting in a larger symmetry-breaking effect of the incident wave. In figure 6.28 we see that the vertical line of reflection, as well as the horizontal nodal lines, has become slightly cleaner after rotation. Being the narrower of the two resonances, the changes are relatively slight.

Like the eighth, the eleventh resonance from table 6.2 can be seen only from the lower cross

section of 6.3, indicating that the inversion symmetry about the x-axis must be broken to excite this resonance. That this is the case is even evident for this resonance from the resulting probability density plotted in figure 6.15 with an angle of incidence equal to  $\pi/12$ .

Vector plots, 6.29, of the current density and velocity field as calculated from (3.9) have been included to show that these more stable resonances correspond to classical multiple reflection events. Flow is maintained across the scatterer at resonance but the velocity drops off as the probability density peaks within the scatterer's interior region, indicative of particles undergoing numerous reflections within the potential before escaping. Upon comparing the square profile of the low velocity region in figure 6.29 to the square footprint of the probability density internal to the scatterer, given in figure 6.5, we notice the relative orientation of each square is rotated with respect to the other by an angle of  $45^\circ$ . This is due to the fact that the low velocity region in the vector plot reflects the areas where the potential's four Gaussian peaks are seated in addition to the region internal to them. The probability peak, however, is confined only to the region internal to the scatterer and does not occupy the four areas where the potential is large and expels the wave function.

Quantum pinching has also been demonstrated for the first two resonances in table 6.2, establishing it as a universal feature. To show this, figures for the real (6.31) and imaginary (6.32) parts of the wave function, in addition to the probability density (6.30), have been included for an energy of 5.43750 that falls just below the energy of the fundamental resonance at 5.51305.

From more panoramic views of the probability densities, such as the one given in 6.33, one can see clear dips in the particle densities behind the scatterer. These shadows, opposite the incident wave, have also been seen and reported for azimuthally symmetric scatterers [50]. In addition to the shadowing phenomenon, these panoramic views display the complex interference patterns that result between the incident and scattered waves.

Producing a more filamentary style repeller by increasing the interpeak distance to  $R=6.0$ , we chose to additionally verify the most stable resonance among those graphed by Gaspard *et al.* [27] for four hard discs in a square geometry. An exact value is not reported by Gaspard *et al.* but an estimate taken from their graph would be  $(k_r, k_i) = (0.55, 0.035)$ . With values set at  $V_o = 1200$  and  $a = 1.6$ , as before, we found this resonance at  $(k_r, k_i) = (0.6729, 0.0056)$ . Because the parameters used were fit at  $k_o = 11.547$ , we are not surprised that our resonance is slightly higher and narrower due to the slight increase in width of the potential's Gaussian contours at this lower energy.

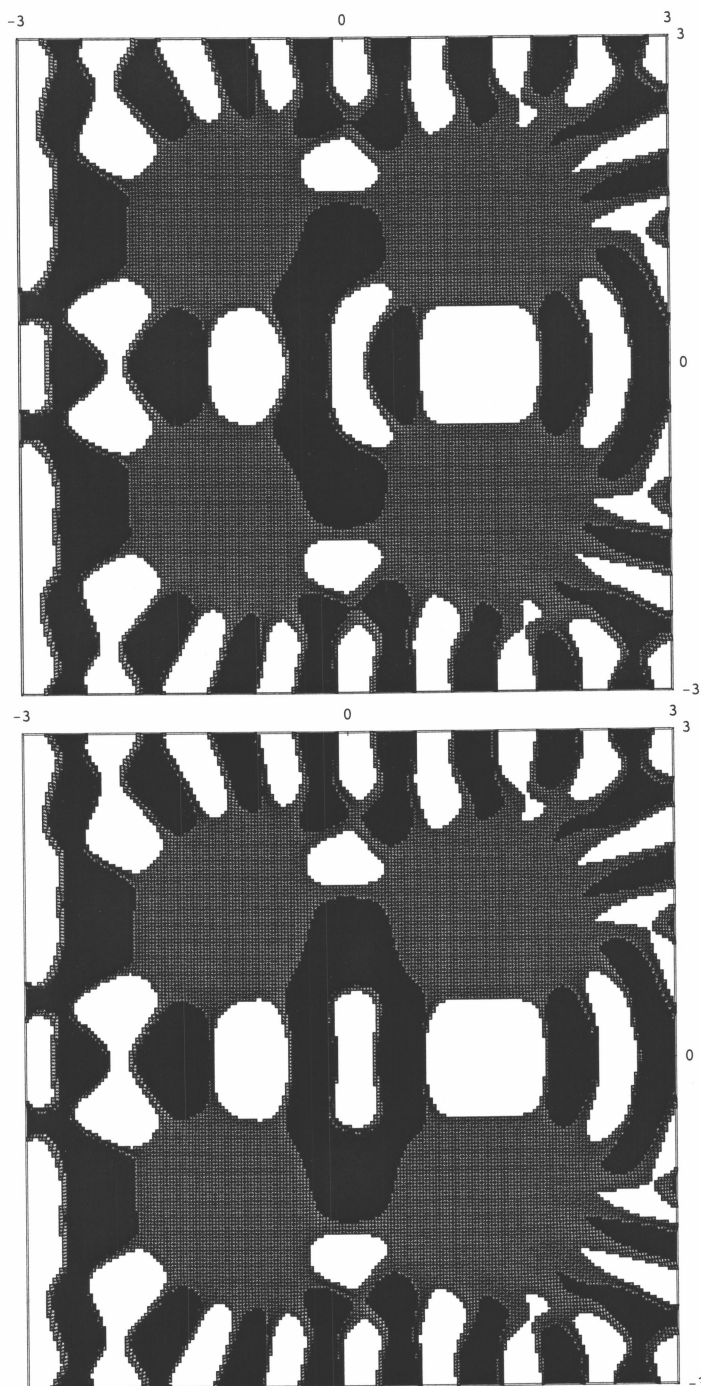


Figure 6.27: Real (top) and rotated (bottom) part of the sixth resonance's clipped wave function showing  $A_1$  symmetry. Black  $< -0.005 < \text{Gray} < 0.005 < \text{White}$  (top). The incident plane wave is seen to approach from the left.

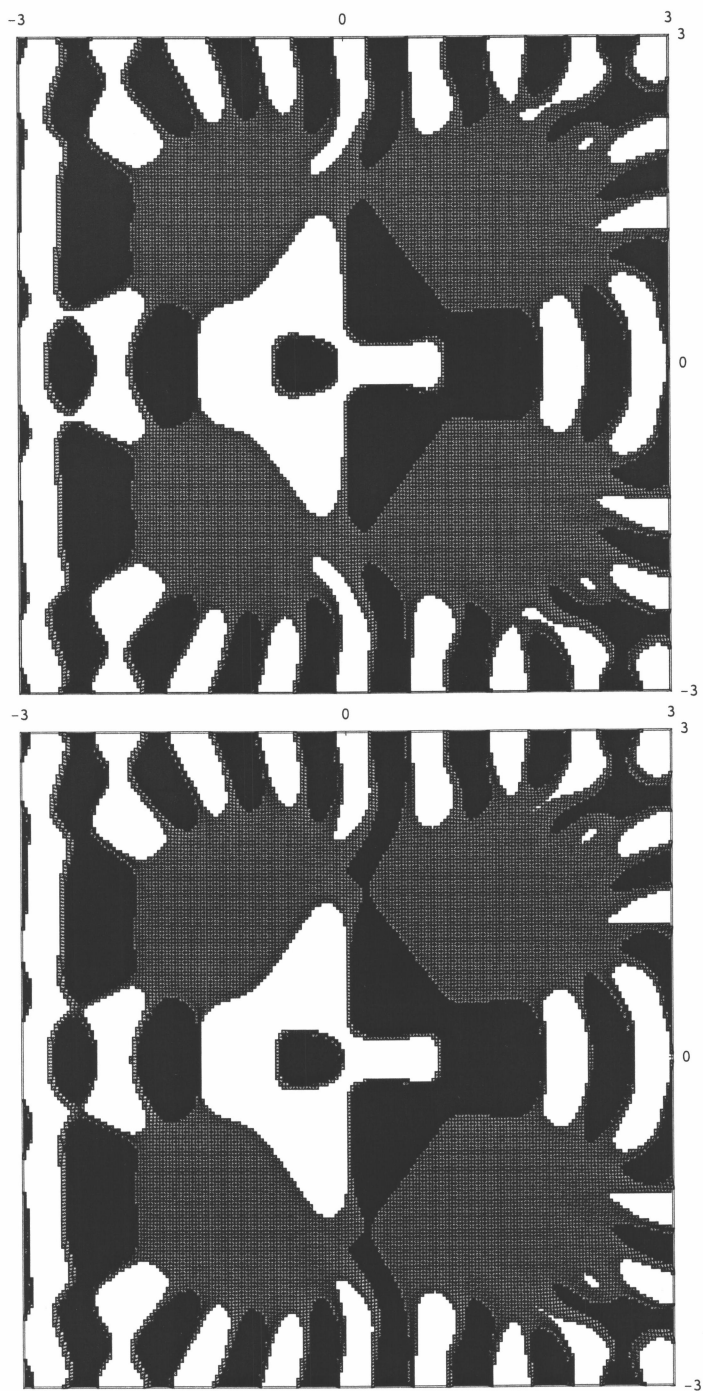


Figure 6.28: Real (top) and rotated (bottom) part of the seventh resonance's clipped wave function showing  $E$  symmetry. Black  $< -0.005 < \text{Gray} < 0.005 < \text{White}$  (top). The incident plane wave is seen to approach from the left.

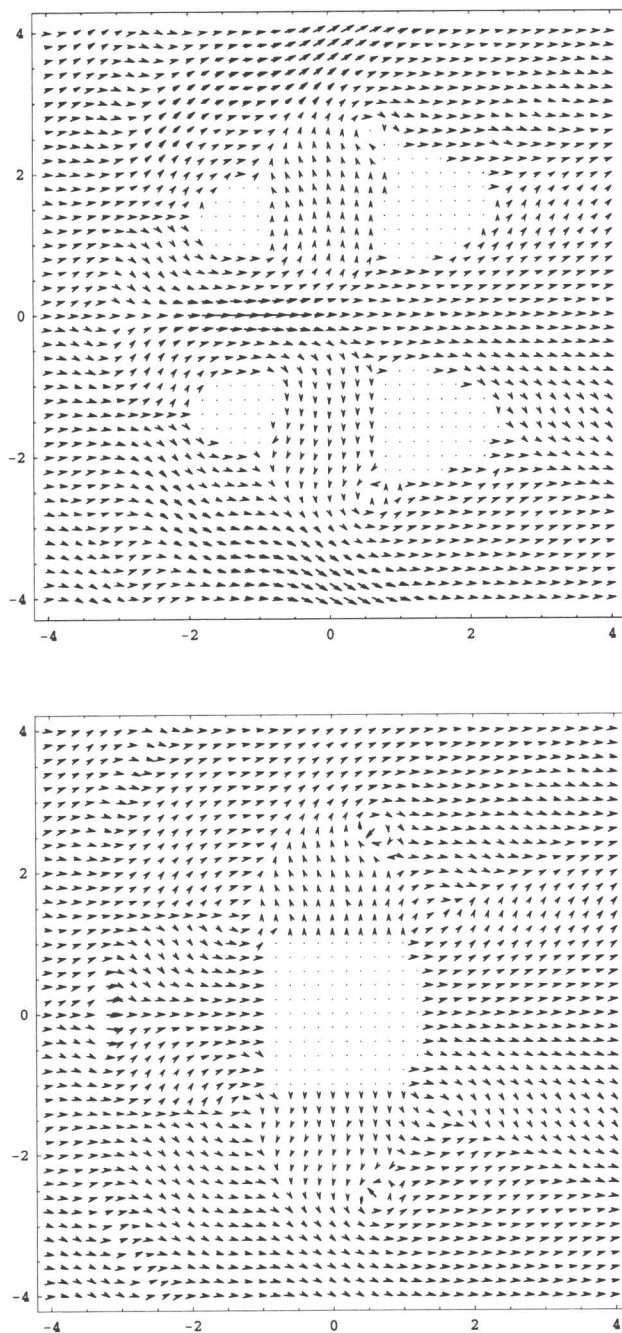


Figure 6.29: Vector fields representing current density (top) and velocity (bottom) of the fundamental resonance calculated from (3.9). Vector lengths are relative, the longest being scaled to the radius of a circle determined by the bases of the nearest neighbors. Any magnitudes below a cutoff threshold of 0.061% (curr.) and 0.257% (vel.) of maximum are indicated by dots.

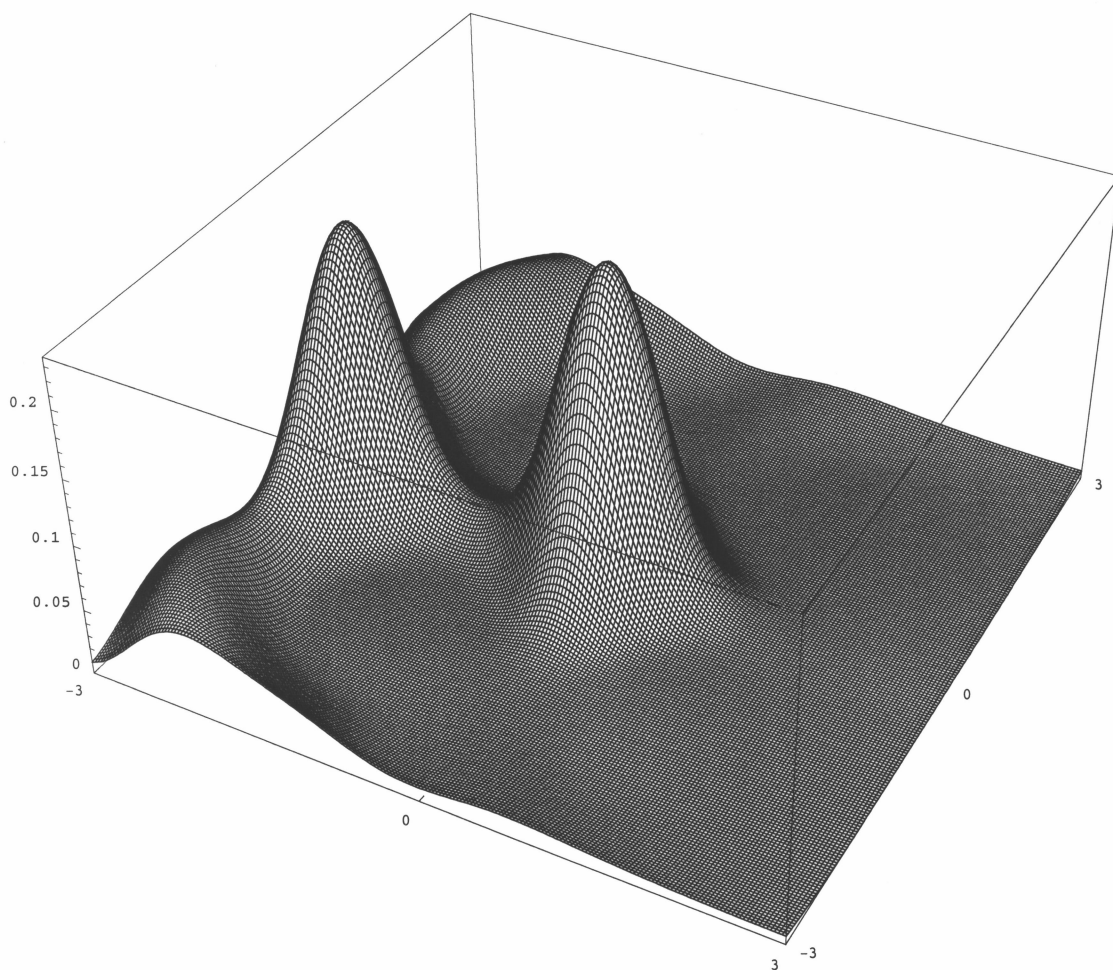


Figure 6.30: Probability density at  $E = 5.43750$ , just below the fundamental resonance of table 6.2.

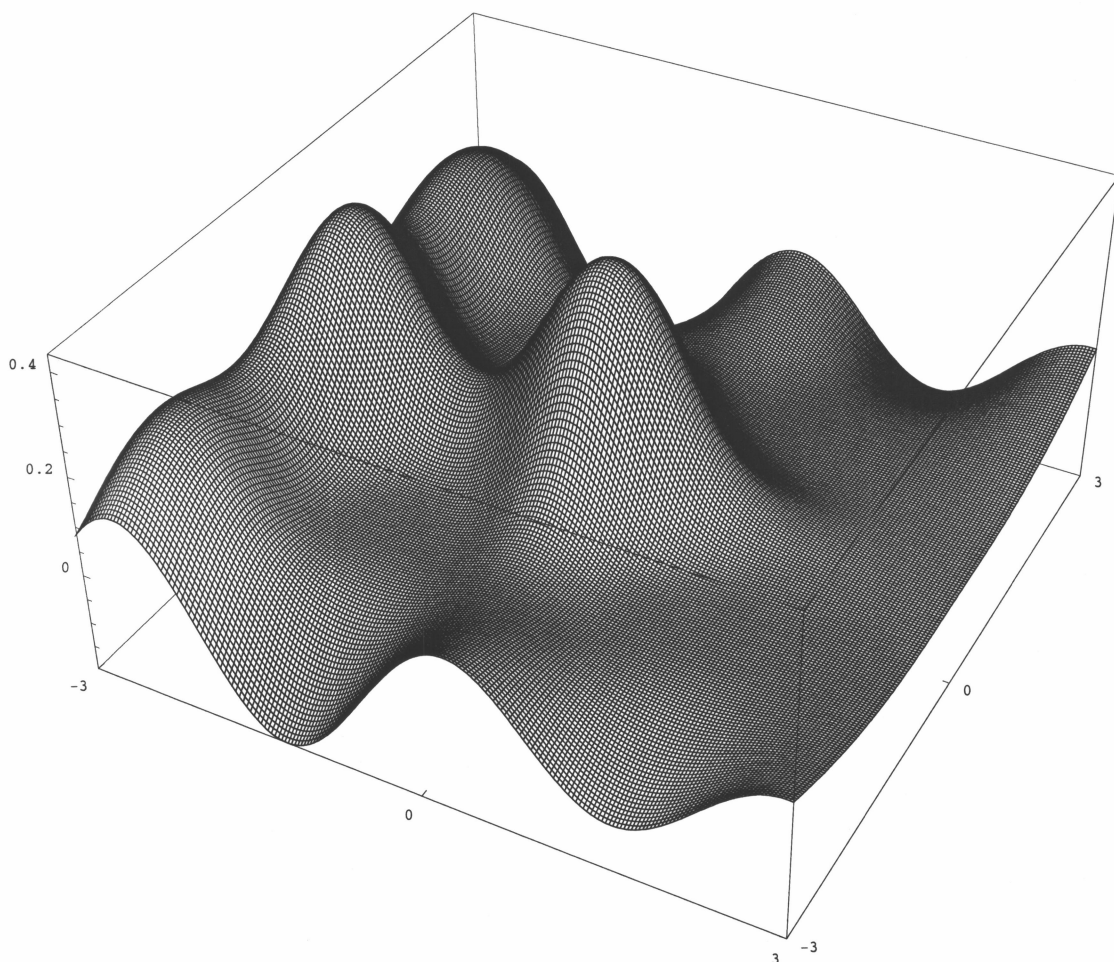


Figure 6.31: Real part of wave function at  $E = 5.43750$ , just below the fundamental resonance of table 6.2, which shows quantum pinching.

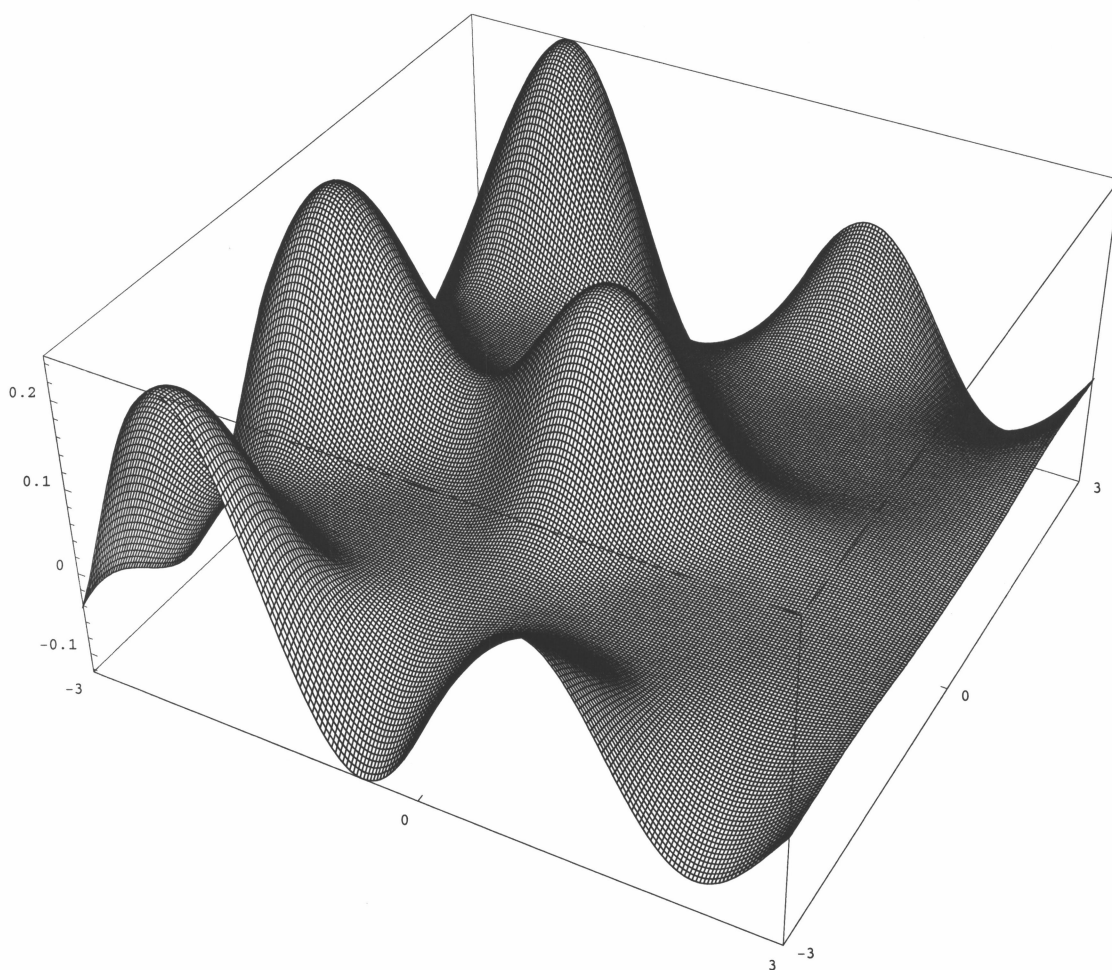


Figure 6.32: Imaginary part of wave function at  $E=5.43750$ , just below the fundamental resonance of table 6.2, which shows quantum pinching.

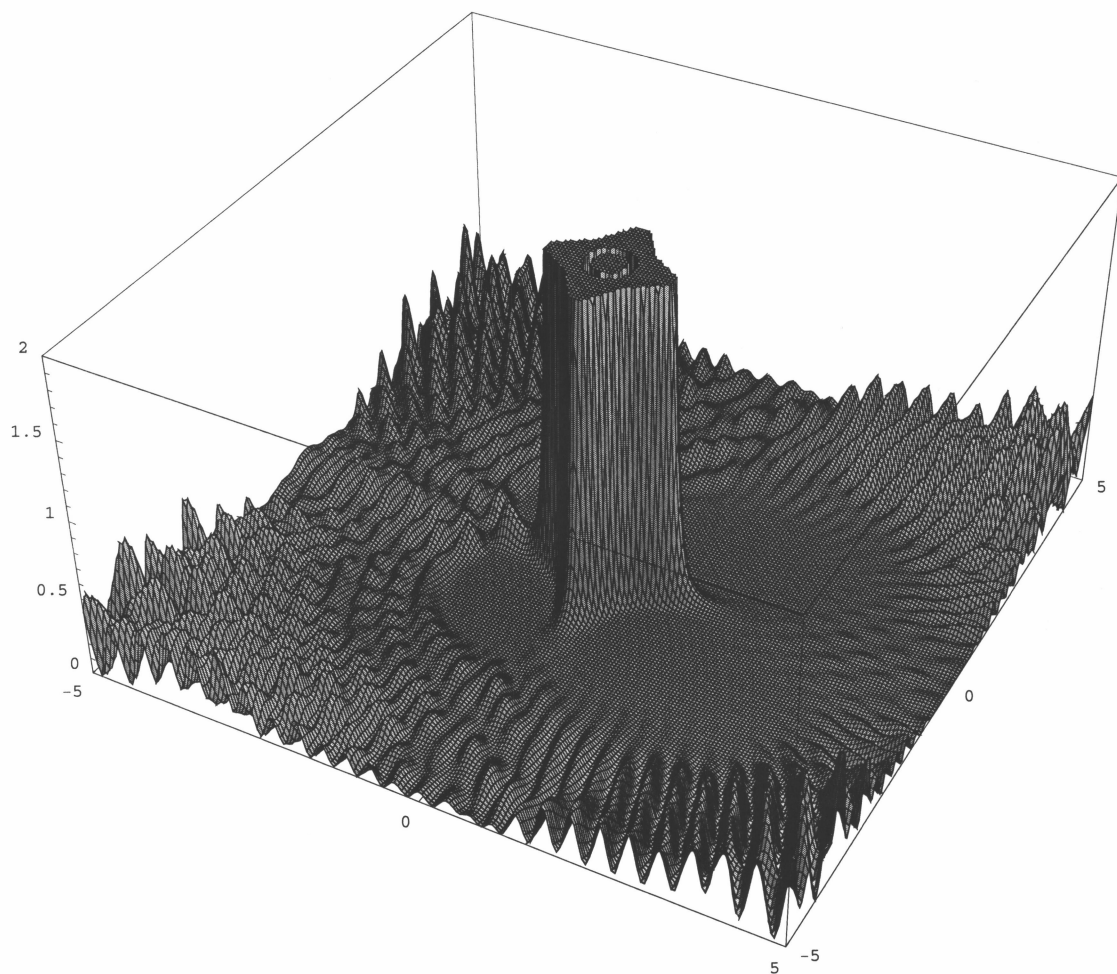


Figure 6.33: Panoramic probability density for the fourth resonance of table 6.2 for which  $V_0 = 1200$ ,  $a = 1.6$  and  $E = 50.9141$  showing complicated interference pattern and the shadow behind the scatterer opposite the incident wave. Truncation of the probability peak here shows the dip in particle densities forming a circular pattern.

## Chapter 7

# Conclusions

Present day manufacturing abilities now include micro-optic and nano-electronic devices. On these length scales, low-mode quantum effects cannot be excluded. A clear understanding is required for wave trapping within potentials that reflect the structure of such devices. The objective of this work has been to contribute to the understanding of the nature of low energy scattering wave functions that result from soft repulsive potentials with broken angular symmetries.

We have demonstrated that the geometry of two-dimensional cage potentials allows long-lived resonances. Such states arise from the transient trapping of quantum particles between the peaks of the potential and correspond classically to multiple reflection. This verifies, for our simple geometry, the interpretations by Peskin *et al.* [32] that transmission maxima correspond to scattering resonances, and that the corresponding localized enhancement in the probability density is due to the local geometry of the scattering centers.

Because of their spatial dependence, soft cage potentials have openings between peaks (the distances between level curves above the saddle points) that broaden with increasing energy. As a result, resonance widths have a strong energy dependence not seen for similar hard potentials that have energy-independent intercolumniation. For hard potentials of this type, there are no resonances in a gap of approximately uniform width below the positive real momentum axis. The width of this band depends not on the energy [26, 27], but on the distance between scattering centers, or more specifically the separation between columns which determines the degree of trapping. For soft potentials, however, we have shown that the width of this gap increases with energy leading to shorter lifetimes for higher-energy resonances.

That specific low-energy resonances with very narrow width correspond to classical multiple-

reflection events is evidenced by much larger probability densities inside the cage than outside, with averaged velocity fields that drop significantly inside the cage as current density actually increases there. These states mimic bound states in the sense that the symmetry-breaking effect of the incident wave is minimal. As a result we have found that these states display the simple symmetry characteristics of bound states.

An example has also been presented in which one of a pair of neighboring resonances has a width that is nearly equal to the interresonance spacing. Under these circumstances the resulting hybridization is shown to cause a mixing of symmetry classes leading to wave functions of lower symmetry, like those exhibited for wider resonances at higher energy.

We have demonstrated that at energies below the lowest resonances of two-dimensional cages, where the distance across the entrance of the cage corresponds to less than half a wavelength, the wave function may still gain access to the interior region by squeezing its wavelength in the necessary direction at the expense of the kinetic energy in the direction normal to the opening. The resulting curvature in the donor dimension corresponds to an imaginary wavenumber, curving away from the  $xy$ -plane. It would be interesting to replace the potentials used for this work with a lattice of repulsive scattering centers to investigate wave function transmission at and off resonance for a geometry that more closely resembles the structure of electronic nanocircuits or photonic crystal fibers.

APPENDICES

## Appendix A

# Solution by Green's Function

Starting with Green's theorem,

$$\int (\Psi(\mathbf{r}') \nabla'^2 G(\mathbf{r}, \mathbf{r}') - G(\mathbf{r}, \mathbf{r}') \nabla'^2 \Psi(\mathbf{r}')) dv' = \oint (\Psi(\mathbf{r}') \nabla' G(\mathbf{r}, \mathbf{r}') - G(\mathbf{r}, \mathbf{r}') \nabla' \Psi(\mathbf{r}')) \cdot \hat{\mathbf{n}} da', \quad (\text{A.1})$$

we show that (3.2) follows from (3.1) by first recasting the time-independent Schrödinger equation into the standard form for the Helmholtz equation,

$$[\nabla^2 + k_o^2] \Psi(\mathbf{r}) = U(\mathbf{r}) \Psi(\mathbf{r}); \quad U = \frac{2\mu V}{\hbar^2}. \quad (\text{A.2})$$

We then assume that a function,  $G_{k_o}(\mathbf{r}, \mathbf{r}')$ , exists which satisfies the nonhomogeneous point source equation with respect to the operator  $\nabla^2 + k_o^2$ ,

$$(\nabla^2 + k_o^2) G_{k_o}(\mathbf{r}, \mathbf{r}') = \delta(\mathbf{r} - \mathbf{r}'). \quad (\text{A.3})$$

and is symmetric with respect to interchange of its arguments. This same operator may be substituted in place of the Laplacians,  $\nabla'^2 \rightarrow \nabla'^2 + k_o^2$ , appearing on the left side of (A.1) to produce an equation,

$$\begin{aligned} \int (\Psi(\mathbf{r}') [\nabla'^2 + k_o^2] G_{k_o}(\mathbf{r}, \mathbf{r}') - G_{k_o}(\mathbf{r}, \mathbf{r}') [\nabla'^2 + k_o^2] \Psi(\mathbf{r}')) dv' \\ = \oint (\Psi(\mathbf{r}') \nabla' G_{k_o}(\mathbf{r}, \mathbf{r}') - G_{k_o}(\mathbf{r}, \mathbf{r}') \nabla' \Psi(\mathbf{r}')) \cdot \hat{\mathbf{n}} da', \quad (\text{A.4}) \end{aligned}$$

in which the two  $k_o$  terms introduced represent a canceling pair.

If we now substitute our assumption (A.3) and the Helmholtz equation (A.2) in (A.4) we obtain

$$\begin{aligned} \int (\Psi(\mathbf{r}') \delta(\mathbf{r} - \mathbf{r}') - G_{k_o}(\mathbf{r}, \mathbf{r}') U(\mathbf{r}') \Psi(\mathbf{r}')) dv' \\ = \oint (\Psi(\mathbf{r}') \nabla' G_{k_o}(\mathbf{r}, \mathbf{r}') - G_{k_o}(\mathbf{r}, \mathbf{r}') \nabla' \Psi(\mathbf{r}')) \cdot \hat{\mathbf{n}} da'. \quad (\text{A.5}) \end{aligned}$$

The surface integral above will vanish if  $\Psi$  and  $G$  both satisfy either Dirichlet or Neumann boundary conditions. Noticing that (A.5) involves only the scattered portion of the asymptotic wave described by (3.26),

$$\lim_{r' \rightarrow \infty} \Psi_{\mathbf{k}_o}^+(\mathbf{r}') = \frac{f_{\mathbf{k}_o}(\theta) e^{ik_o r'}}{2\pi\sqrt{r'}}, \quad (\text{A.6})$$

and that the asymptotic form of the Green's function given by (3.25),

$$G_{\mathbf{k}_o}^+(\mathbf{r}, \mathbf{r}') = \frac{1}{4i} H_o^{(1)}(k_o |\mathbf{r} - \mathbf{r}'|) \rightarrow \frac{e^{i(k_o |\mathbf{r} - \mathbf{r}'| - \pi/4)}}{2i\sqrt{2\pi k_o} |\mathbf{r} - \mathbf{r}'|} \quad : \quad |\mathbf{r} - \mathbf{r}'| \rightarrow \infty, \quad (\text{A.7})$$

will also vanish for large  $r'$ , we extent this integral to infinity by integrating the left hand side over all space. Integrating over the delta function then produces our scattered wave solution in integral form,

$$\Psi_{\mathbf{k}_o}(\mathbf{r}) = \int G_{\mathbf{k}_o}(\mathbf{r}, \mathbf{r}') U(\mathbf{r}') \Psi_{\mathbf{k}_o}(\mathbf{r}') d\mathbf{r}'. \quad (\text{A.8})$$

To obtain a complete solution to our second order differential equation, we form a linear combination of the particular scattered wave solution above with the homogeneous solution,  $\varphi_{\mathbf{k}_o}(\mathbf{r})$ , to (A.2),

$$[\nabla^2 + k_o^2] \varphi_{\mathbf{k}_o}(\mathbf{r}) = 0. \quad (\text{A.9})$$

The homogeneous solution is obtained by turning off the potential and consequently gives us a term equal to the unaltered incident wave. We thus have the general expression for the wave function,

$$\Psi_{\mathbf{k}_o}(\mathbf{r}) = \varphi_{\mathbf{k}_o}(\mathbf{r}) + \int G_{\mathbf{k}_o}(\mathbf{r}, \mathbf{r}') U(\mathbf{r}') \Psi_{\mathbf{k}_o}(\mathbf{r}') d\mathbf{r}', \quad (\text{A.10})$$

which may be written in terms of

$$G_E = \frac{2\mu}{\hbar^2} G_{\mathbf{k}_o}, \quad V = \frac{\hbar^2}{2\mu} U, \quad (\text{A.11})$$

as

$$\Psi_{\mathbf{k}_o}(\mathbf{r}) = \varphi_{\mathbf{k}_o}(\mathbf{r}) + \int G_E(\mathbf{r}, \mathbf{r}') V(\mathbf{r}') \Psi_{\mathbf{k}_o}(\mathbf{r}') d\mathbf{r}', \quad (\text{A.12})$$

consistent with (3.2).

We conclude this appendix by mentioning that alternate forms of the assumed point source equation (A.3) are frequently used in the literature. The three most common occurrences are as follows:

$$(\nabla^2 + k_o^2) G_{\mathbf{k}_o}(\mathbf{r}, \mathbf{r}') = \begin{cases} \delta(\mathbf{r} - \mathbf{r}') & : \text{Case I} \\ -\delta(\mathbf{r} - \mathbf{r}') & : \text{Case II} \\ -4\pi\delta(\mathbf{r} - \mathbf{r}') & : \text{Case III.} \end{cases} \quad (\text{A.13})$$

The representations of the Green's functions from the different cases differ only by the corresponding constant factor multiplying the delta functions above.

## Appendix B

# Scattering Amplitude Particulars

This appendix provides details for the derivation of the scattering amplitude given by (3.27) from the equation

$$\Psi_{\mathbf{k}_o}^+(\mathbf{r}) = \varphi_{\mathbf{k}_o}(\mathbf{r}) + \int G_E^+(\mathbf{r}, \mathbf{r}') V(\mathbf{r}') \Psi_{\mathbf{k}_o}^+(\mathbf{r}') d\mathbf{r}', \quad (\text{B.1})$$

which follows from (3.2), and the Green's function for two-dimensional space given by (3.25),

$$G_{k_o}^+(\mathbf{r}, \mathbf{r}') = \frac{e^{i(k_o|\mathbf{r}-\mathbf{r}'|-\pi/4)}}{2i\sqrt{2\pi k_o|\mathbf{r}-\mathbf{r}'|}}; \quad |\mathbf{r}-\mathbf{r}'| \rightarrow \infty. \quad (\text{B.2})$$

Using the fact that  $G_E^+ = 2\mu G_{k_o}^+/\hbar^2$ , (B.1) and (B.2) are combined to produce

$$\Psi_{\mathbf{k}_o}^+(\mathbf{r}) = \varphi_{\mathbf{k}_o}(\mathbf{r}) + \frac{2\mu}{\hbar^2} \int \frac{e^{i(k_o|\mathbf{r}-\mathbf{r}'|-\pi/4)}}{2i\sqrt{2\pi k_o|\mathbf{r}-\mathbf{r}'|}} V(\mathbf{r}') \Psi_{\mathbf{k}_o}^+(\mathbf{r}') d\mathbf{r}'. \quad (\text{B.3})$$

We approximate  $|\mathbf{r}-\mathbf{r}'|$  by expanding it as a power series in  $\mathbf{r}'$ ,

$$|\mathbf{r}-\mathbf{r}'| = \sqrt{r^2 - 2\mathbf{r}\cdot\mathbf{r}' + r'^2} = r - \frac{\mathbf{r}\cdot\mathbf{r}'}{r} + \frac{|\mathbf{r}\times\mathbf{r}'|^2}{2r^3} + \frac{(\mathbf{r}\cdot\mathbf{r}')|\mathbf{r}\times\mathbf{r}'|^2}{2r^5} + \dots, \quad (\text{B.4})$$

and considering a field point,  $\mathbf{r}$ , located a large distance from a local scattering center given by  $\mathbf{r}'$  as shown in figure B.1. Also shown is the incident momentum,  $\mathbf{k}_o$ , being scattered at  $\mathbf{r}'$  toward the field point,  $\mathbf{r}$ . The scattering is taken to be elastic so the scattered momentum  $\mathbf{k}$  has the same magnitude as the incident momentum,  $k^2 = k_o^2$ , and the new direction defines the scattering angle  $\theta$  between these two vectors. If the effective range of the scatterer is limited so that only small values of  $r'$  contribute to the integral (B.3) while  $r \gg r'$ , then higher order terms in  $\mathbf{r}'$  from the expansion (B.4) may be discarded from our approximations. Taking the first two terms of the series allows us to write the exponential appearing in (B.3) as

$$e^{i(k_o|\mathbf{r}-\mathbf{r}'|-\pi/4)} \approx e^{ik_o r} e^{-i\mathbf{k}_o\cdot\mathbf{r}'} e^{-i\pi/4}. \quad (\text{B.5})$$

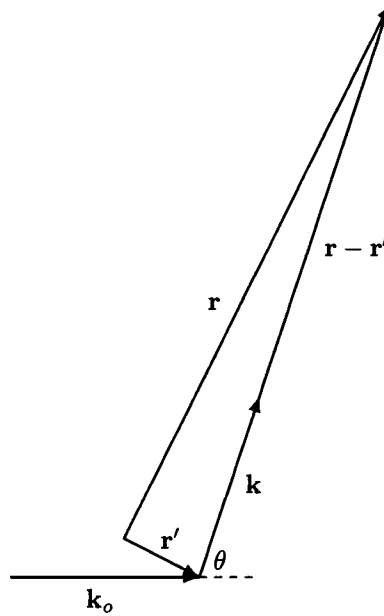


Figure B.1: Relationship between the vectors used.

As is evident from figure B.1, if  $r$  is taken to be asymptotically distant from the localized scattering region then the direction of the scattered wave,  $(\mathbf{r} - \mathbf{r}')$ , may be taken to lie along  $\mathbf{r}$  consistent with considering only the first term in the expansion so that  $|\mathbf{r} - \mathbf{r}'| \approx r$ . We apply this first term to the denominator of (B.3) and the second exponential appearing on the right hand side of (B.5), which determines the numerator, and write

$$\Psi_{\mathbf{k}_o}^+(\mathbf{r}) = \varphi_{\mathbf{k}_o}(\mathbf{r}) + \frac{2\mu}{\hbar^2} \int \frac{e^{ik_o r} e^{-i\pi/4} e^{-i\mathbf{k} \cdot \mathbf{r}'}}{2i\sqrt{2\pi k_o r}} V(\mathbf{r}') \Psi_{\mathbf{k}_o}^+(\mathbf{r}') d\mathbf{r}', \quad (\text{B.6})$$

where  $r'/r \rightarrow 0$  leads to the equality. The constants are moved outside the integration and the approximated exponential is written as  $\varphi_{\mathbf{k}}^*(\mathbf{r}')$  so that the resulting equation,

$$\Psi_{\mathbf{k}_o}^+(\mathbf{r}) = \varphi_{\mathbf{k}_o}(\mathbf{r}) + \frac{\mu}{i\hbar^2} \sqrt{\frac{2\pi}{k_o r}} \int e^{ik_o r} e^{-i\pi/4} \varphi_{\mathbf{k}}^*(\mathbf{r}') V(\mathbf{r}') \Psi_{\mathbf{k}_o}^+(\mathbf{r}') d\mathbf{r}', \quad (\text{B.7})$$

may be expressed in terms of the transition matrix.

Recognizing that  $\mathbf{T}$ , given by (3.3),

$$\int \varphi_{\mathbf{k}}^*(\mathbf{r}') V(\mathbf{r}') \Psi_{\mathbf{k}_o}^+(\mathbf{r}') d^2 r' = \langle \varphi_{\mathbf{k}}^* | V | \Psi_{\mathbf{k}_o}^+ \rangle \equiv T_{\mathbf{k}\mathbf{k}_o}, \quad (\text{B.8})$$

now appears explicitly in (B.7) allows us to write

$$\Psi_{\mathbf{k}_o}^+(\mathbf{r}) = \varphi_{\mathbf{k}_o}(\mathbf{r}) + \frac{\mu}{i\hbar^2} \sqrt{\frac{2\pi}{k_o r}} e^{ik_o r} e^{-i\pi/4} T_{\mathbf{k}\mathbf{k}_o}. \quad (\text{B.9})$$

We may now recast the additional phase factor,

$$e^{-i\pi/4} = \cos\left(\frac{\pi}{4}\right) - i \sin\left(\frac{\pi}{4}\right) = \frac{\sqrt{2}}{2}(1 - i), \quad (\text{B.10})$$

where upon substitution into (B.9) we are left with

$$\Psi_{\mathbf{k}_o}^+(\mathbf{r}) = \varphi_{\mathbf{k}_o}(\mathbf{r}) - \frac{i\mu}{\hbar^2} \sqrt{\frac{\pi}{k_o r}} (1 - i) e^{ik_o r} T_{\mathbf{k}\mathbf{k}_o}. \quad (\text{B.11})$$

Distributing  $i$  gives us a cleaner expression,

$$\Psi_{\mathbf{k}_o}^+(\mathbf{r}) = \varphi_{\mathbf{k}_o}(\mathbf{r}) - \frac{\mu}{\hbar^2} \sqrt{\frac{\pi}{k_o r}} (1 + i) e^{ik_o r} T_{\mathbf{k}\mathbf{k}_o}, \quad (\text{B.12})$$

that when compared to the asymptotic form of the scattered wave given by (3.26),

$$\lim_{r \rightarrow \infty} \Psi_{\mathbf{k}_o}^+(\mathbf{r}) = \varphi_{\mathbf{k}_o}(\mathbf{r}) + \frac{f_{k_o}(\theta) e^{ik_o r}}{2\pi\sqrt{r}}, \quad (\text{B.13})$$

reveals the form of the scattering amplitude that appears in equation (3.27),

$$f_{k_o}(\theta) = -\frac{2\pi\mu}{\hbar^2} \sqrt{\frac{\pi}{k_o}} (1 + i) T_{\mathbf{k}\mathbf{k}_o}. \quad (\text{B.14})$$

## Appendix C

# Scattering Amplitude Dependence of 2-D Differential Cross Sections

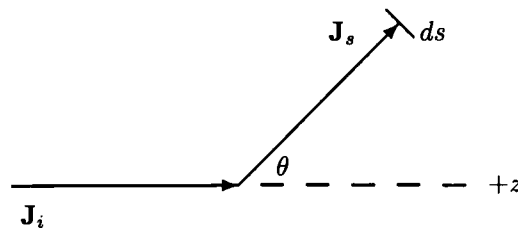


Figure C.1: Relationship between incident and scattered current densities.

From figure C.1 we see that the number of scattered particles per unit time passing through a length of arc  $ds$  is proportional to the incident current density,

$$\frac{dN}{dt} = \mathbf{J}_s \cdot ds \propto \mathbf{J}_i. \quad (\text{C.1})$$

Letting  $d\lambda$  represent the constant of proportionality,

$$\mathbf{J}_s \cdot ds = d\lambda \mathbf{J}_i, \quad (\text{C.2})$$

we may express it in terms of the angle,  $d\theta$ , subtended by the arc length,

$$d\lambda = ds \frac{J_s}{J_i} = r d\theta \frac{J_s}{J_i}. \quad (\text{C.3})$$

The incident and scattered current densities are found by applying the expression for current density,

$$\mathbf{J}(\mathbf{r}) = \frac{\hbar}{2\mu i} [\Psi^*(\mathbf{r})\nabla\Psi(\mathbf{r}) - \Psi(\mathbf{r})\nabla\Psi^*(\mathbf{r})], \quad (\text{C.4})$$

to the incident and scattered parts of the wave as given by the 2-D equation (3.26),

$$\Psi_{\mathbf{k}_o}^+(\mathbf{r}) = \varphi_i(\mathbf{r}) + \varphi_s(\mathbf{r}) = \frac{e^{ik_o z}}{2\pi} + \frac{f_{k_o}(\theta)e^{ik_o r}}{2\pi\sqrt{r}}. \quad (\text{C.5})$$

Since the scattered wave propagates radially at asymptotic distances from the scatterer, only that component of the gradient survives,

$$J_s(\mathbf{r}) = \frac{\hbar}{8\pi^2\mu i} \left[ \frac{f_{k_o}^*(\theta)e^{-ik_o r}}{\sqrt{r}} \frac{\partial}{\partial r} \frac{f_{k_o}(\theta)e^{ik_o r}}{\sqrt{r}} - \frac{f_{k_o}(\theta)e^{ik_o r}}{\sqrt{r}} \frac{\partial}{\partial r} \frac{f_{k_o}^*(\theta)e^{-ik_o r}}{\sqrt{r}} \right] = \frac{|f_{k_o}(\theta)|^2 \hbar k}{4\pi^2\mu r}. \quad (\text{C.6})$$

Having chosen the unit vector  $\hat{\mathbf{z}}$  to coincide with the direction of travel for the incident wave in (C.5), the magnitude of the incident current density is found to be

$$J_i = \frac{\hbar}{8\pi^2\mu i} \left[ e^{-ik_o z} \frac{\partial}{\partial z} e^{ik_o z} - e^{ik_o z} \frac{\partial}{\partial z} e^{-ik_o z} \right] = \frac{\hbar k}{4\pi^2\mu}. \quad (\text{C.7})$$

Substituting the right hand sides of (C.6) and (C.7) back into equation (C.3) reveals the dependence of the two-dimensional differential cross section on the scattering amplitude,

$$\frac{d\lambda}{d\theta} = |f_{k_o}(\theta)|^2. \quad (\text{C.8})$$

As is clearly evident from equation (C.3), the cross section here actually has units of length. The quantities  $r$  and  $J_s$  in the same formula vary inversely in such a way that their product remains fixed.

## Appendix D

# Two-Dimensional Partial Wave

## Basis

Although the code was specifically designed for calculations with noncentral potentials, its modular form allows for the insertion of central potentials as well. Since the technique we employ is unbiased toward either type of potential we are afforded the opportunity to test the code against a two-dimensional partial wave method.

### Scattering Amplitude Expansion

Since for a central potential the angular momentum operator commutes with the Hamiltonian,  $[L, H]=0$ , the wave function may be expanded in simultaneous eigenfunctions of both operators. In two dimensions the scattering amplitude takes on a slightly different form so we will briefly sketch its derivation. We start by finding the spatial representation of the angular momentum operators:

$$L = R \times P = xP_y - yP_x = -i\hbar \left( x \frac{\partial}{\partial y} - y \frac{\partial}{\partial x} \right) = L_z. \quad (\text{D.1})$$

Expressing terms in polar form:

$$\begin{aligned} x = r \cos \theta & \quad \frac{\partial}{\partial x} = \cos \theta \frac{\partial}{\partial r} - \frac{\sin \theta}{r} \frac{\partial}{\partial \theta} \\ y = r \sin \theta & \quad \frac{\partial}{\partial y} = \sin \theta \frac{\partial}{\partial r} + \frac{\cos \theta}{r} \frac{\partial}{\partial \theta}, \end{aligned} \quad (\text{D.2})$$

we substitute into (D.1) to find:

$$L_z = -i\hbar \frac{\partial}{\partial \theta}, \quad L^2 = -\hbar^2 \frac{\partial^2}{\partial \theta^2}. \quad (\text{D.3})$$

The easiest way to get the partial derivatives given in (D.2) is to equate the gradients:

$$\nabla_{xy} = \nabla_{r\theta} \Rightarrow \hat{x} \frac{\partial}{\partial x} + \hat{y} \frac{\partial}{\partial y} = \hat{r} \frac{\partial}{\partial r} + \hat{\theta} \frac{1}{r} \frac{\partial}{\partial \theta}, \quad (\text{D.4})$$

and find the components of the  $\hat{r}$  and  $\hat{\theta}$  unit vectors in the  $\hat{x}$  and  $\hat{y}$  directions:

$$\begin{aligned} \hat{r} &= \cos \theta \hat{x} + \sin \theta \hat{y} \\ \hat{\theta} &= -\sin \theta \hat{x} + \cos \theta \hat{y}. \end{aligned} \quad (\text{D.5})$$

We focus now on the solution to Schrödinger's equation,

$$\left[ -\frac{\hbar^2}{2\mu} \nabla^2 + V(\mathbf{r}) \right] \Psi(\mathbf{r}) = E \Psi(\mathbf{r}), \quad (\text{D.6})$$

for both a free particle and one subject to a central potential. Letting  $V=0$  and substituting the Laplacian

$$\nabla^2 = \frac{1}{r} \frac{\partial}{\partial r} \left( r \frac{\partial}{\partial r} \right) + \frac{1}{r^2} \frac{\partial^2}{\partial \theta^2} \quad (\text{D.7})$$

into (D.6) gives

$$\left[ -\frac{\hbar^2}{2\mu r} \frac{\partial}{\partial r} \left( r \frac{\partial}{\partial r} \right) + \frac{L^2}{2\mu r^2} \right] R(r)\Theta(\theta) = E R(r)\Theta(\theta), \quad (\text{D.8})$$

where we have assumed a separable solution. Letting  $L^2$  act on  $\Psi(\mathbf{r}) = R(r)\Theta(\theta)$  we find the normalized eigenfunction to be

$$\Theta(\theta) = \frac{e^{im\theta}}{\sqrt{2\pi}} \quad (\text{D.9})$$

with a corresponding eigenvalue

$$L^2 \Theta(\theta) = m^2 \hbar^2 \Theta(\theta), \quad (\text{D.10})$$

normalized so that

$$\frac{1}{2\pi} \int_0^{2\pi} e^{-im\theta} e^{im'\theta} d\theta = \delta_{mm'}. \quad (\text{D.11})$$

Substituting into (D.8) and dividing out the angular dependence, we are left with Bessel's equation,

$$\left[ -\frac{1}{r} \frac{d}{dr} \left( r \frac{d}{dr} \right) + \frac{m^2}{r^2} \right] R(r) = k^2 R(r), \quad (\text{D.12})$$

the solution to which is well known. As our differential equation is of second order, the complete solution is a linear combination of two linearly independent functions. These are the Bessel and Neumann functions, sometimes referred to simply as Bessel functions of the first and second kind. Being irregular at the origin, the Neumann function is excluded from the wave function of a free particle, so that

$$R_{km}(r) = \sqrt{k} J_m(kr); \quad k \int_0^\infty J_m(kr) J_m(k'r) r dr = \delta(k - k'). \quad (\text{D.13})$$

Including the central potential, we have

$$\left[ -\frac{1}{r} \frac{d}{dr} \left( r \frac{d}{dr} \right) + \frac{m^2}{r^2} + U(r) \right] R(r) = k^2 R(r). \quad (\text{D.14})$$

We are careful to choose a potential whose influence is felt only locally and drops quickly for increasing radial distance. This way (D.14) will reduce to (D.12) for large  $r$  and the asymptotic solution must be a linear combination of both Bessel and Neumann functions:

$$J_m(kr) \xrightarrow{kr \rightarrow \infty} J_m(kr \rightarrow \infty) = \sqrt{\frac{2}{\pi kr}} \cos \left[ kr - \frac{\pi}{2} \left( m + \frac{1}{2} \right) \right], \quad (\text{D.15})$$

$$N_m(kr) \xrightarrow{kr \rightarrow \infty} N_m(kr \rightarrow \infty) = \sqrt{\frac{2}{\pi kr}} \sin \left[ kr - \frac{\pi}{2} \left( m + \frac{1}{2} \right) \right]. \quad (\text{D.16})$$

Mathematically we are allowed to exchange the two linear coefficients for an amplitude and phase angle,

$$\begin{aligned} A J_m(kr \rightarrow \infty) + B N_m(kr \rightarrow \infty) &= C \sqrt{\frac{2}{\pi kr}} \cos \left[ kr - \frac{\pi}{2} \left( m + \frac{1}{2} \right) + \delta_m \right] \\ &= R_{km}(r \rightarrow \infty) / \sqrt{k}, \end{aligned} \quad (\text{D.17})$$

where  $C$  is fixed by normalization criteria. In general a closed form solution in the region of the potential will not be known, but if the potential is well behaved, we expect that the wave function in the transitional region will be both continuous and smooth. If we compare the free particle solution to one asymptotically distant from a central potential we see that (D.17) will differ from (D.15) in its phase,  $\delta_m$ . It is these changes in phase, one for each angular momentum quantum number  $m$ , that carry all the information necessary to deduce the scattering amplitude for a given energy.

To explicitly show the dependence of the scattering amplitude on the phase shifts, we take the asymptotic solution in the presence of a potential, given by (D.17) with  $C$  set to unity, and express it in complex form using the fact that  $\sin(\theta + \pi/2) = \cos(\theta)$ ,

$$\frac{R_{km}(r \rightarrow \infty)}{\sqrt{k}} = \frac{1}{2i} \sqrt{\frac{2}{\pi kr}} \left[ e^{i(kr - m\pi/2 + \pi/4 + \delta_m)} - e^{-i(kr - m\pi/2 + \pi/4 + \delta_m)} \right]. \quad (\text{D.18})$$

A new partial wave is defined by forming the product with a global phase factor,  $e^{i\delta_m}$ , that has no physical bearing:

$$\frac{R_{km}(r \rightarrow \infty)}{\sqrt{k}} = \frac{1}{2i} \sqrt{\frac{2}{\pi kr}} \left[ e^{i(kr - m\pi/2 + \pi/4)} e^{i2\delta_m} - e^{-i(kr - m\pi/2 + \pi/4)} \right]. \quad (\text{D.19})$$

We pause to compare the previous expression to the asymptotic form of the free particle solution (D.15) when expressed first as a sine, by advancing the argument  $\pi/2$  radians, and then in complex form. Evidently the outwardly travelling wave is shifted in phase by  $2\delta_m$  relative to the unperturbed

wave propagating inward toward the potential's region of influence. We continue by employing the identity

$$e^{i2\delta_m} = 1 + e^{i2\delta_m} - 1 = 1 + 2ie^{i\delta_m} \frac{e^{i\delta_m} - e^{-i\delta_m}}{2i} = 1 + 2ie^{i\delta_m} \sin \delta_m, \quad (\text{D.20})$$

so that (D.19) takes the form

$$\begin{aligned} & \frac{R_{km}(r \rightarrow \infty)}{\sqrt{k}} \\ &= \frac{1}{2i} \sqrt{\frac{2}{\pi kr}} \left[ e^{i(kr - m\pi/2 + \pi/4)} - e^{-i(kr - m\pi/2 + \pi/4)} + e^{i(kr - m\pi/2 + \pi/4)} 2ie^{i\delta_m} \sin \delta_m \right], \end{aligned} \quad (\text{D.21})$$

which may be expressed as the free-wave Bessel solution plus an additional term,

$$\sqrt{\frac{2}{\pi kr}} \cos \left[ kr - \frac{\pi}{2} \left( m + \frac{1}{2} \right) + \delta_m \right] = J_m(kr \rightarrow \infty) + \sqrt{\frac{2}{\pi kr}} e^{i\delta_m} \sin \delta_m e^{ikr} e^{-im\pi/2} e^{i\pi/4}, \quad (\text{D.22})$$

where we have used the notation established in the first line of (D.15). We now introduce a plane wave expansion in terms of Bessel functions [43],

$$e^{ikx} = \sum_{m=0}^{\infty} \nu_m i^m \cos(m\theta) J_m(kr). \quad (\text{D.23})$$

The parameter  $\nu_m$ , defined as 1 only for  $m=0$  and 2 otherwise, is introduced so that the expansion may be written to involve only positive  $m$ . This expansion gives us a clue to the coefficients required when the potential is acting. Remember that in the absence of a potential our solution takes the form of a superposition of Bessel functions of all orders (D.23) representing a plane wave that will continue to propagate unaltered. With the potential present, we expect an additional scattering term. This additional term is the second one appearing on the left hand side of (D.24). We will relate this scattering term directly to the sum over  $m$  of the second terms appearing on the right hand side of (D.22). We assert now that the correct coefficients for this sum will be identically the same as those used for the plane wave expansion (D.23) for the no-potential case, giving us

$$e^{ikx} + \frac{f(\theta)e^{ikr}}{\sqrt{r}} = \sum_{m=0}^{\infty} \nu_m i^m \cos(m\theta) \left[ J_m(kr \rightarrow \infty) + \sqrt{\frac{2}{\pi kr}} e^{i\delta_m} \sin \delta_m e^{ikr} e^{-im\pi/2} e^{i\pi/4} \right]. \quad (\text{D.24})$$

Justification comes from the fact that if the potential is adiabatically turned off, then the sum of (D.22) over  $m$  must degenerate into (D.23). The second additional scattering term will drop out because the phase shifts,  $\delta_m$ , will all tend toward zero, giving us the desired limiting behavior. Using the fact that

$$i^m = \left( e^{i\pi/2} \right)^m = e^{im\pi/2}, \quad (\text{D.25})$$

the  $e^{-im\pi/2}$  term is canceled from the right side of (D.24), leaving behind the correct form of the two-dimensional scattering amplitude,

$$f(\theta) = \sqrt{\frac{2}{\pi k}} e^{i\pi/4} \sum_{m=0}^{\infty} \nu_m \cos(m\theta) e^{i\delta_m} \sin \delta_m. \quad (\text{D.26})$$

### Calculating Phase Shifts

To actually calculate phase shifts for a given central potential, the numerical differential equation solver, `NDSolve`, packaged with *Mathematica*<sup>®</sup> was used. After deciding on a particular mass,  $\mu$ , and energy,  $E$ , the `NDSolve` command is evoked twice for each angular momentum quantum number,  $m$ . Using the proper Cauchy boundary conditions at  $r=0$ , our solutions with (D.14) and without (D.12) the potential are extrapolated radially outward until the effect of the potential in (D.14) is negligible. The  $n^{\text{th}}$  intersection with the abscissa is chosen as a reference and the difference in the radial coordinate,  $\Delta r$ , of where these two plots cross the abscissa is determined. From these data the phase shifts are quickly resolved,

$$\delta_m = 2\pi \frac{\Delta r_m}{\lambda} = k\Delta r_m. \quad (\text{D.27})$$

These phase shifts are then plugged back into (D.26) so that we may obtain the scattering amplitude and ultimately the differential scattering cross section (see appendix C),

$$\frac{\partial \lambda}{\partial \theta} = |f(\theta)|^2. \quad (\text{D.28})$$

The actual phase shifts used to calculate the solid dots pictured in the upper and lower plots of figure 5.4 are tabulated in D.1 and D.2 respectively. The negative values indicate the repulsive potential expelling the partial waves from the origin.

$m$	$\delta_m$ (radians)
0	-2.98749548
1	-1.79689945
2	-1.04183076
3	-.55316603
4	-.25740429
5	-.10193870
6	-.03372200
7	-.00955088
8	-.00233155
9	-.00051425
10	-.00010066
11	-.00001797
12	-.00000306

Table D.1: Phase shifts obtained and used in the generation of the top plot of figure 5.4.

$m$	$\delta_m$ (radians)	$m$	$\delta_m$ (radians)
0	-3.01024329	25	-.07708983
1	-4.66892510	26	-.05287917
2	-3.35447563	27	-.035773788
3	-2.19097700	28	-.02372604
4	-1.15785964	29	-.01548241
5	-.23629731	30	-.00998570
6	-5.70630729	31	-.00631711
7	-4.97002059	32	-.00395613
8	-4.30806958	33	-.00242980
9	-3.71484504	34	-.00147097
10	-3.18211529	35	-.00088324
11	-2.70725008	36	-.00051990
12	-2.28350993	37	-.00030182
13	-1.90978181	38	-.00017410
14	-1.58011677	39	-.00009837
15	-1.29396571	40	-.00005531
16	-1.04584009	41	-.00003043
17	-.83409322	42	-.00001652
18	-.65658359	43	-.00000895
19	-.50836068	44	-.00000473
20	-.38791781	45	-.00000247
21	-.29058729	46	-.00000129
22	-.21436158	47	-.00000066
23	-.15504016	48	-.00000033
24	-.11015089	49	-.00000016

Table D.2: Phase shifts obtained and used in the generation of the bottom plot of figure 5.4.

## Appendix E

# Momentum Space Representation of the $D_3$ Potential

Beginning with the coordinate representation of the  $D_3$  scatterer given by (5.1),

$$\begin{aligned}
 V(\mathbf{r}) = & \frac{V_0}{\exp\left(\left[a\left(x - \frac{R}{\sqrt{3}}\right)\right]^2 + [ay]^2\right)} \\
 & + \frac{V_0}{\exp\left(\left[a\left(x + \frac{R}{2\sqrt{3}}\right)\right]^2 + \left[a\left(y - \frac{R}{2}\right)\right]^2\right)} + \frac{V_0}{\exp\left(\left[a\left(x + \frac{R}{2\sqrt{3}}\right)\right]^2 + \left[a\left(y + \frac{R}{2}\right)\right]^2\right)}, \quad (\text{E.1})
 \end{aligned}$$

we use the following notation

$$\begin{aligned}
 \mathbf{r} &= x \hat{\mathbf{x}} + y \hat{\mathbf{y}} \\
 \mathbf{k}' &= k'_x \hat{\mathbf{x}} + k'_y \hat{\mathbf{y}} \\
 \mathbf{k} &= k_x \hat{\mathbf{x}} + k_y \hat{\mathbf{y}} \\
 \mathbf{r} \cdot (\mathbf{k}' - \mathbf{k}) &= x(k'_x - k_x) + y(k'_y - k_y) \quad (\text{E.2})
 \end{aligned}$$

to deduce the needed momentum space representation used in (3.18) and (3.22),

$$V(\mathbf{k}, \mathbf{k}') \equiv \langle \varphi_{\mathbf{k}} | V | \varphi_{\mathbf{k}'} \rangle \equiv \langle \mathbf{k} | V | \mathbf{k}' \rangle. \quad (\text{E.3})$$

Expanding the explicit form of the previous equation,

$$\int \frac{e^{-i\mathbf{k}\cdot\mathbf{r}}}{2\pi} V(\mathbf{r}) \frac{e^{i\mathbf{k}'\cdot\mathbf{r}}}{2\pi} d^2r, \quad (\text{E.4})$$

produces

$$\begin{aligned}
V(\mathbf{r}) &= \frac{V_o}{4\pi^2} \iint \frac{e^{i\mathbf{r}\cdot(\mathbf{k}'-\mathbf{k})}}{\exp\left(\left[a\left(x-\frac{R}{\sqrt{3}}\right)\right]^2 + [ay]^2\right)} dx dy \\
&+ \frac{V_o}{4\pi^2} \iint \frac{e^{i\mathbf{r}\cdot(\mathbf{k}'-\mathbf{k})}}{\exp\left(\left[a\left(x+\frac{R}{2\sqrt{3}}\right)\right]^2 + \left[a\left(y-\frac{R}{2}\right)\right]^2\right)} dx dy \\
&+ \frac{V_o}{4\pi^2} \iint \frac{e^{i\mathbf{r}\cdot(\mathbf{k}'-\mathbf{k})}}{\exp\left(\left[a\left(x+\frac{R}{2\sqrt{3}}\right)\right]^2 + \left[a\left(y+\frac{R}{2}\right)\right]^2\right)} dx dy. \tag{E.5}
\end{aligned}$$

Because all limits of integration extend to infinity, the integrals given above factorize. We use (E.2) together with the fact that the exponential of a sum is the product of exponentials to write

$$\begin{aligned}
V(\mathbf{r}) &= \frac{V_o}{4\pi^2} \int_{-\infty}^{\infty} \frac{\cos[x(k'_x - k_x)] + i \sin[x(k'_x - k_x)]}{\exp\left[a\left(x-\frac{R}{\sqrt{3}}\right)\right]^2} dx \int_{-\infty}^{\infty} \frac{\cos[y(k'_y - k_y)] + i \sin[y(k'_y - k_y)]}{\exp[ay]^2} dy \\
&+ \frac{V_o}{4\pi^2} \int_{-\infty}^{\infty} \frac{\cos[x(k'_x - k_x)] + i \sin[x(k'_x - k_x)]}{\exp\left[a\left(x+\frac{R}{2\sqrt{3}}\right)\right]^2} dx \int_{-\infty}^{\infty} \frac{\cos[y(k'_y - k_y)] + i \sin[y(k'_y - k_y)]}{\exp\left[a\left(y-\frac{R}{2}\right)\right]^2} dy \\
&+ \frac{V_o}{4\pi^2} \int_{-\infty}^{\infty} \frac{\cos[x(k'_x - k_x)] + i \sin[x(k'_x - k_x)]}{\exp\left[a\left(x+\frac{R}{2\sqrt{3}}\right)\right]^2} dx \int_{-\infty}^{\infty} \frac{\cos[y(k'_y - k_y)] + i \sin[y(k'_y - k_y)]}{\left[a\left(y+\frac{R}{2}\right)\right]^2} dy \tag{E.6}
\end{aligned}$$

where the exponentials in the numerators have been represented as trigonometric functions. Equation (E.6) may be expanded as ten integral pairs, four of which cancel and four of which combine. The remaining four integral pairs,

$$\begin{aligned}
V(\mathbf{r}) &= \frac{V_o}{4\pi^2} \int_{-\infty}^{\infty} \frac{\cos\left[\left(x+\frac{R}{\sqrt{3}}\right)(k'_x - k_x)\right]}{e^{(ax)^2}} dx \int_{-\infty}^{\infty} \frac{\cos[y(k'_y - k_y)]}{e^{(ay)^2}} dy \\
&+ \frac{V_o}{2\pi^2} \int_{-\infty}^{\infty} \frac{\cos\left[\left(x+\frac{R}{2\sqrt{3}}\right)(k'_x - k_x)\right]}{e^{(ax)^2}} dx \int_{-\infty}^{\infty} \frac{\cos[y(k'_y - k_y)] \cos\left[\frac{R}{2}(k'_y - k_y)\right]}{e^{(ay)^2}} dy \\
&+ i \frac{V_o}{4\pi^2} \int_{-\infty}^{\infty} \frac{\sin\left[\left(x+\frac{R}{\sqrt{3}}\right)(k'_x - k_x)\right]}{e^{(ax)^2}} dx \int_{-\infty}^{\infty} \frac{\cos[y(k'_y - k_y)]}{e^{(ay)^2}} dy \\
&+ i \frac{V_o}{2\pi^2} \int_{-\infty}^{\infty} \frac{\sin\left[\left(x+\frac{R}{2\sqrt{3}}\right)(k'_x - k_x)\right]}{e^{(ax)^2}} dx \int_{-\infty}^{\infty} \frac{\cos[y(k'_y - k_y)] \cos\left[\frac{R}{2}(k'_y - k_y)\right]}{e^{(ay)^2}} dy, \tag{E.7}
\end{aligned}$$

may be readily evaluated [51] to produce the momentum space representation of the potential,

$$\begin{aligned}
 V(\mathbf{k}, \mathbf{k}_o) = & \frac{V_o}{4\pi a^2 \exp\left[\frac{(k'_x - k_x)^2 + (k'_y - k_y)^2}{4a^2}\right]} \\
 & \times \left[ \left( \cos\left[\frac{R(k'_x - k_x)}{\sqrt{3}}\right] + 2 \cos\left[\frac{R(k'_x - k_x)}{2\sqrt{3}}\right] \cos\left[\frac{R(k'_y - k_y)}{2}\right] \right) \right. \\
 & \left. + i \left( \sin\left[\frac{R(k'_x - k_x)}{\sqrt{3}}\right] - 2 \sin\left[\frac{R(k'_x - k_x)}{2\sqrt{3}}\right] \cos\left[\frac{R(k'_y - k_y)}{2}\right] \right) \right], \quad (\text{E.8})
 \end{aligned}$$

given by (5.3).

# Bibliography

- [1] J. C. Elenbogen, *A Brief Overview of Nanoelectronic Devices*, 1998 Government Microelectronics Applications Conference (GOMAC98), ©1998 by the Mitre Corporation.
- [2] P. Russell, *Photonic Crystal Fibers*, *Science* 299, 358-362 (2003).
- [3] L. C. Botten, R. C. McPhedran, N. A. Nicorovici, A. A. Asatryan, C. M. de Sterke, P. A. Robinson, K. Bush, G. H. Smith and T. N. Langtry, *Rayleigh Multipole Methods for Photonic Crystal Calculations*, *Progress in Electromagnetics Research* 41, 21-60 (2003).
- [4] J. Arriaga, J. C. Knight and P. St. J. Russell, *Modeling the Propagation of Light in Photonic Crystal Fibers*, *Physica D* 189, 100-106 (2003).
- [5] Blaze Photonics, [www.blazephotonics.com](http://www.blazephotonics.com).
- [6] E. I. Fredholm, *Sur une nouvelle méthode pour la resolution du problème de Dirichlet*, *Översigt af Kongliga Svenska Vetenskaps-Akademiens Förhandlingar* 57, 39-46 (1900).
- [7] E. I. Fredholm, *Sur une classe d'equations fonctionelle*, *Acta Mathematica* 27, 365-390 (1903).
- [8] E. Rutherford, *The Scattering of  $\alpha$  and  $\beta$  Particles by Matter and the Structure of the Atom*, *Philosophical Magazine* 21, 669 (1911).
- [9] N. Bohr, *On the Constitution of Atoms and Molecules*, *Philosophical Magazine* 26, (1913).
- [10] N. F. Mott and H. S. W. Massey, *The Theory of Atomic Collisions*, Oxford University Press, Oxford, (first edition 1933, third edition 1965).
- [11] J. A. Wheeler, *On the Mathematical Description of Light Nuclei by the Method of Resonanting Group Structure*, *Physical Review* 52, 1107-1122 (1937).
- [12] W. Heisenberg, *Z. Phys.* 120, 513 (1943).

- [13] B. A. Lippmann and J. Schwinger, *Variational principles for scattering processes. I*, Physical Review 79, 469-480 (1950).
- [14] M. Gell-Mann and M. L. Goldberger, *The Formal Theory of Scattering*, Physical Review 91, 398-408 (1953).
- [15] C. Møller, *Det. Kgl. Danske Vidensk. Selskab, Math-Fys. Medd.* 23, no. 1 (1945).
- [16] B. A. Lippmann, *Rearrangement collisions*, Physical Review 102, 264-268 (1956).
- [17] H. Ekstein, *Theory of Time-Dependent Scattering for Multichannel Processes*, Physical Review 101, 880-890 (1956).
- [18] E. Gerjuoy, *Time-Independent Nonrelativistic Collision Theory*, Annals of Physics 5, 58-93 (1958).
- [19] L. D. Faddeev, *Scattering Theory for a Three-Particle System*, Zh. Eksp. Teor. Fiz. 39, 1459-1467 (1960). [Soviet Physics JETP 12, 1014-1019 (1961).]
- [20] A. N. Mitra, *Three-Body Problem with Separable Potentials. (I) Bound States*, Nucl. Phys. 32, 529-542 (1962).
- [21] R. Jost and A. Pais, *On the Scattering of a Particle by a Static Potential*, Physical Review 82, 840-851 (1951).
- [22] J. Schwinger, *The Theory of Quantized Fields. V*, Physical Review 93, 615-628 (1954).
- [23] M. Baker, *Determinantal Approach to Meson-Nucleon Scattering*, Annals of Physics 4, 271-305 (1958).
- [24] W. P. Reinhardt and A. Szabo, *Fredholm Method. I. A Numerical Procedure for Elastic Scattering*, Physical Review A 1, 1162-1169 (1970).
- [25] H. R. J. Walters, *Integral Equation Method for the Determination of the Scattering Amplitude*, Journal of Physics B 4, 437-449 (1971).
- [26] P. Gaspard and S. A. Rice, *Exact Quantization of the Scattering from a Classically Chaotic Repellor*, Journal of Chemical Physics 90, 2255-2262 (1989).
- [27] P. Gaspard, D. Alonso, T. Okuda and K. Nakamura, *Chaotic Scattering on  $C_{4v}$  Four-Disc Billiards: Semiclassical and Exact Quantum Theories*, Physical Review E 50, 2591-2596 (1994).

- [28] M. V. Berry, *Quantizing a Classically Ergodic System: Sinai's Billiard and the KKR Method*, *Annals of Physics* 131, 163-216 (1981).
- [29] A. Edlund, I. Bar-On and U. Peskin, *Parallel Computation of Multidimensional Scattering Wave functions for Helmholtz/Schrödinger Equations*, *Applied Parallel Computing. Large Scale Scientific and Industrial Problems. 4th International Workshop, PARA'98. Proceedings: Berlin, Germany, Springer-Verlag*, p. 112-19 (1998).
- [30] I. Bar-on, A. Edlund and U. Peskin, *Parallel Solution of the Multidimensional Helmholtz/Schrödinger Equation Using High Order Methods*, *Applied Numerical Mathematics* 33, 95-104 (2000).
- [31] U. Peskin, A. Edlund and I. Bar-On, *Parallel Wave-Packet Simulations of Electron Transmission Through Water*, *Journal of Chemical Physics* 112, 3220-3226 (2000).
- [32] U. Peskin, A. Edlund, I. Bar-On, Misha Galperin and Abraham Nitzan, *Transient Resonance Structure in Electron Tunneling Through Water*, *Journal of Chemical Physics* 111, 7558-7566 (1999).
- [33] M. Polášek, M. Juřek, M. Ingr, P. Čársky, and J. Horáček, *Discrete Momentum Representation of the Lippmann-Schwinger Equation and its Application to Electron-Molecule Scattering*, *Physical Review A* 61, 032701;1-7 (2000).
- [34] R. H. Landau, *Quantum Mechanics II*, John Wiley & Sons, New York, (1996).
- [35] M. Ingr, M. Polášek, P. Čársky, and J. Horáček, *Discrete Momentum Representation Method for Polar Molecules: Calculation of the Elastic Electron Scattering on the H<sub>2</sub>O Molecule*, *Physical Review A* 62, 032703;1-7 (2000).
- [36] P. Čársky, R. Čurik, F. A. Gianturco, R. R. Lucchese, M. Polášek, *Computing the Exchange Interaction in Electron Scattering from Polyatomic Molecules*, *Physical Review A* 65, 052713;1-8 (2002).
- [37] M. Polášek, P. Čársky, *Efficient Evaluation of the Matrix Elements of the Coulomb Potential Between Plane Waves and Gaussians*, *Journal of Computational Physics* 181, 1-8 (2002).
- [38] R. Čurik, P. Čársky, *Vibrationally Inelastic Electron Scattering on Polyatomic Molecules by the Discrete Momentum Representation (DMR) method*, *Journal of Physics B* 36, 2165-2177 (2003).

- [39] I. H. Sloan, *The numerical Evaluation of Principal-Value Integrals*, Journal of Computational Physics 3, 332-333 (1968).
- [40] M. L. Goldberger and Kenneth M. Watson, *Collision Theory*, John Wiley & Sons, New York, (1964).
- [41] R. G. Newton *Scattering Theory of Waves and Particles*, Springer-Verlag, New York, (1982).
- [42] G. Arfken, *Mathematical Methods for Physicists*, Academic Press, San Diego, (1985).
- [43] P. M. Morse and Herman Feshbach, *Methods of Theoretical Physics*, McGraw-Hill, New York, (1953).
- [44] P. J. Davis and P. Rabinowitz, *Methods of Numerical Integration*, Academic Press, Orlando, (1984).
- [45] H. Engels, *Numerical Quadrature and Cubature*, Academic Press, New York, (1980).
- [46] V. Heine, *Group Theory in Quantum Mechanics*, Pergamon, Oxford, (1960).
- [47] T. Ericson, *Fluctuations of Nuclear Cross Sections in the "Continuum" Region*, Physical Review Letters 5, 430-431 (1960).
- [48] T. Ericson, *A Theory of Fluctuations in Nuclear Cross Sections*, Annals of Physics 23, 390-414 (1963).
- [49] D. M. Brink and R. O. Stephen, *Widths of Fluctuations in Nuclear Cross Sections*, Physics Letters 5, 77-79 (1963).
- [50] W. Żakowicz, *Classical Properties of Quantum Scattering*, Journal of Physics A: Mathematical and General 36, 4445-4464 (2003).
- [51] I. S. Gradshteyn and I. M. Ryzhik, *Table of Integrals, Series, and Products Fifth Edition*, Academic Press, Boston, (1994).